

Stable a-Si:H Based Multijunction Solar Cells with Guidance from Real Time Optics

**Annual Report, Phase I
17 July 1998–16 October 1999**

C.R. Wronski, R.W. Collins, L. Jiao, A. Ferlauto,
P.I. Rovira, R.J. Koval, Z. Lu, and X. Niu
*Center for Thin Film Devices
University Park, Pennsylvania*



NREL

National Renewable Energy Laboratory

1617 Cole Boulevard
Golden, Colorado 80401-3393

NREL is a U.S. Department of Energy Laboratory
Operated by Midwest Research Institute • Battelle • Bechtel

Contract No. DE-AC36-99-GO10337

Stable a-Si:H Based Multijunction Solar Cells with Guidance from Real Time Optics

**Annual Report, Phase I
17 July 1998–16 October 1999**

C.R. Wronski, R.W. Collins, L. Jiao, A. Ferlauto,
P.I. Rovira, R.J. Koval, Z. Lu, and X. Niu
*Center for Thin Film Devices
University Park, Pennsylvania*

NREL Technical Monitor: B. von Roedern

Prepared under Subcontract No. XAF-8-17619-22



NREL

National Renewable Energy Laboratory

1617 Cole Boulevard
Golden, Colorado 80401-3393

NREL is a U.S. Department of Energy Laboratory
Operated by Midwest Research Institute • Battelle • Bechtel

Contract No. DE-AC36-99-GO10337

NOTICE

This report was prepared as an account of work sponsored by an agency of the United States government. Neither the United States government nor any agency thereof, nor any of their employees, makes any warranty, express or implied, or assumes any legal liability or responsibility for the accuracy, completeness, or usefulness of any information, apparatus, product, or process disclosed, or represents that its use would not infringe privately owned rights. Reference herein to any specific commercial product, process, or service by trade name, trademark, manufacturer, or otherwise does not necessarily constitute or imply its endorsement, recommendation, or favoring by the United States government or any agency thereof. The views and opinions of authors expressed herein do not necessarily state or reflect those of the United States government or any agency thereof.

Available electronically at <http://www.doe.gov/bridge>

Available for a processing fee to U.S. Department of Energy
and its contractors, in paper, from:

U.S. Department of Energy
Office of Scientific and Technical Information
P.O. Box 62
Oak Ridge, TN 37831-0062
phone: 865.576.8401
fax: 865.576.5728
email: reports@adonis.osti.gov

Available for sale to the public, in paper, from:

U.S. Department of Commerce
National Technical Information Service
5285 Port Royal Road
Springfield, VA 22161
phone: 800.553.6847
fax: 703.605.6900
email: orders@ntis.fedworld.gov
online ordering: <http://www.ntis.gov/ordering.htm>



EXECUTIVE SUMMARY

TASK I: Novel Improved Intrinsic Materials for Multijunction Solar Cells

I.1. Novel i-Layers for Solar Cells

Phase diagrams that characterize plasma-enhanced chemical vapor deposition of Si thin films at low substrate temperature (200°C) have been established using real time spectroscopic ellipsometry as a probe of thin film microstructural evolution and optical properties. These deposition phase diagrams describe the regimes over which predominantly amorphous and microcrystalline Si phases are obtained as a function of the accumulated film thickness and the hydrogen-to-silane gas flow ratio $R=[H_2]/[SiH_4]$. The diagrams for different substrate materials demonstrate how general principles can be formulated and verified for the design of optimized multistep i-layer components of amorphous silicon p-i-n and n-i-p solar cells.

I.2. Evaluation of Optoelectronic Properties

Research has continued on improving a-Si:H materials for solar cells, particularly with respect to their stability against light-induced degradation. The diluted and undiluted a-Si:H materials that have been studied and characterized were deposited under a wide range of deposition conditions. They have included a-Si:H films from Penn State and Super Laboratory at ETL, as well as our team partners BP Solarex and Uni-Solar. The similarities and differences in their properties have been evaluated and detailed analysis, required for obtaining reliable gap state parameters for all gap states, has been carried out on several of these materials.

Our characterization and analysis results show that in the annealed state, charged defects can dominate the properties of truly “device quality” a-Si:H materials, materials that have actually proven their quality in high performance solar cells. We found that because of the low densities of neutral dangling bond, D^0 , states in such materials even small changes in charged defects can result in significant difference in the electron mobility-lifetime ($\mu\tau$) products and

subgap absorption $\alpha(h\nu)$. If they are interpreted in the simple manner based on D^0 state dominance, then there are clear inconsistencies between results on subgap absorption and those on $\mu\tau$ products. However the results can be understood when account is taken of the charged defect states. On the other hand, analysis of these charged defects presents a big challenge because their densities cannot be independently measured as in the case of neutral dangling bond defect states, as well as they introduce a large number of new parameters for characterization. The methodology for the characterization of all the gap states, developed at Penn State has been applied to the analysis of results on a-Si:H in materials in both annealed and 1 sun degraded states.

It should also be pointed out that “operational parameters” are not unique because of the flexibility offered in fitting as a result of having as many as 20 different parameters. Nevertheless the ability to obtain good fits to so many results using such “operational parameters” is in direct contrast to the inability to do so when charged defects are not included. It offers some new insights about the nature of gap states and their contribution to solar cell performance and stability.

TASK II: Insights into Improved Stability in Materials and Solar Cells

II.1. Degradation Studies

The type, nature and densities of different light induced defects in optimized a-Si:H materials have been investigated and characterized. These studies have been carried out on films and corresponding Schottky barrier cell structures with different thicknesses of the intrinsic bulk layers. Taking into account the inadequacy of the approach based on solely “neutral dangling bonds”, the characterization was expanded in the attempt to include all of the gap states. We find that light-induced charged defects are as important as the neutral dangling bond defects in determining the properties and stability of a-Si:H materials and solar cells. We also find that

unlike previous claims in truly “device quality” materials the degraded steady states do depend on both intensity and temperature (even less than 70°C). This makes the commonly used arbitrary, accelerated degradation results meaningless unless they are related to 1 sun degraded states. Extensive studies of light induced defects were carried out on diluted ($R=10$) Schottky barrier solar cell structures and the corresponding films. The measurements on Schottky barrier cell structures, which include forward I-V, light I-V and QE with different i layer thicknesses, are analyzed with results of $\mu\tau$ products and subgap absorption spectra obtained on the corresponding films. The focus of the work here is mainly on the degraded steady state (DSS) obtained with 1 sun illumination at 25°C in films and Schottky barrier cells. All these results were analyzed using a distribution of gap states shown in Fig.1, where in addition to the neutral dangling bond D^0 states two Gaussian distributions of defect states are introduced above and below midgap. This and the procedure for obtaining “operational” parameters for these states are discussed.

TASK III: Optimization of Solar Cell Performance with Improved Intrinsic Layers

III.1. Optimization of p/i Interfaces

The formation of p/i interfaces in hydrogenated amorphous silicon p-i-n solar cells prepared by plasma-enhanced chemical vapor deposition has been analyzed in detail using real time optics. With this capability, three effects have been successfully separated and quantified: (i) contaminant layer deposition at the p-layer surface with a sensitivity of $\pm 0.1 \text{ \AA}$, (ii) thermal emission of bonded hydrogen from the p-layer with a sensitivity of $\pm 0.1 \text{ at.}\%$ ($\pm 2 \text{ meV}$ in optical gap), and (iii) surface temperature variations with a sensitivity of $\pm 1^\circ\text{C}$. The separation of these

competing effects has yielded a better understanding of p/i interface formation and has led to an optimum process for device fabrication.

III.2. p-Layers for n-i-p Solar Cells

Real time optical analysis (RTSE) has been applied to study the nucleation, coalescence, and growth processes for $\sim 100\text{-}200$ Å thick microcrystalline silicon ($\mu\text{c-Si:H}$) p-layers on H_2 plasma-treated amorphous silicon (a-Si:H) i-layers in the substrate/(n-i-p) device configuration. For such i-layers, p-layer microcrystal nucleation at low plasma power is controlled by the catalytic effects of B-containing radicals at the i-layer surface, irrespective of the dopant source, whereas nucleation at higher plasma power is controlled by the bombardment of the i-layer by Si-containing ions. Under high power plasma conditions using BF_3 , dense single-phase $\mu\text{c-Si:H}$ p-layers can be obtained over a wide range of the dopant gas flow ratio. In contrast, for B_2H_6 and $\text{B}(\text{CH}_3)_3$, such properties are obtained only over narrow flow ratio ranges owing to the relative ease of dissociation of these gases in the plasma. Based on these results, an optimized $\mu\text{c-Si:H}$ p-layer has been developed for application in n-i-p solar cells.

III.3. Protocrystalline Intrinsic Layers

Studies have been carried out on the thickness dependent transition between the amorphous and microcrystalline phases in intrinsic Si:H materials (i-layers) and its effect on p-i-n solar cell performance. P(a-SiC:H)-i(a-Si:H)-n($\mu\text{cSi:H}$) cell structures were deposited with the intrinsic Si:H layer thickness and the flow ratio of hydrogen to silane, $R=[\text{H}_2]/[\text{SiH}_4]$, guided by an evolutionary phase diagram obtained from real-time spectroscopic ellipsometry. The thickness range over which the fill factors are controlled by the bulk was established and their characteristics investigated with different protocrystalline i-layer materials (i.e., materials prepared near the amorphous to microcrystalline boundary but on the amorphous side). Insights into the properties of these materials and the effects of the transition to the microcrystalline phase were obtained from the systematic changes in the initial fill factors, their light-induced

changes, and their degraded steady states for cells with i-layers of different thickness and H_2 dilution.

TASK IV: Optimization of Multijunction Solar Cells

IV.1. Textured TCO Studies

We have applied a rotating-compensator multichannel ellipsometer to perform real time Stokes vector spectroscopy (also called polarimetry) during the preparation of hydrogenated amorphous silicon (a-Si:H) p-i-n solar cells on Asahi U-type textured tin-oxide (SnO_2) surfaces. With this spectroscopy (1.5 to 4.0 eV), the irradiance I_r and polarization parameters $\{(Q, \chi), p\}$ of the specularly reflected beam are obtained with 0.8 s resolution versus time during solar cell preparation. Here Q and χ are the tilt and ellipticity angles of the polarization state and p is the degree of polarization. An analysis of Q and χ that neglects the effects of the texture can provide the time evolution of the thicknesses, microscopic structure, and the optical properties of the component layers of the a-Si:H solar cell. Deviations of the measured reflectance spectra from those predicted on the basis of the (Q, χ) analysis provide the thickness dependence of the scattering and the evolution of the macroscopic structure of the solar cell. The measurement and analysis approach is important because of its potential application for real time monitoring of solar cell production. The analysis results also provide realistic inputs for optical modeling of the effects of texture in light trapping.

IV.2. Optical Modeling

Analytical expressions have been developed that provide close fits to the dielectric functions ϵ of amorphous (a), nanocrystalline (nc), and microcrystalline (μc) silicon-based films. These expressions provide the capability of accurate optical modeling of the intrinsic (i) layers used in a-Si:H-based multijunction solar cells. As a result, a set of optical functions

representative of high-density a-Si:H and its alloys spanning the full solar spectrum can be generated from the optical gap alone.

IV.3. Tunnel Junction Formation

Tunnel junction formation for applications in amorphous silicon (a-Si:H) based multijunction n-i-p solar cells has been studied using real time optics. The junction structure investigated in detail here consists of a thin (~ 100 Å) layer of n-type microcrystalline silicon ($\mu\text{c-Si:H}$) on top of an equally thin p-type $\mu\text{c-Si:H}$ layer, the latter deposited on thick (~ 2000 Å) intrinsic a-Si:H. Such structures have been optimized to obtain single-phase $\mu\text{c-Si:H}$ with a high crystallite packing density and large grain size for both layers of the tunnel junction. We have determined the conditions under which grain growth is continuous across the p/n junction and the conditions under which renucleation of n-layer grains can be ensured at the junction. One important finding of this study is that the optimum conditions for single-phase, high-density $\mu\text{c-Si:H}$ n-layers are different depending on whether the substrate is a $\mu\text{c-Si:H}$ p-layer or is a H_2 -plasma treated or untreated a-Si:H i-layer. Thus, the top-most $\mu\text{c-Si:H}$ layer of the tunnel junction must be optimized in the multi-junction device configuration, rather than in single cell configurations on i-layers. These observations are explained using evolutionary phase diagrams for Si film growth.

TABLE OF CONTENTS

TASK I:	<u>Novel Improved Intrinsic Materials for Multijunction Solar Cells</u>	10
I.1.	<u>Novel i-Layer Materials for Solar Cells</u>	10
	<i><u>Motivation and Overview</u></i>	10
	<i><u>Experimental Details</u></i>	11
	<i><u>Results and Discussion</u></i>	12
	<i><u>Concluding Remarks</u></i>	17
	<i><u>References</u></i>	18
I.2.	<u>Evaluation of Optoelectronic Properties</u>	29
	<i><u>Results and Discussion</u></i>	29
	<i><u>References</u></i>	31
TASK II:	<u>Insights into Improved Stability in Materials and Solar Cells</u>	36
II.1.	<u>Degradation Studies</u>	36
	<i><u>Results and Discussion</u></i>	36
	<i><u>References</u></i>	41
TASK III:	<u>Optimization of Solar Cell Performance with Improved Intrinsic Layers</u>	49
III.1.	<u>Optimization of p/i Interfaces</u>	49
	<i><u>Motivation and Overview</u></i>	49
	<i><u>Experimental Details</u></i>	49
	<i><u>Results and Discussion</u></i>	50
	<i><u>Concluding Remarks</u></i>	54
	<i><u>References</u></i>	55
III.2.	<u>p-Layers for n-i-p Solar Cells</u>	61
	<i><u>Motivation and Overview</u></i>	61
	<i><u>Experimental Procedures</u></i>	62
	<i><u>Results and Discussion:</u></i>	
	<i><u>Effect of H₂-Dilution on the Nucleation and Growth of $\mu\text{c-Si:H}$ p-Layers</u></i>	63
	<i><u>Results and Discussion:</u></i>	
	<i><u>Effect of Doping Level on the Nucleation and Growth of $\mu\text{c-Si:H}$ p-Layers</u></i>	64
	<i><u>Results and Discussion:</u></i>	
	<i><u>Effect of Plasma Power on the Nucleation and Growth of $\mu\text{c-Si:H}$ p-Layers</u></i>	68
	<i><u>Concluding Remarks</u></i>	71
	<i><u>References</u></i>	72
III.3.	<u>Protocrystalline Intrinsic Layers</u>	89
	<i><u>Motivation and Overview</u></i>	89
	<i><u>Experimental Procedures</u></i>	90
	<i><u>Results and Discussion</u></i>	91
	<i><u>Concluding Remarks</u></i>	94
	<i><u>References</u></i>	95
TASK IV:	<u>Optimization of Multijunction Solar Cells</u>	103
IV.1	<u>Textured TCO Studies</u>	103
	<i><u>Motivation and Overview</u></i>	103
	<i><u>Experimental Procedures</u></i>	104
	<i><u>Results and Discussion</u></i>	105

<u>Concluding Remarks</u>	109
<u>References</u>	110
<u>IV.2. Optical Modeling</u>	121
<u>Motivation and Overview</u>	121
<u>Experimental Details</u>	121
<u>Results</u>	123
<u>Discussion</u>	124
<u>Concluding Remarks</u>	124
<u>References</u>	125
<u>IV.3. Tunnel Junction Formation</u>	128
<u>Motivation and Overview</u>	128
<u>Experimental Details</u>	128
<u>Results</u>	130
<u>Discussion</u>	132
<u>Summary</u>	133
<u>References</u>	134
<u>APPENDIX I</u>	143
<u>Bibliography (1998-1999)</u>	153

TASK I: Novel Improved Intrinsic Materials for Multijunction Solar Cells

I.1. Novel i-Layer Materials for Solar Cells

Motivation and Overview

The benefits of moderate H_2 -dilution of SiH_4 (gas flow ratio $R=[H_2]/[SiH_4]=5-15$) in plasma-enhanced chemical vapor deposition (PECVD) of amorphous semiconductors have been noted in several studies. [1-6] In amorphous silicon (a-Si:H) deposition, moderate dilution leads to higher stability films having greater resistance to the Staebler-Wronski effect. [7] Recent studies have also explored the benefits of H_2 -dilution in intrinsic (i) layer preparation for higher stability a-Si:H p-i-n and n-i-p solar cells. [4-6,8-10] Such studies have suggested a guiding principle for fabrication of optimum materials and devices, namely, that the i-layer should be amorphous, yet prepared as close as possible to the boundary between amorphous (a) and microcrystalline (μc) film growth versus the H_2 -dilution ratio. [9-11] Operating near the a $\rightarrow\mu c$ boundary, however, has its drawbacks because the boundary locations in deposition parameter space -- and thus the resulting film properties -- are very sensitive to the substrate material and accumulated film thickness, as recognized just recently. [10,12] As a result, optimization of the i-layer process for devices is more complicated than previously recognized.

In this task, we developed deposition phase diagrams for three different substrate materials. These diagrams describe the regimes of bulk layer thickness d_b and dilution ratio R within which dominant a-Si:H and μc -Si:H phases are obtained. There are two important outcomes of our real time optical studies. First, the deduced structural evolution and dielectric functions identify the regimes of d_b and R within which dominant a-Si:H and μc -Si:H phases are obtained. The resulting deposition phase diagrams can be used to direct the preparation of i-layers on different doped layer surfaces for optimized electronic devices. Second, the dielectric functions of the films can be analyzed to assess the degree of ordering and crystallinity in the amorphous and microcrystalline regimes, respectively. The analysis results in the amorphous regime provide insights into the observed improvements in materials and device performance

and stability as R is increased to the a→ μ c boundary. The analysis results in the microcrystalline regime provide insights into the evolution of crystallinity from nucleation, which leads to a mixed amorphous/microcrystalline phase, through growth which leads to a stable, single-phase microcrystalline structure.

Substrates of relevance for solar cells used in these studies include a-Si:H prepared with R=0, simulating the situation in which the underlying doped layer is amorphous, and μ c-Si:H prepared with R=200, simulating the situation in which the underlying doped layer is microcrystalline. Second, the deposition phase diagrams reveal the dangers of correlating materials properties and solar cell performance when different substrates and/or thicknesses are used for the materials and device studies. In this case, an additional substrate of relevance is crystalline silicon (c-Si) with its native oxide intact, which is often used for materials analyses.

Experimental Details

Three substrate materials were used here, including (i) native oxide-covered crystalline Si (c-Si) wafers; (ii) newly-deposited (unoxidized) a-Si:H films prepared to 3000 Å without dilution (R=0); and (iii) newly-deposited p-type μ c-Si:H films prepared to 200 Å using gas flow ratios of [SiH₄]: [H₂]:[BF₃] of 1:200:0.05. For the latter, the PECVD process was optimized for single-phase μ c-Si:H on a-Si:H. [13] The deposition temperature was 200°C for all substrate and overlying films. For the overlying Si, the SiH₄ pressure was set in the absence of H₂ flow at 0.07 Torr for 0≤R≤40 and 0.04 Torr for 50≤R≤80, and H₂ was introduced to establish the selected flow ratio from 0 to 80. As a result, the total pressure increased from 0.07 Torr at R=0 to 0.9 Torr at R=80. This approach was used to avoid possible enhancement in polysilane radical formation in the plasma with decreasing R at a fixed total pressure. Deposition rates ranged from 1.3 Å/s (R=0) to 0.10 Å/s (R=80). Real time spectroscopic ellipsometry (RTSE) measurements applied to establish the deposition phase diagrams were performed using rotating polarizer and compensator multichannel ellipsometers with spectral ranges of 1.3-4.3 eV. [14]

Results and Discussion

As an example of RTSE analysis results, Fig. I.1.1 shows the surface roughness layer thickness (d_s) versus bulk layer thickness (d_b) for three Si films prepared onto R=0 a-Si:H substrate films. The d_s value at the first monolayer of bulk layer growth ($d_b=2.5$ Å, vertical broken line in Fig. I.1.1) is controlled by the roughness on the underlying R=0 substrate film which varies with deposition history, i.e., the PECVD sequence prior to substrate film preparation. Such substrate film roughness has a large in-plane scale (>100 Å) and exerts no measurable effect on the subsequent variations in d_s . In fact, the features of interest in Fig. I.1.1 are the abrupt increases in d_s that signify the a $\rightarrow\mu$ c transition for the three Si depositions. This transition is also identified by a change in the dielectric function of the accumulating material, and occurs near $d_b=3000$, 300, and 30 Å for R=15, 30 and 80, respectively. This change is characterized by a decrease in the magnitude of ϵ_2 in the range from 2.5 to 3 eV as the a $\rightarrow\mu$ c boundary is crossed due to possible electronic confinement effects in the early stages of crystallite formation and due to the appearance of indirect gap electronic structure as the microcrystals increase in size. Similar analyses to those of Fig. I.1.1 have been performed for the other substrate types.

Figure I.1.2 depicts superimposed deposition phase diagrams from the RTSE analyses. The three lines are the phase boundaries for the different substrates. These boundaries separate the growth of a-Si:H (left) and μ c-Si:H (right). For a-Si:H substrates, the a $\rightarrow\mu$ c boundary varies continuously from $d_b\sim 3000$ Å for R=15 to $d_b\sim 30$ Å for R=80. In contrast for c-Si wafer substrates, the a $\rightarrow\mu$ c boundary varies from $d_b\sim 2000$ Å for R=15 to $d_b\sim 75$ Å for R=30; immediate nucleation of μ c-Si:H occurs on oxide-covered c-Si for $R\geq 40$. Finally, for μ c-Si:H p-layer substrates, for $d_b<50$ Å it is more difficult to distinguish the phase owing to the ~ 50 Å thick roughness on p-type μ c-Si:H substrates. However, it is clear that overlying Si films prepared with $R\leq 5$ remain amorphous from the phase-sensitivity lower limit of $d_b\sim 50$ Å throughout deposition to $d_b\sim 3000$ Å, whereas films prepared with $R\geq 10$ are microcrystalline over this range. As a result, the a $\rightarrow\mu$ c boundary for this substrate must lie between R=5 and 10

for $50 < d_b < 3000 \text{ \AA}$. The importance of Fig. I.1.2 rests in its depiction of results for films ranging in thickness from $\sim 3000 \text{ \AA}$ used for bulk i-layers in single-junction solar cells, to $\sim 100 \text{ \AA}$ used for near-interface i-layer components.

The deposition phase diagrams of Fig. I.1.2 show that Si microcrystals do not nucleate immediately from ($R=0$) a-Si:H surfaces even for R values up to 80. This behavior is in contrast to oxide-covered c-Si and p-type $\mu\text{c-Si:H}$ surfaces on which immediate nucleation occurs for $R=40$ and 10, respectively. Thus, the a-Si:H substrate suppresses $\mu\text{c-Si:H}$ formation by imposing its structure on the growing film. It is interesting that such substrate-induced structure can propagate for 3000 \AA or more when $R=15$. Under these conditions, it has been suggested that regions of higher ordering develop gradually as the a-Si:H grows, and these serve as sites for microcrystal formation. [9] Another contributing factor to the $a \rightarrow \mu\text{c}$ transition at $d_b \sim 3000 \text{ \AA}$ may be the buildup of stress in the network. [15] Such stress may be relieved through the development of roughness or void structures that may also induce microcrystal formation. Although it is generally believed that increased H penetration from the plasma causes the Si-Si bonding network to relax, [16] H-induced stress may build up due to trapped H_2 . Analyses of the bulk dielectric functions deduced versus d_b in the amorphous regime ($d_b < 3000 \text{ \AA}$) for $R=15$ depositions on c-Si and $R=0$ a-Si:H reveal no decreases in the broadening Γ and no significant increases ($< 3 \text{ vol.}\%$) in void fraction. Thus, any regions of higher ordering or voids that lead to microcrystal formation are not readily detectable by RTSE. In the following paragraphs, we discuss in detail the information that can be extracted from inspection and analysis of the dielectric functions of the Si films.

First, Figures I.1.3 and 4 contrast the spectra of films prepared under identical conditions to identical thicknesses, but on different substrate surfaces. The spectra in Fig. I.1.3 for 2300 \AA Si films prepared at $R=10$ on oxide-covered c-Si and clean $R=200 \mu\text{c-Si:H}$ substrate surfaces are characteristic of amorphous and fine-grained microcrystalline phases, respectively. This figure highlights the disconcerting fact that the phase of the final film is controlled by the substrate rather than by the deposition conditions even for film thicknesses $> 2000 \text{ \AA}$. The spectra in Fig.

I.1.4 for 200 Å Si films prepared at R=40 on a-Si:H (R=0) and c-Si substrate surfaces are characteristic of amorphous and larger-grained microcrystalline phases, respectively. This figure highlights the fact that $\mu\text{c-Si:H}$ nucleates readily on the native oxide of c-Si but not on clean a-Si:H. By oxidizing the underlying a-Si:H surface, one can obtain comparable $\mu\text{c-Si:H}$ nucleation behavior for the two substrates. [17]

To assess a-Si:H films obtained at different phase diagram points in greater detail, the dielectric functions $\epsilon = \epsilon_1 + i\epsilon_2$ as determined by RTSE have been fit using the Tauc-Lorentz empirical model. [18] Figure I.1.5 depicts the (a) oscillator width Γ and (b) Tauc optical gap E_g at 200°C versus R for films prepared on c-Si and R=0 a-Si:H. With increasing R, films of decreasing thickness are probed in order to remain within the amorphous regime. Analyses of R=0 films of different thicknesses show that the trends in Fig. I.1.5 are meaningful in terms of bulk properties and are attributable to the increase in R. Γ is expected to be inversely proportional to the excited state lifetime for transitions of electrons and holes deep into the bands. In support of this interpretation, the studies of Sec. IV.2. show that Γ is increased by local potential fluctuations and disorder induced by alloying of a-Si:H with Ge or C (see Fig. IV.2.2). Thus, the decrease in Γ in Fig. I.1.5(a) suggests increasing order in the films with increasing R (with high R a-Si:H films being called "protocrystalline"). This trend can account for improved interface characteristics when thin high R layers are incorporated at the p/i interfaces in solar cells. [10] Thus, by utilizing an R=0 a-Si:H substrate film to suppress $\mu\text{c-Si:H}$ formation, one can take advantage of the favorable PECVD conditions at increased R. Favorable conditions may be the result of (i) greater relaxation of the network by diffusing H due to either a reduced deposition rate, [5, 19] or an increased concentration of plasma H, [16] (ii) enhanced coverage of the surface by H which reduces the defect density in the final film bulk, [20] and (iii) a reduced concentration of detrimental short lifetime precursors. [21] Finally, Fig. I.1.6 shows Γ_1 versus the best fit CM optical gap for the a-Si:H films with variable R from Fig. I.1.5, along with results deduced for $\text{a-Si}_{1-x}\text{C}_x\text{:H}$ ($0 \leq x \leq 0.23$) at thicknesses of 200 Å, both at 200°C. These

results reveal that for thin wide-gap amorphous films used as p-layers or undoped p/i interface layers in solar cells, greater ordering can be achieved by H_2 -dilution tailoring of the gap.

Next, the evolution of the Si film optical properties will be assessed as the film crosses the $a \rightarrow \mu c$ boundary. Figure I.1.7 shows the dielectric functions at different thicknesses obtained from real time SE for a graded Si film deposited under fixed conditions with $R=39$ on GaAs at $150^\circ C$. A GaAs substrate is used to achieve greater optical contrast when the Si film is grown on its surface. The Si film crosses the $a \rightarrow \mu c$ boundary versus d at a thickness of $\sim 70 \text{ \AA}$, so that the process evolves from predominantly a-Si:H growth ($d \sim 0-50 \text{ \AA}$), through nanocrystal development within an amorphous matrix ($d \sim 50-200 \text{ \AA}$), to single-phase μc -Si:H growth ($d > 500 \text{ \AA}$). For the latter, the grain size increases only weakly with d . This overall growth behavior is characteristic of films that cross the $a \rightarrow \mu c$ boundary and has been corroborated by cross-sectional transmission electron microscopy. As shown in Fig. I.1.7, ϵ is fit using a single oscillator in the amorphous regime ($d=50 \text{ \AA}$), and two oscillators in the nanocrystalline ($d=165 \text{ \AA}$) and microcrystalline ($d=740 \text{ \AA}$) regimes. Figure I.1.8 shows the best fit optical gap, E_G , and resonance and broadening energies (E_1, Γ_1) versus d . Interestingly the optical gap is in the 1.6 to 1.7 eV range for the a-Si:H and nc-Si:H regimes, but decreases toward the bulk c-Si gap with increasing d in the μc -Si:H regime. The broadening energy, reflecting grain boundary scattering, decreases and then stabilizes with increasing d , an indication of the increase and stabilization in the grain size. To obtain further insights, Fig. I.1.9 shows ϵ at $200^\circ C$ and its best fit for a nc-Si:H film that nucleates immediately at $R=200$ from a H_2 -plasma treated a-Si:H surface as discussed in Sec. III.2. The much wider gap of 2.2 eV in this case is attributed to stronger confinement effects in the nanocrystals that are evident only when the nc-Si:H film is single-phase and any intergranular a-Si:H is fully etched away under the higher R conditions. As described in Sec. III.2, this etching leaves voids at the boundaries that serve as barriers that increase confinement of electrons within the crystallites.

Next we discuss the implications of the phase diagrams for the optimization of a-Si:H solar cells in the p-i-n and n-i-p configurations. For cells in the glass/(conducting oxide)/p-i-n

configuration having amorphous p-layers, the phase boundary for the $R=0$ a-Si:H substrate in Fig. I.1.2 is relevant for guiding i-layer deposition. In this case, higher cell performance can be obtained by initiating i-layer deposition at the p/i interface with a high R value, and then reducing R for the bulk i-layer to avoid microcrystal development. [10] This places material with the highest overall quality and widest optical gap adjacent to the p/i interface, where it is most effective at enhancing cell performance. For a 4000 Å thick i-layer prepared in two steps of 200 Å and 3800 Å, optimum cell performance in both annealed and fully light-soaked states has been obtained using two-step R values of 40 and 10, respectively. [10] This result is consistent with the concept of maintaining deposition as close as possible to the $a \rightarrow \mu c$ boundary, but on the amorphous side versus thickness. For cells in the p-i-n configuration having microcrystalline p-layers, the phase boundary for the $R=200$ p-type μc -Si:H substrate in Fig. I.1.2 is relevant in guiding i-layer fabrication. In this case, a reverse optimization strategy appears necessary, namely, initiating i-layer deposition with a low R value to prevent propagation of microcrystallinity and then increasing R to ensure the highest quality material in the bulk i-layer. Similar considerations apply for solar cell fabrication in the metal/(back reflector)/n-i-p configuration. This configuration has the disadvantage that R must be increased in the second step in order to utilize beneficial i-layer properties near the i/p interface. As a result, any inadvertent microcrystal formation prior to the second step is expected to be highly detrimental. In contrast, the advantage of the n-i-p configuration is that a μc -Si:H p-layer can be incorporated without concern for its effect on the i-layer structure. For either configuration, once microcrystallinity develops in an underlying layer of the device, R must be decreased below the optimum bulk value ($R \sim 10$) in the overlying layer to arrest its continued development.

Finally, it is important to discuss the implications of the deposition phase diagrams for the correlation of materials properties with solar cell performance. First, the thickness dependence the phase boundary can lead to inconsistencies when correlating materials and device properties. For a 2000 Å thick i-layer of a solar cell, for example, $R \sim 15$ is expected to yield high performance as this is the maximum value sustainable while remaining below the

a \rightarrow μ c transition. If 5000 Å thick R=15 films are prepared on either amorphous layers or c-Si substrates for materials analysis, however, such layers will exhibit a structure varying from a-Si:H in the first \sim 2500 Å to μ c-Si:H in the next \sim 2500 Å. Second, the substrate dependence of the phase boundary can lead to similar inconsistencies. For a 1000 Å thick i-layer used in a multijunction solar cell, for example, R \sim 18 is expected to yield high performance. If 1000 Å thick R=18 films are prepared on c-Si substrates, however, only the first \sim 500 Å of the film will be amorphous whereas the remaining 500 Å will be microcrystalline. Thus, the phase diagrams demonstrate that to obtain valid (materials properties)-(device performance) correlations, the material properties must be obtained from depositions on similar substrates with similar thicknesses as those for devices. This fact also demonstrates the need to consider the effects of texturing of the conducting oxide and back reflector used in p-i-n and n-i-p solar cell production. Because the texture exhibits a large in-plane scale (>1000 Å) and the a-Si:H i-layers appear to conformally cover such surfaces, we expect that the texture has little effect on the deposition phase diagram; however future studies are needed to verify this expectation.

Concluding Remarks

Real time optical studies of Si film growth by PECVD have elucidated deposition phase diagrams that describe regimes of film thickness and H₂-dilution ratio $R=[H_2]/[SiH_4]$ over which amorphous and microcrystalline films are obtained. When Si films are deposited at high R ($R>15$) on a-Si:H ($R=0$) substrate films, the substrate suppresses microcrystal formation. In this regime, favorable plasma conditions lead to films with a higher degree of order and higher stability. In contrast, when Si films are deposited at intermediate and high R ($R>5$) on μ c-Si:H substrate films, the substrate enhances microcrystal formation. Because of the strong effect of the substrate on the overdeposited material, solar cell optimization is more complicated than previously recognized. In addition, incorrect conclusions can be drawn in materials-device correlations if the materials are not prepared on similar substrates to similar thicknesses as the i-layer in the solar cell.

References

1. K. Tanaka (Ed.), *Glow Discharge Hydrogenated Amorphous Silicon*, (Kluwer, Boston, 1988).
2. S. Guha, K.L. Narasimhan, and S.M. Pietruszko, *J. Appl. Phys.* **52**, 859 (1981).
3. A. Matsuda and K. Tanaka, *J. Non-Cryst. Solids* **97-98**, 1367 (1987).
4. Y. Lee, L. Jiao, H. Liu, Z. Lu, R.W. Collins, and C.R. Wronski, *Conf. Record 25th IEEE Photovoltaics Specialists Conference*, (IEEE, NY, 1996), p. 1165.
5. S. Okamoto, Y. Hishikawa, and S. Tsuda, *Jpn. J. Appl. Phys.* **35**, 26 (1996).
6. B. Rech, S. Wieder, F. Siebke, C. Beneking, and H. Wagner, *Mater. Res. Soc. Symp. Proc.* **420**, 33 (1996).
7. D.L. Staebler and C.R. Wronski, *Appl. Phys. Lett.* **28**, 1198 (1976).
8. M. Bennett, K. Rajan, and K. Kritikson, *Conf. Record 23rd IEEE Photovoltaics Specialists Conference*, (IEEE, NY, 1993), p. 845.
9. D.V. Tsu, B.S. Chao, S.R. Ovshinsky, S. Guha, and J. Yang, *Appl. Phys. Lett.* **71**, 1317 (1997).
10. J. Koh, Y. Lee, H. Fujiwara, C.R. Wronski, and R.W. Collins, *Appl. Phys. Lett.* **73**, 1526 (1998).
11. Y. Lu, S. Kim, M. Gunes, Y. Lee, C.R. Wronski, and R.W. Collins, *Mater. Res. Soc. Symp. Proc.* **336**, 595 (1994).
12. S. Guha, J. Yang, D.L. Williamson, Y. Lubianiker, J.D. Cohen, and A.H. Mahan, *Appl. Phys. Lett.* **74**, 1860 (1999).
13. J. Koh, H. Fujiwara, R.J. Koval, C.R. Wronski, and R.W. Collins, *J. Appl. Phys.* **85**, 4141 (1999).
14. R.W. Collins, I. An, H. Fujiwara, J. Lee, Y. Lu, J. Koh, and P.I. Rovira, *Thin Solid Films* **313-314**, 18 (1998).
15. U. Kroll, J. Meier, A. Shah, S. Mikhailov, and J. Weber, *J. Appl. Phys.* **80**, 4971 (1996).

16. H. Shirai, D. Das, J. Hanna, and I. Shimizu, Appl. Phys. Lett. **59**, 1096 (1991).
17. A.S. Ferlauto, J. Koh, P.I. Rovira, C.R. Wronski, and R.W. Collins, Mater. Res. Soc. Symp. Proc. (1999, in press).
18. G.E. Jellison, Jr., and F.A. Modine, Appl. Phys. Lett. **69**, 371 (1996); **69**, 2137 (1996).
19. R.A. Street, Phys. Rev. B **43** (1991) 2454.
20. G. Ganguly and A. Matsuda, Phys. Rev B **47**, 3661 (1993).
21. I.S. Osborne, N. Hata, and A. Matsuda, J. Non-Cryst. Solids **198-200** (1996) 991.

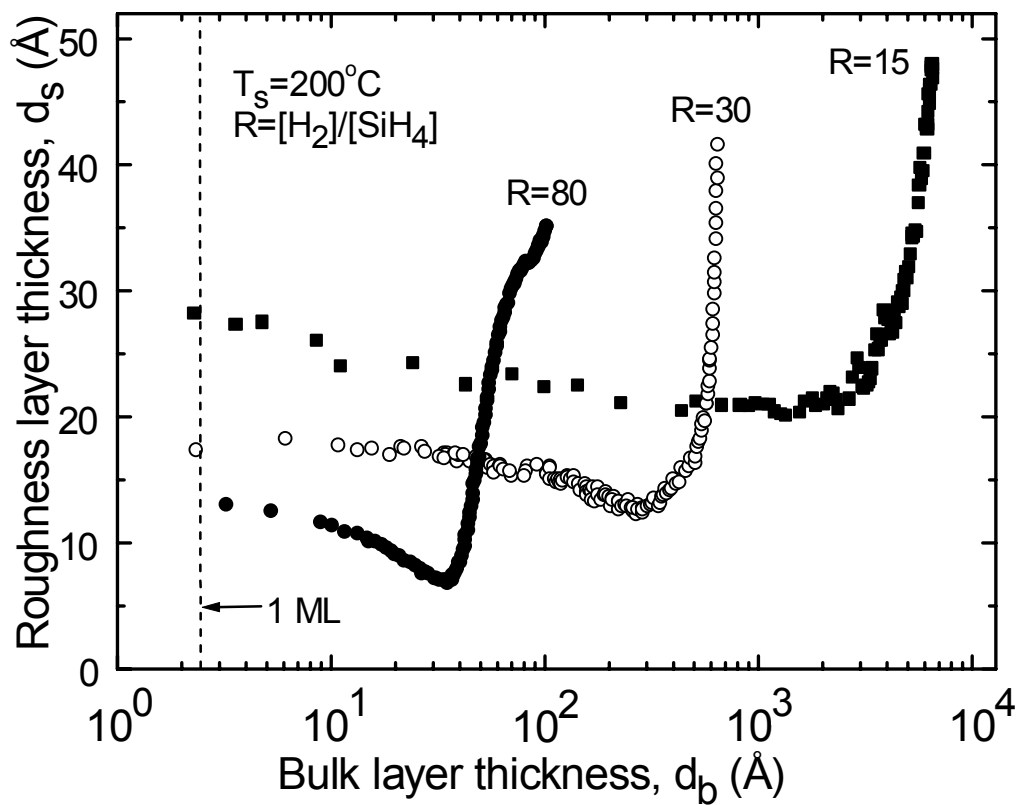


Figure I.1.1 Surface roughness layer thickness (d_s) versus bulk layer thickness (d_b) from RTSE data collected during the preparation of Si films with $R=[\text{H}_2]/[\text{SiH}_4]=15, 30$, and 80 . The underlying substrate is a-Si:H prepared with $R=0$.

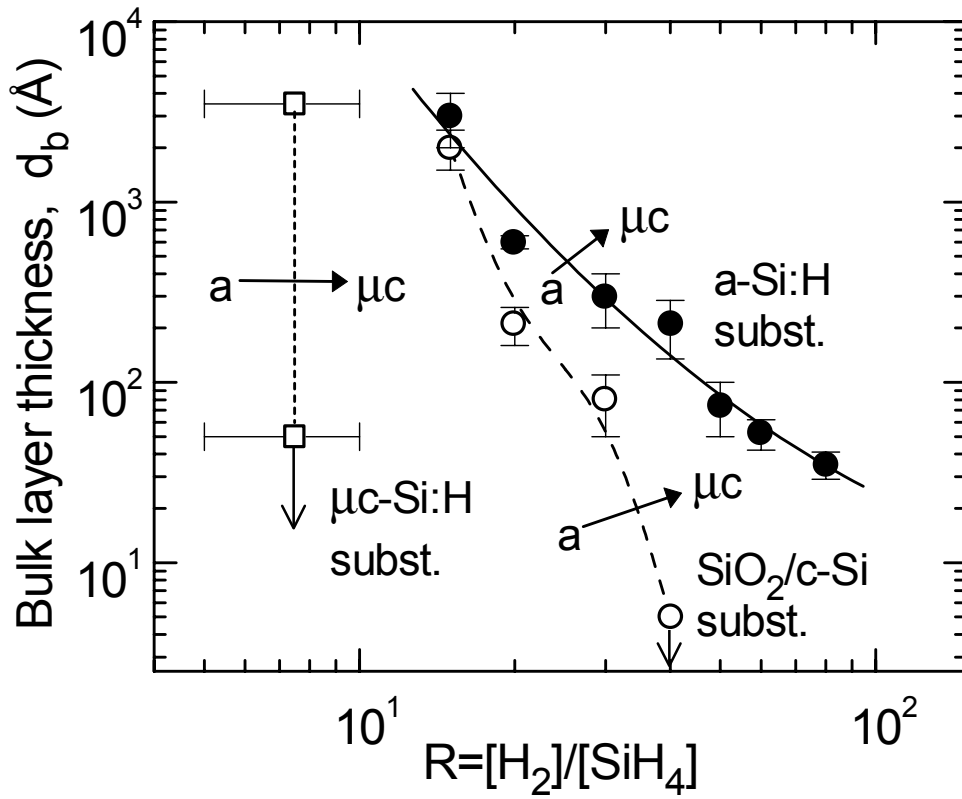


Figure I.1.2 Phase boundaries vs. R and d_b for the deposition of Si films at 200°C on different substrate materials: 3000 Å thick $R=0$ a -Si:H (solid line and filled circles); native-oxide-covered c -Si wafers (dashed line and open circles); and 200 Å $R=200$ p -type μc -Si:H (dotted line and open squares). The phase boundaries (lines) separate a -Si:H (left) and μc -Si:H (right) growth regimes.

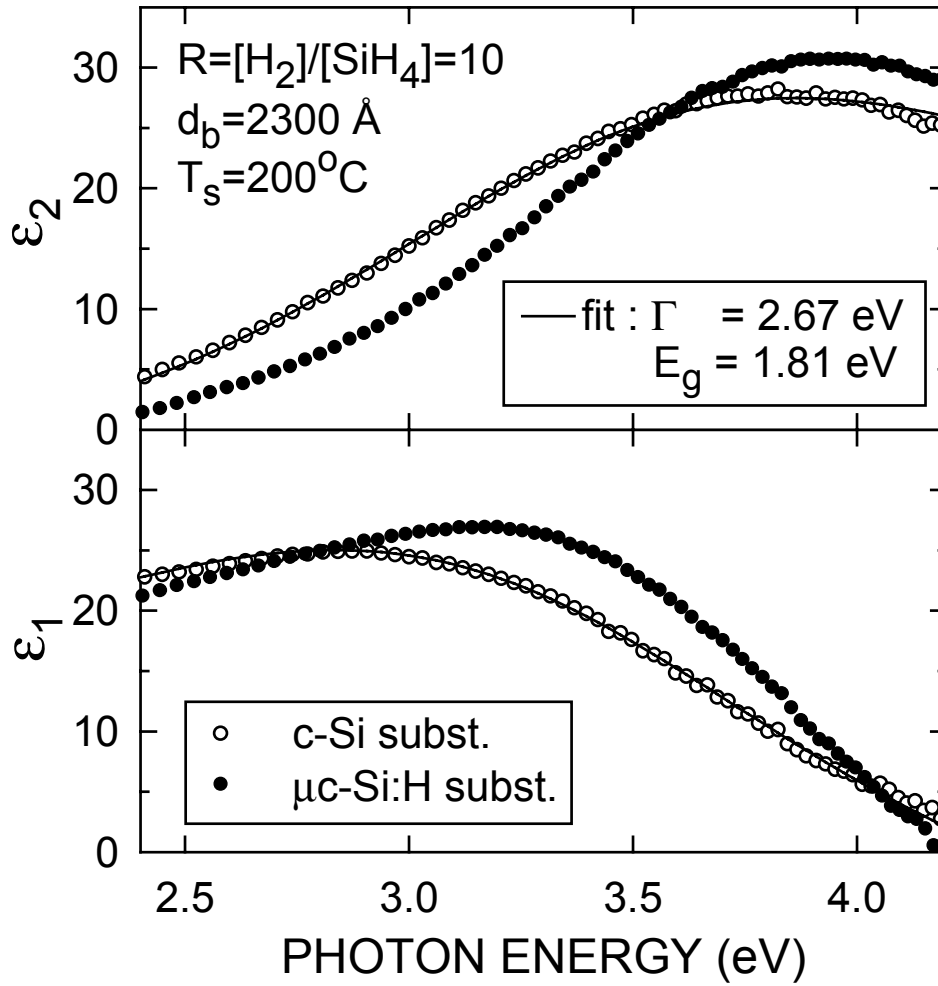


Figure I.1.3 Dielectric functions ϵ measured after a thickness of 2300 Å for Si films prepared at $R=10$ on a native oxide-covered c-Si substrate (open points) and on a μ c-Si:H ($R=200$) substrate film (solid points). The solid lines represent a best fit to the former results using the Tauc-Lorentz expression for an amorphous material, yielding the Tauc gap E_g and Lorentzian linewidth Γ .

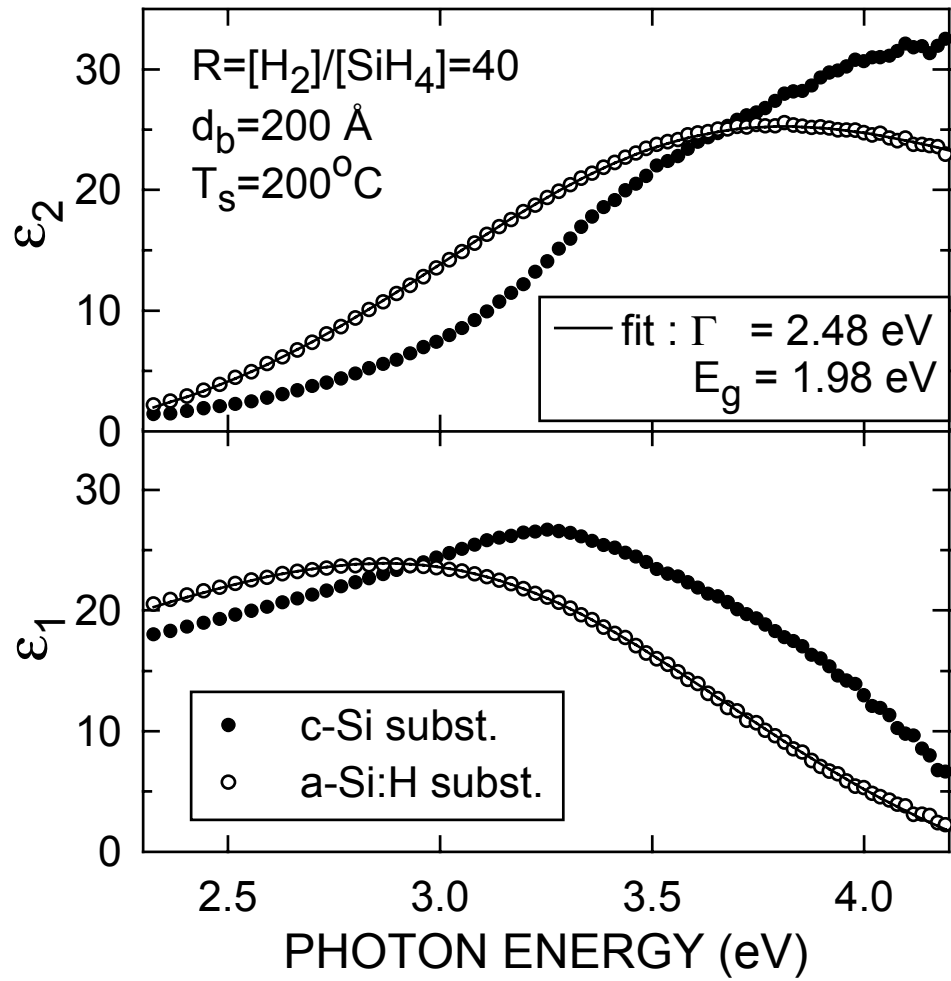


Figure I.1.4 Dielectric functions for 200 Å thick Si films prepared at $R=40$ on an a-Si:H ($R=0$) substrate film (open points) and on a native oxide-covered c-Si substrate (solid points). The solid lines represent best fits to the former results as in Fig. I.1.3.

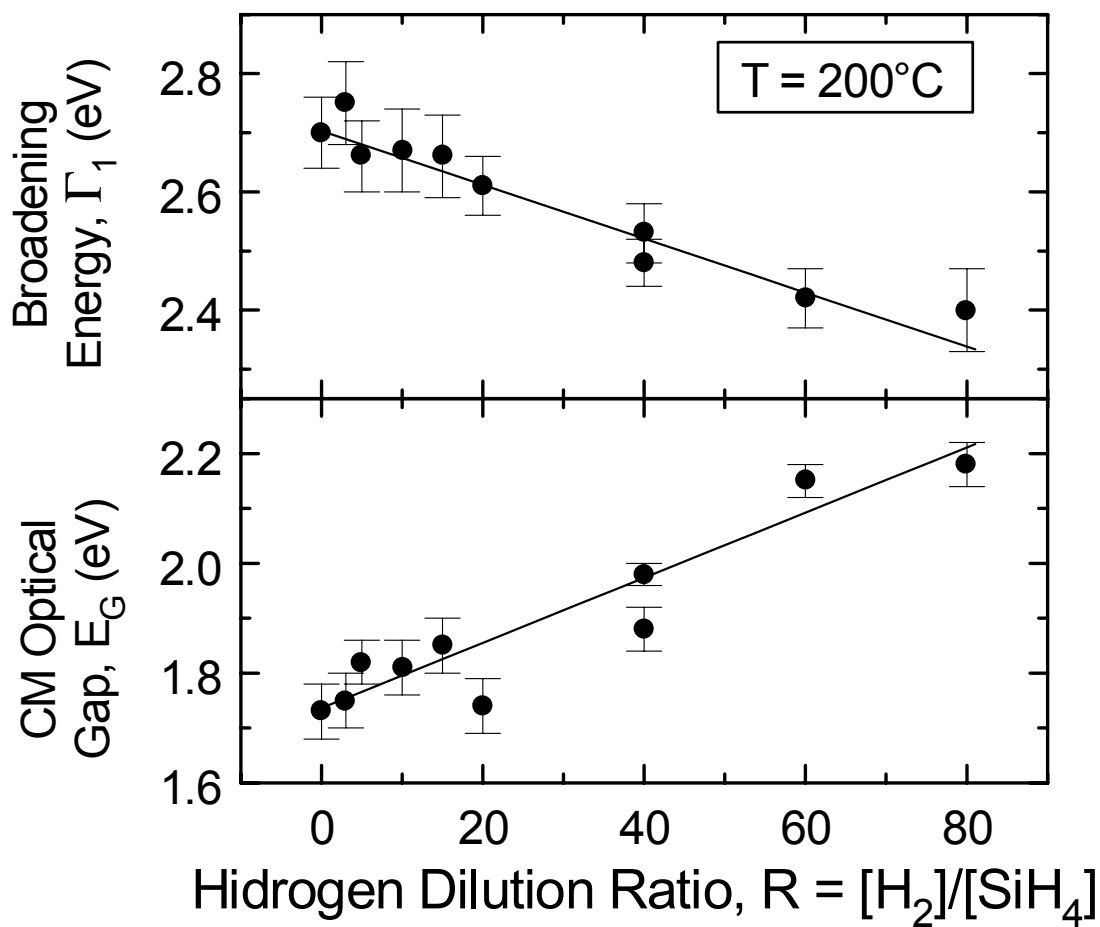


Figure I.1.5 Broadening parameter and optical gap at 200°C obtained in best fits to dielectric functions measured by real time SE for a series of a-Si:H films prepared as a function of the H_2 -dilution ratio $R=[H_2]/[SiH_4]$ on a-Si:H ($R=0$) substrate films.

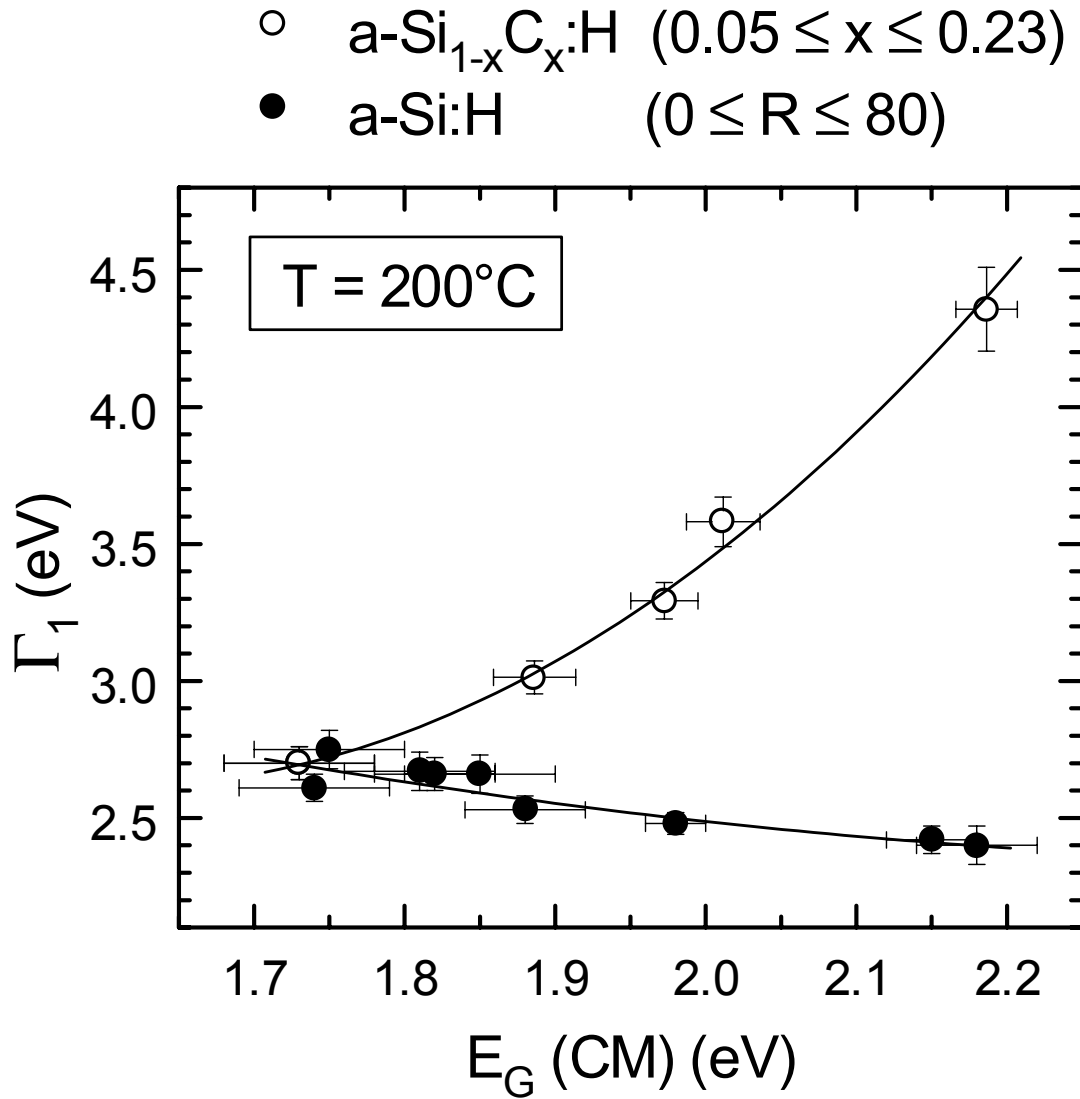


Figure I.1.6 Broadening parameter plotted versus optical gap at 200°C for $\text{a-Si}_{1-x}\text{C}_x\text{:H}$ ($0 \leq x \leq 0.23$) films prepared at different flow ratios $[\text{CH}_4]/\{[\text{SiH}_4] + [\text{CH}_4]\}$ from 0 to 0.8 (open circles) and for a-Si:H films prepared at different H_2 -dilution ratios $[\text{H}_2]/[\text{SiH}_4]$ from 0 to 80 (solid circles).

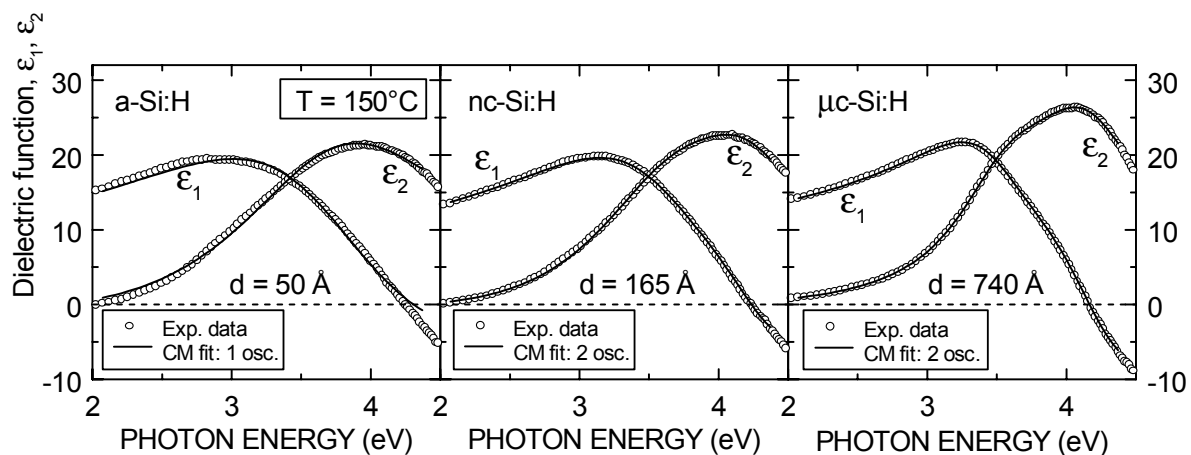


Figure I.1.7 Dielectric functions at 150°C deduced from real time SE data for the growth of a Si film on GaAs that spans the transition from a-Si:H ($d=50 \text{ \AA}$), through nc-Si:H ($d=165 \text{ \AA}$), to stable $\mu\text{c-Si:H}$ ($d=740 \text{ \AA}$). The solid lines are fits to the data using a one oscillator expression for a-Si:H and a two oscillator expression for nc-Si:H and $\mu\text{c-Si:H}$.

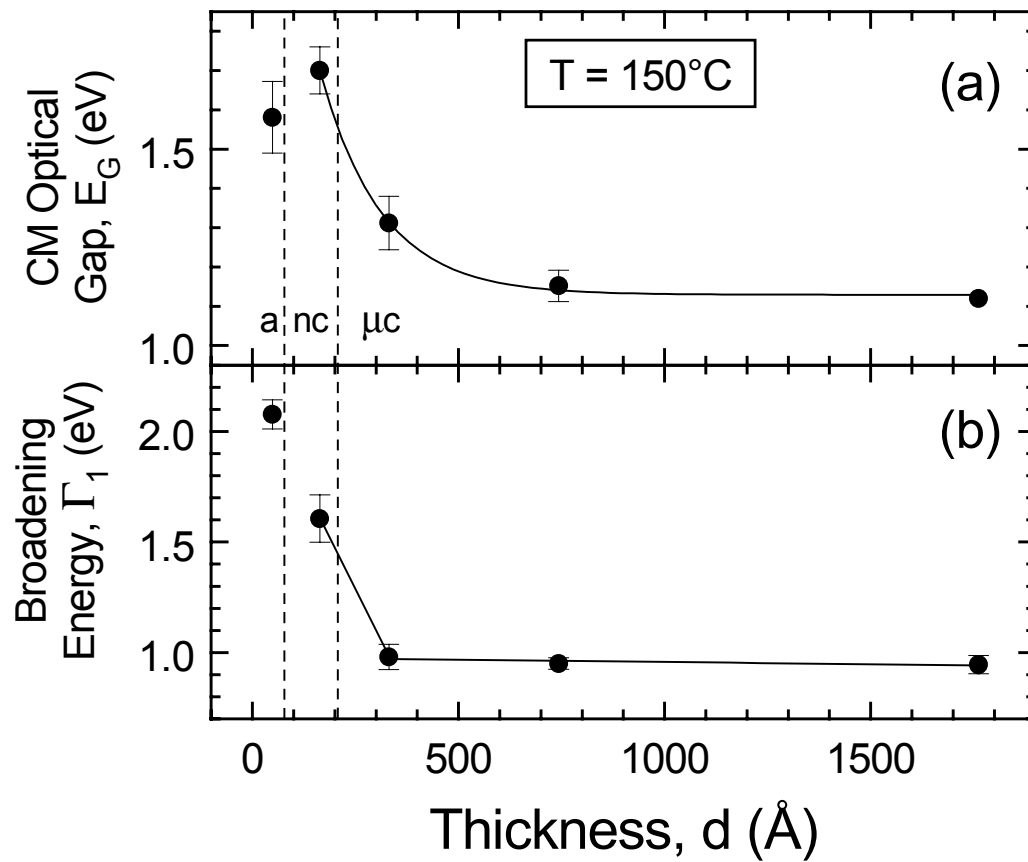


Figure I.1.8 (a) Optical gap and (b) Γ_1 broadening energy at 150°C plotted as a function of thickness during growth for the film of Fig. I.1.7.

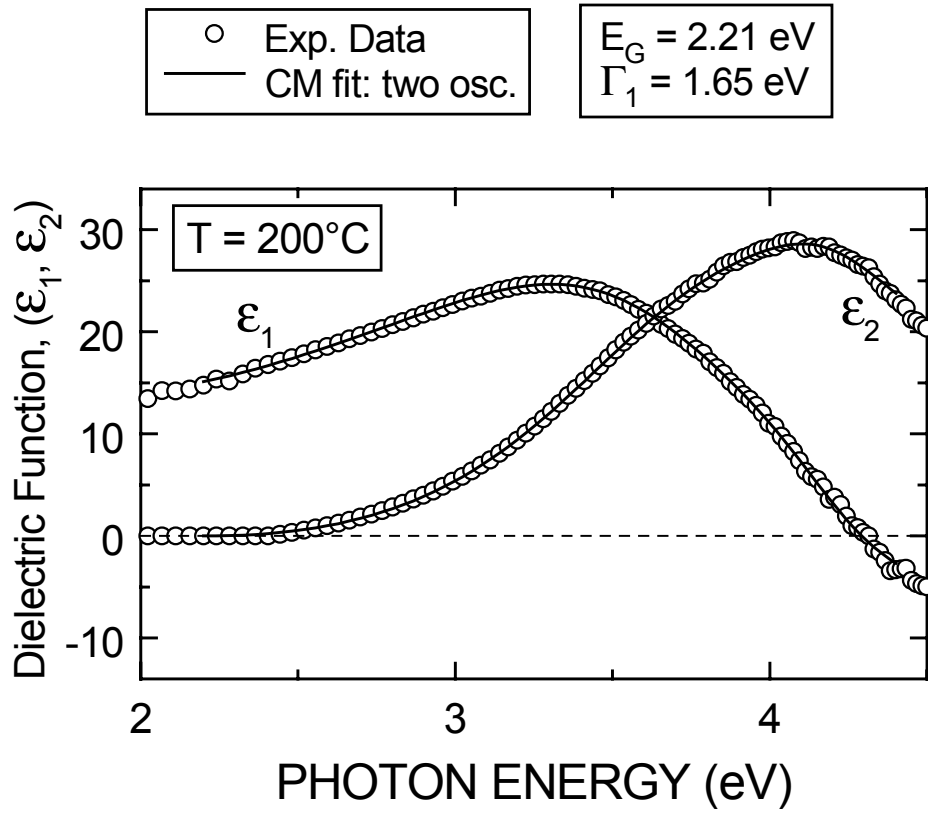


Figure I.1.9 Dielectric function at 200°C deduced from real time SE data for the growth of a 200 Å thick single-phase nc-Si:H film at $R=[\text{H}_2]/[\text{SiH}_4]=200$ on H_2 -plasma-treated a-Si:H. The solid lines represent a best fit to the data using a two-oscillator expression.

I.2. Evaluation of Optoelectronic Properties

Results and Discussion

Thin films of a-Si:H, prepared by PECVD under different conditions, have been characterized in detail to evaluate the properties related to solar cell performance. This is first done on the annealed state discussed here, as well as after 1 sun light-induced degradation discussed in Section 2 and Appendix I.

A methodology developed at Penn State University was used to reliably characterize the gap states in different a-Si:H films. This is based on transmission and reflection measurements (T&R) to obtain the energy dependence of optical functions for the materials such as refractive index, n , extinction coefficient, k , and optical absorption α . Then, dual beam photoconductivity (DBP) is used to measure the relative absorption in the subgap region ($\alpha(h\nu)$) at different carrier generation rates (G), whereby for $G \leq 10^{16} \text{ cm}^{-3} \text{ s}^{-1}$ the results are equivalent to those from CPM. Because of the importance of obtaining accurate values of $\alpha(h\nu)$, a novel method to accurately normalize DBP spectra with T&R spectra was developed at Penn State and is used in these studies [1]. In this method, the optical absorption caused by transitions from tail states to extended states is derived using constant dipole matrix elements. An iterative procedure is used to fit the optical absorption from T&R measurements and at the same time to extend it to exponential region using the slope obtained from DBP spectra. The DBP spectra are then aligned with the calculated $\alpha(h\nu)$ in exponential region, so minimum error is introduced. The characterization of the gap states consists of measuring the electron $\mu\tau$ products as a function of carrier generation rate, $\mu\tau(G)$, rather than just photoconductivity $\sigma(G)$, since the changes in $\mu\tau(G)$ are much pronounced and are thus a more accurate representation of the recombination kinetics. This methodology is applied for characterizing both the annealed state as well as the light-induced changes under 1 sun illumination. Detailed results of such a characterization carried out on USSC and PSU hydrogen-diluted a-Si:H films are presented in Appendix 1.

A comparison was made between hydrogen-diluted ($R=10$) materials from Penn State and “low” dilution materials from BP Solarex and Uni-Solar, where all of these materials have produced high performance solar cells. There are two interesting aspects to the results presented here for the annealed state. The first is the similarity of the three materials deposited under quite different conditions. The other is the difference the three materials exhibit in their relationships between $\mu\tau$ products and $\alpha(h\nu)$, in spite of the fact that the often misused term “device quality material” is relevant here. Fig. I.2.1 shows the $\mu\tau$ products as a function of generation rate G for the three materials in the annealed state. Compared to PSU diluted material, relatively higher electron $\mu\tau$ products are present in the BP Solarex material and lower electron $\mu\tau$ products in the USSC material. The results of Dual Beam Photoconductivity (DBP) measurements at low generation rate that corresponds to CPM, are shown in Fig. I.2.2. There is a clear discrepancy here with the commonly held view based on the “omnipotence” of the dangling bond, D^0 , states in that the BP Solarex material has both $\mu\tau$ products as well as subgap absorption at $\alpha(1.2\text{eV})$ higher than those from PSU material, and for Uni-Solar material both the $\mu\tau$ and $\alpha(1.2\text{eV})$ are lower. Such a presence of higher lifetimes with higher subgap absorption directly contradicts the still widely held view that these characteristics are determined solely by the D^0 states while ignoring the effects of charged defects. The dependence of a-Si:H material properties on charged defects is also found to dominate the characteristics of thin film materials from the Super Lab at ETL. In Fig. I.2.3, the $\mu\tau$ products are shown as function of generation rate G for one of the Super Lab a-Si:H films deposited at $T_s = 200^\circ\text{C}$. Also shown are the results for the PSU diluted $R=10$, undiluted, $R=0$, films prepared at $T_s = 200^\circ\text{C}$. Significant differences in the recombination kinetics are clearly indicated by the magnitude, and particularly by the shape of $\mu\tau(G)$ curves. It should be remembered that the key claim of the “ D^0 dominated model” is that $\mu\tau$ products are independent of G , i.e. γ is constant and equal to 1 [2]. The presence of charged defects is also evidenced from the more subtle differences in the subgap absorption spectra. Results from The Super Lab for the $T_s = 200^\circ\text{C}$, and from PSU for the $R=0$ and $R=10$ films of Fig. I.2.3 are shown in Fig. I.2.4, where the symbols are the experimental results. The subgap spectra obtained here

with DBP at a generation rate of $10^{15}\text{cm}^{-3}\text{s}^{-1}$, which is equivalent to that used in CPM, exhibit distinctly different dependences on photon energy. The differences in the fall off of $\alpha(h\nu)$ at low photon energies are indicative of the relative contribution from defects located above midgap. The contributions from these states are further enhanced at higher generation rates when these states become more occupied by electrons.

The results of subgap absorption and photoconductivity measurements ($\mu\tau$) have been analyzed using an improved Subgap Absorption Model (SAM) with a five Gaussian distribution of gap states. An iterative procedure for fitting of results such as in Fig. I.2.3 and Fig. I.2.4 is used to obtain a single set of “operational parameters” for the densities, distribution and carrier capture cross-sections of different gap states. An example of such self-consistent analysis is shown for the R=0 and R=10 materials in Fig. I.2.3, where the solid lines are fits to the experimental results for $\mu\tau$ versus G. The corresponding fits for $\alpha(h\nu)$ with identical parameters are shown in Fig. I.2.4. It should also be pointed out here that the parameters used here are also the same as those used to fit the I~V, QE and FF characteristics of corresponding Schottky barrier cell structures discussed in Section 2.

References

1. L. Jiao, I. Chen, R.W. Collins, and C.R. Wronski, “An Improved Analysis for Band Edge Optical Absorption Spectra in Hydrogenated Amorphous Silicon from Optical and Photoconductivity Measurements”, *Applied Physics Letters*, **72**, 1057-1058, (1998).
2. M. Stutzmann, W.B. Jackson and C.C. Tsai, “Light-induced Metastable Defects in Hydrogenated Amorphous Silicon: A systematic study”, *Physical Review B*, **32** 23-47 (1985).

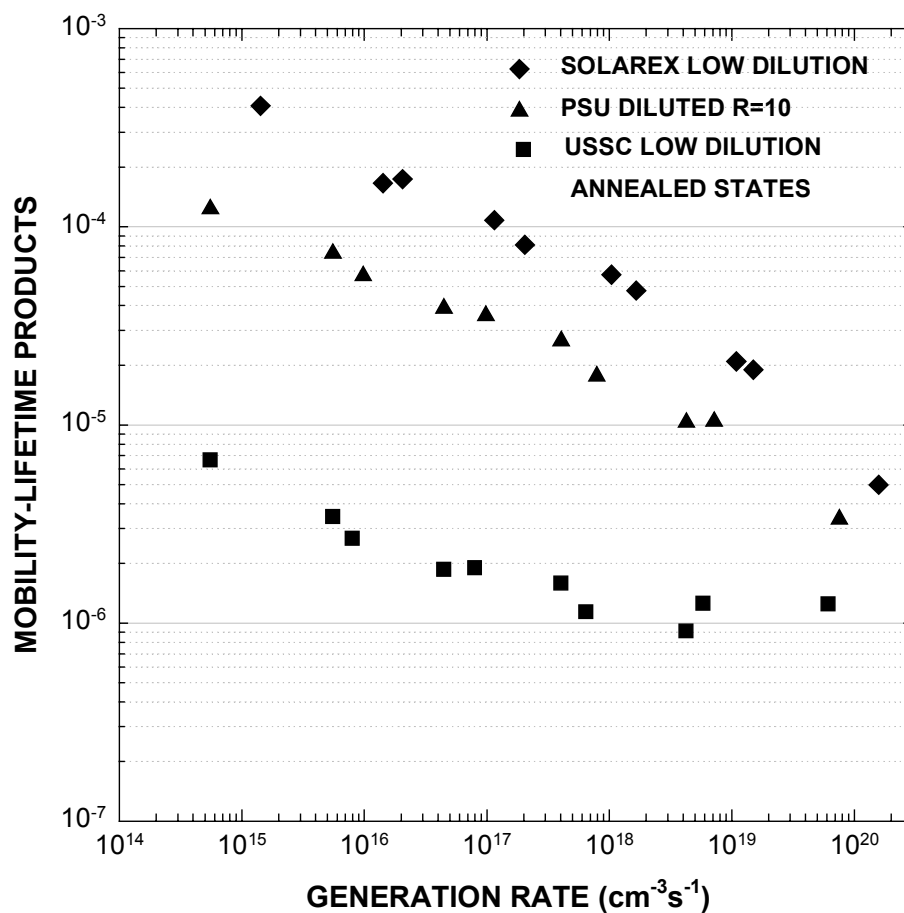


Figure I.2.1 Mobility-lifetime products of USSC low dilution, Solarex low dilution and PSU diluted R=10 in annealed state.

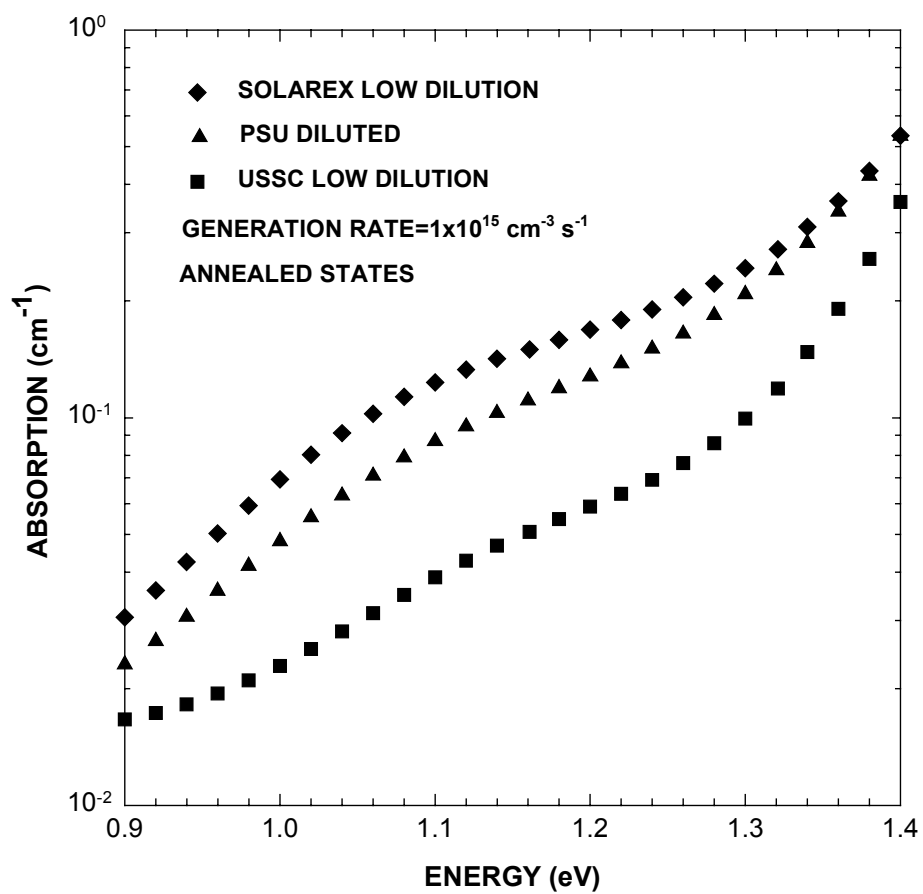


Figure I.2.2 Subgap absorption of USSC low dilution, Solarex low dilution and PSU diluted R=10 in annealed state.

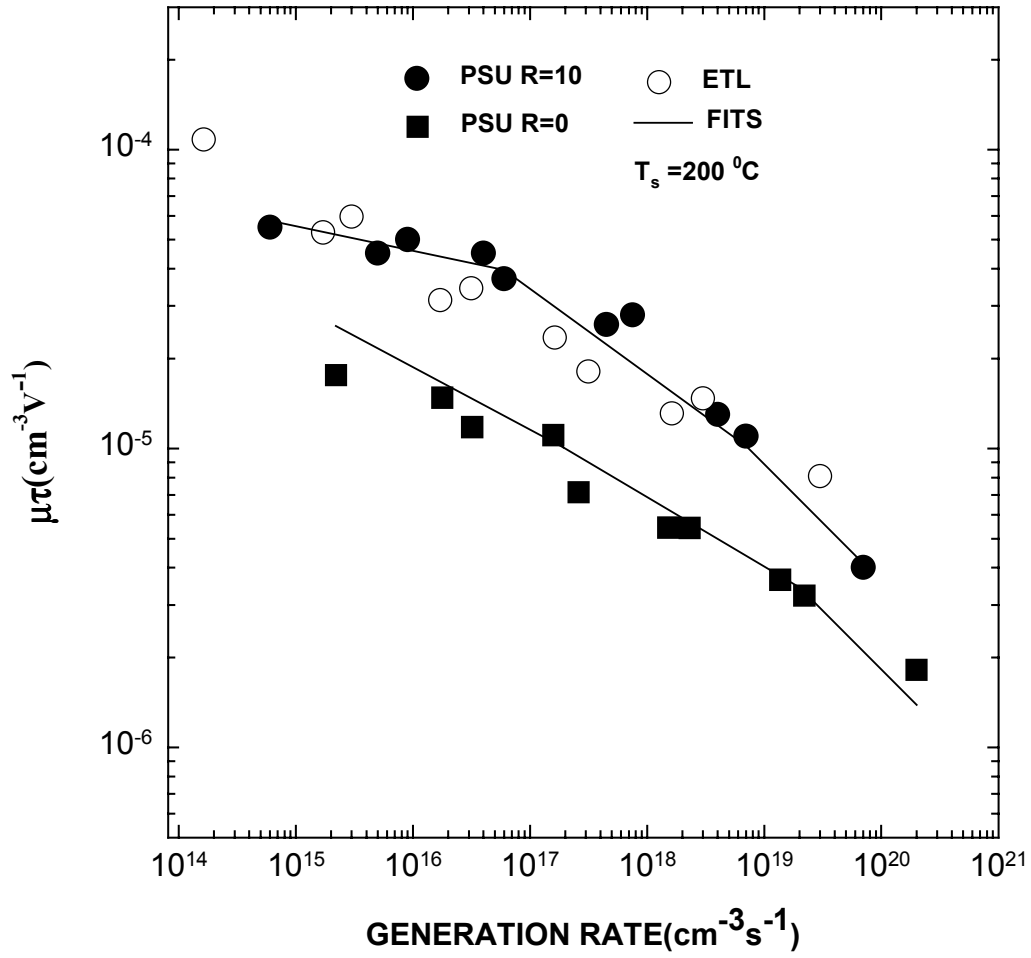


Figure I.2.3 Mobility-lifetime products of PSU R=10, 0 and ETL materials in annealed state. Symbols are experimental results and the lines are fits.

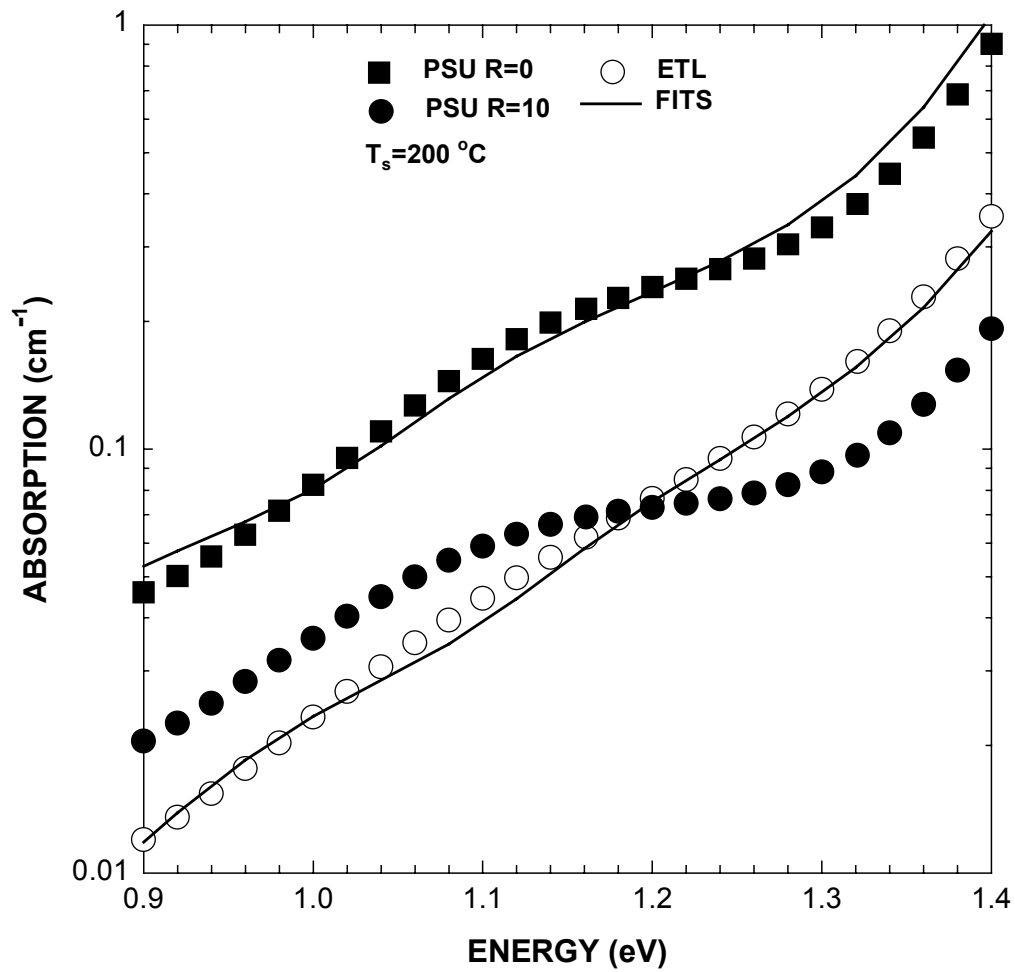


Figure I.2.4 Subgap absorption of PSU R=10, 0 and ETL materials in annealed state. Symbols are experimental results and lines are fits.

TASK II: Insights into Improved Stability in Materials and Solar Cells

II.1. Degradation Studies

Results and Discussion

The type, nature and densities of different light induced defects in optimized a-Si:H materials have been investigated and characterized. These studies have been carried out on films and corresponding Schottky barrier cell structures with different thicknesses of the intrinsic bulk layers. Taking into account the inadequacy of the approach based solely on “neutral dangling bonds”, the characterization was expanded in an attempt to include all gap states. We find that light-induced charged defects are as important as the neutral dangling bond defects in determining the properties and stability of a-Si:H materials and solar cells.

The light induced gap states have been characterized using the methodology described in Task I. This included the self-consistent fitting of all the results on films and corresponding Schottky barrier cell structures with a five Gaussian distribution of gap states. The studies on light-induced changes have been carried out with a-Si:H materials fabricated in different laboratories over a wide range of deposition conditions. Examples of the different light-induced changes in $\mu\tau$ products are shown in Fig. II.1.1 with results on BP Solarex, PSU and ETL materials. Fig. II.1.1 shows the $\mu\tau$ products at a generation rate of $G=1 \times 10^{19} \text{ cm}^{-3} \text{ s}^{-1}$ for two diluted and two undiluted materials as function of 1 sun illumination time and the two lines corresponding to $t^{-0.3}$ and $t^{-0.22}$ as guides for the eye. Although in the undiluted materials the degradation kinetics can be interpreted in terms of the “famous” $t^{-1/3}$ dependence, such a dependence is found only in undiluted materials and then at high generation rates such as this $1 \times 10^{19} \text{ cm}^{-3} \text{ s}^{-1}$, which is close to that of 1 sun. The PSU and BP Solarex diluted samples clearly show degradation kinetics which are significantly slower. These studies have also shown that the $\mu\tau$ products obtained at different generation rates exhibit quite different kinetics as seen in Fig. II.1.2, where the $\mu\tau$ products at $G=1 \times 10^{19}$ and $1 \times 10^{16} \text{ cm}^{-3} \text{ s}^{-1}$ are plotted as a function of 1 sun illumination time for the PSU undiluted film. A more detailed description of measurements and

results on light-induced changes is presented in Appendix I for diluted a-Si:H films from USSC and PSU. Such a wide range of kinetics, as well as the large, rapid light-induced changes under 1 sun illumination reported previously can not be explained by a D^0 dominated model, but are entirely consistent with the accompanying creation of charged defects. It can also be noted in Fig. II.1.1 that under 1 sun illumination at room temperature the diluted materials reach a degraded steady state in less than 100 hours, unlike the greater than 1000 hours for undiluted materials.

The importance of taking into account the effects of charged defects is also clearly evident in the detailed evaluation of results in the soaked states. After light-induced degradation and the creation of significant number of dangling bonds, their presence is reflected more strongly in the subgap absorption. Consequently, values such as $\alpha(1.2\text{eV})$ are an indication (not in an absolute terms though) of the densities of D^0 , but the subgap absorption also depends on the ratio between the densities of the charged defects and the neutral states. This results in subtle but real differences in the shape of the absorption spectra, which can be reconciled with the corresponding difference in $\mu\tau$ products. Results, such as obtained on PSU R=0 and R=10 films after 100 hours of 1 sun illumination, clearly show the similarity of subgap absorption in the two materials with both $\alpha(1.2\text{eV})$ values virtually equal to one. But as seen in Fig. II.1.1, the R=0 materials have $\mu\tau$ products significantly smaller than those of the R=10 material. Detailed self-consistent analysis indicates that the same densities of D^0 states have been created after the 100 hours 1 sun illumination in both materials, but that more charged defects are present in the R=0 case. It should be pointed out here also that the densities of dangling bonds deduced from the analysis are in very good agreement with those obtained from ESR measurements, which give densities of $8\sim 10 \times 10^{16} \text{ cm}^{-3}$ for the D^0 states for both materials. It is also important to note that even with these high densities of D^0 states, in p-i-n solar cells excellent fill factors are obtained with the R=10 material and not with the R=0 material, further showing the significance of the light-induced charged defects in degrading the performance of a-Si:H solar cells.

Another misconception about the creation of light induced defects is that there is only a limited number of sites available in a given a-Si:H material which can be converted into metastable defects. This is based in part on results which claim that there is no dependence of the degraded steady state densities of defects on either the light intensity or temperatures below 70 °C [Park et al., 1989]. This has in part been responsible for accepting accelerated tests of light-induced changes with high illumination intensities as being representative of the 1 sun degraded steady states (DSS) and the modeling predictions for end of life efficiencies. Despite the clear indications that this is certainly not true in solar cells [2], because of the very long times needed for undiluted a-Si:H films to reach the 1 sun degraded steady state (DSS), there have not been any independent verifications of such equivalence in films as well as the corresponding solar cells.

As part of the studies here, light-induced degradation with high intensity illuminations were also carried out on diluted films which reach the 1 sun degraded steady state in less than 100 hours at room temperature. Results on a PSU diluted a-Si:H film are shown in Fig. II.1.3 for the $\mu\tau$ products and for $\alpha(h\nu)$ in Fig. II.1.4 after 1 sun and 10 sun illumination. Degraded steady states for $\mu\tau$ products and $\alpha(h\nu)$ are reached with both 1 sun and 10sun illuminations, having clearly different values. In addition we find that the 1 sun light-induced changes, even between 25 °C and 75 °C have distinctly different degradation rates as well as values of the $\mu\tau$ products and $\alpha(h\nu)$ in their respective DSS. Because such dependence of light-induced changes on both temperature and light intensity, the arbitrarily chosen high intensity tests commonly used are irrelevant unless quantified with 1 sun DSS results. In the studies carried out here, the actual 1 sun DSS is evaluated and the defects are characterized with the detailed measurements and modeling of results on both films and Schottky barrier cell structures.

Extensive studies of light induced defects were carried out on diluted (R=10) Schottky barrier solar cell structures and the corresponding films. The measurements on Schottky barrier cell structures, which include forward I-V, light I-V and QE with different i layer thicknesses, are analyzed with results of $\mu\tau$ products and subgap absorption spectra obtained on the

corresponding films. The focus of the work here is mainly on the degraded steady state (DSS) obtained with 1 sun illumination at 25°C in films and Schottky barrier cells. All these results were analyzed using the distribution of gap states shown in Fig. II.1.5, where in addition to the neutral dangling bond D^0 states two gaussian distributions of defect states are introduced above and below midgap. Because of the large number of adjustable parameters associated with the energy locations, halfwidths, densities and carrier capture cross-sections of the different gap states, an iterative procedure was adopted for the self-consistent fitting of all the results on the thin films and the Schottky barriers using the same values for the parameters. In the process the relative sensitivity of the different results to specific gap state parameters was established and this is illustrated in Table I.

Table I. Parameters with largest effect on respective characteristics.

$\mu\tau$	Subgap	forward I-V	light I-V	QE
D^{+*} , D^0 , $D^+(E)$	D^0 , D^+ , D^-	$D^+(E)$, $D^{+*}(N)$	D^0 , D^{+*} , VB(tail)	α , D^0 , D^{+*} , VB(tail)

E: energy location only N: density only

The characteristics of Schottky barrier solar cell structures with different thickness protocrystalline ($R=10$) i layers, were fitted using the gap state distribution shown in Fig. II.1.5 and the same parameters were used in fitting the results on the thin film materials. This is discussed in detail in Appendix 2 with the I-V characteristic being discussed here.

As an example, the forward bias dark current characteristics are shown in Fig. II.1.6, where the symbols are the experimental results for cells with 0.2, 0.5 and 0.7 μm thick i-layers in the 1 sun degraded steady state (DSS). Also shown are results for the 0.7 μm cell in the annealed state (AS). At low forward bias, the currents are controlled by the Schottky barrier height for electron, $\phi_{\text{BN}}=0.97\text{eV}$, and have an exponential region before they become limited by the bulk, and thus the thicknesses of the i layers. In addition Fig. II.1.6 shows that the light induced defects have a very large effect whereby in the case of the 0.7 μm cell that the far forward bias

currents decrease over 5 orders of magnitude. The simulation results of these three cells, using the same “operational” parameters as in Fig. II.1.5, are shown as solid lines in Fig. II.1.6. Very good agreements are obtained for all three cells up to 2V.

Corresponding fits to the mobility-lifetime product ($\mu\tau$) and the subgap absorption with two generation rates for the corresponding R=10 thin film materials are shown in Fig. II.1.7, where the symbols are the experimental results and the lines are the fits using the same gap state parameters as used in Fig. II.1.6. It may be pointed out that the values of the $\mu\tau$ products at each generation rate correspond to an individual result, just as in the case of the quantum efficiencies for the different wavelengths. The good fits of both the $\mu\tau$ products and the subgap absorption using the same ‘operational’ gap state parameters as in the corresponding Schottky barrier solar cell structures clearly support the importance of including charge defects in any realistic characterization of gap state and their effect on cell performance. However the distribution of states chosen to represent charged defects is not unique but rather a possibility, nevertheless, the “operational” parameters such as derived here offer a more realistic and reliable approach for modeling of p-i-n and n-i-p solar cells characteristics in their degraded steady state.

A better understanding of the contributions that the different gap states make to the degradation will help to further quantify their parameters and to obtain self-consistent fits for all the cell characteristics. To assess the effects of the various gap states on the different film results and Schottky barrier cell characteristics, sensitivity studies were carried out where the values of the densities, energy positions and electron-hole capture cross-sections were individually changed. The results of these were used in obtaining the self-consistent fits to the Schottky barrier characteristics, presented in Appendix II, as well as the analysis of p-i-n solar cell characteristics discussed in Section 3.

References

1. H.R. Park, J.Z. Liu and S. Wagner, “Saturation of the Light-Induced Defect Density in Hydrogenated Amorphous Silicon”, *Appl. Phys. Lett.* 55, 2658-2660 (1989).
2. L. Yang, L. Chen and A. Catalano, “Intensity and Temperature Dependence of Photodegradation of Amorphous Silicon Solar Cells under Intense Illumination”, *Appl. Phys. Lett.* 59, 840-842 (1991).

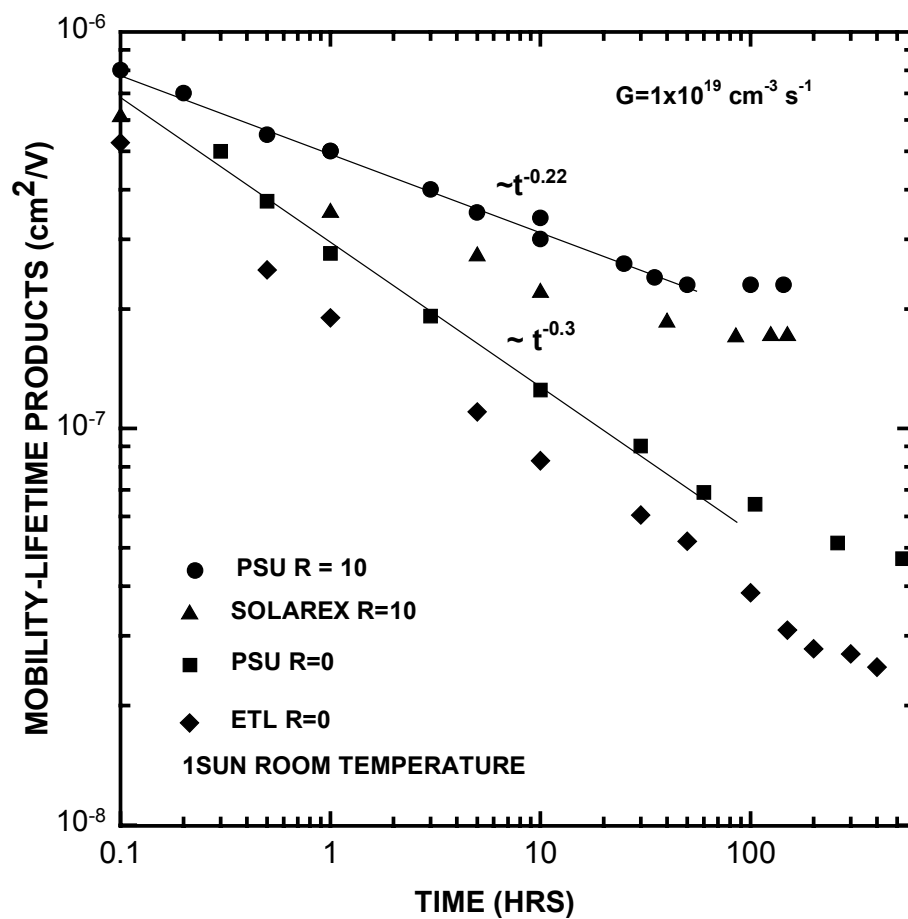


Figure II.1.1 Kinetics of light-induced changes of PSU R=10, 0, Solarex R=10 and ETL R=0 materials.

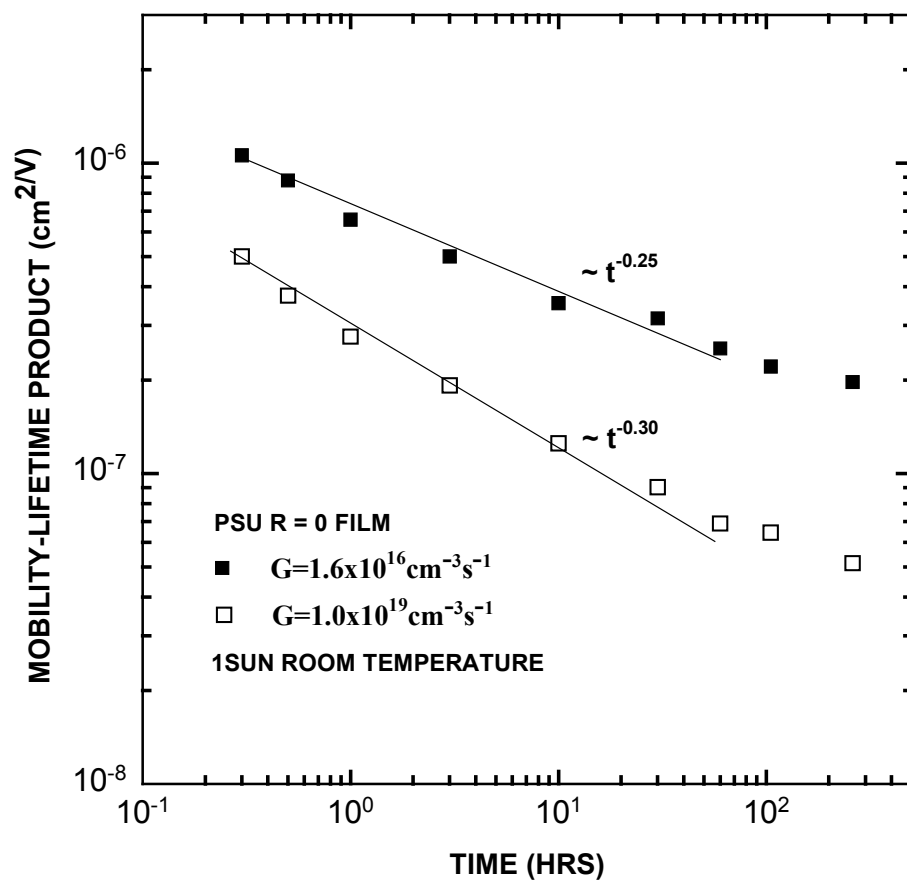


Figure II.1.2 Kinetics of light-induced change of PSU R=0 materials at two generation rates.

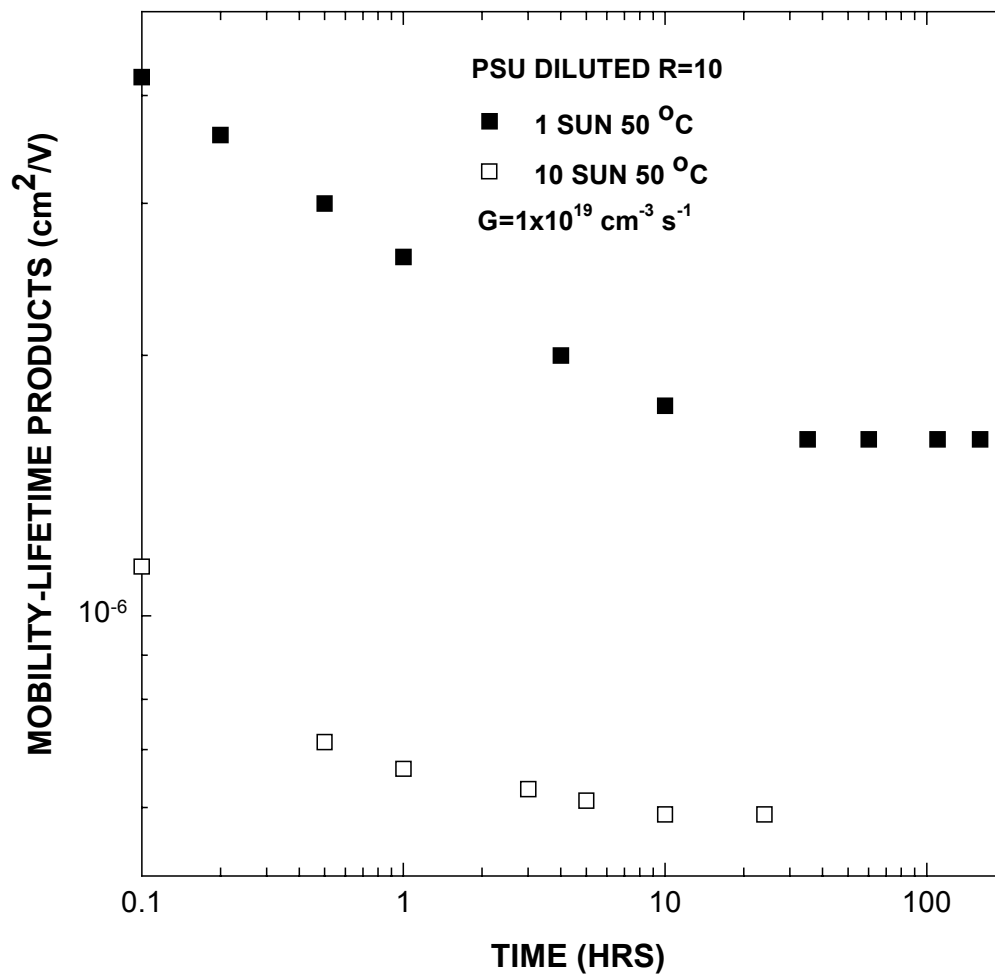


Figure II.1.3. Kinetics of light-induced changes of PSU R=10 materials at two light intensities.

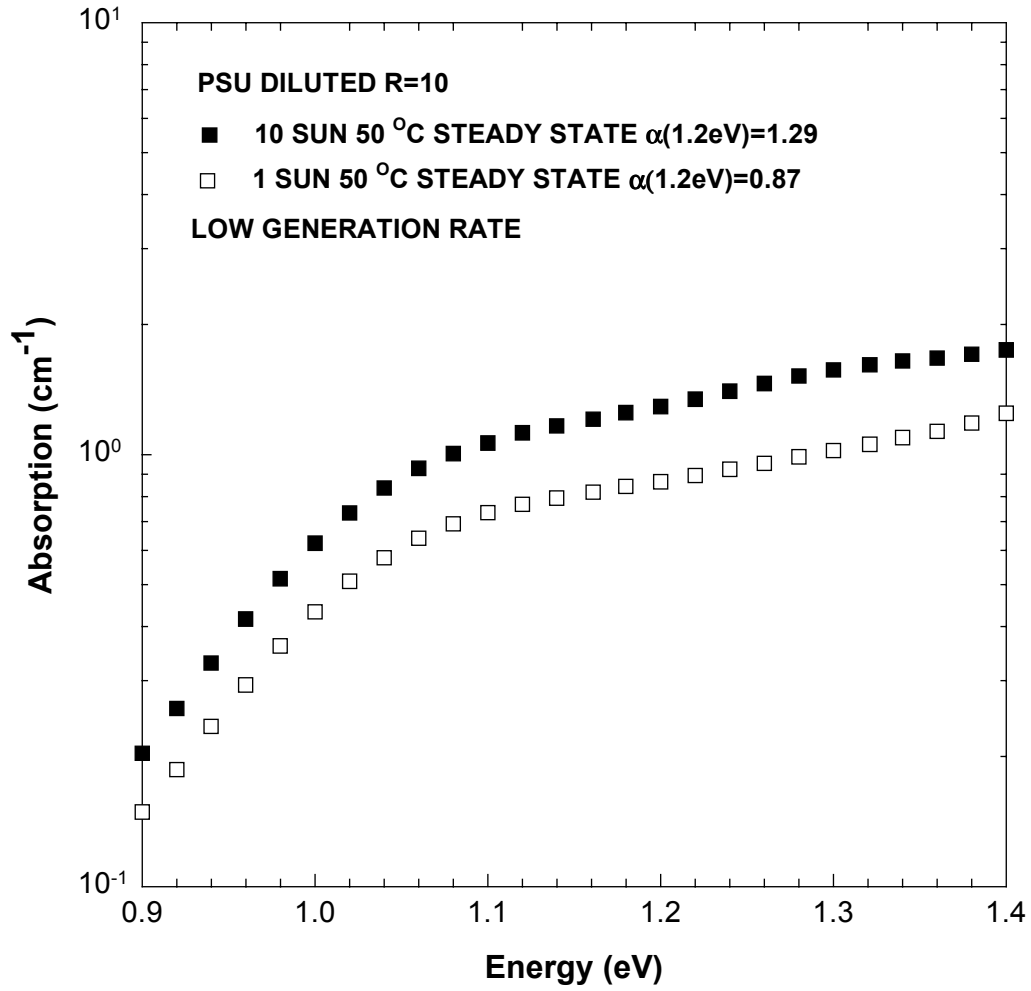


Figure II.1.4. Subgap absorption of PSU R=10 material in degraded steady state at 1 sun and 10 sun illumination.

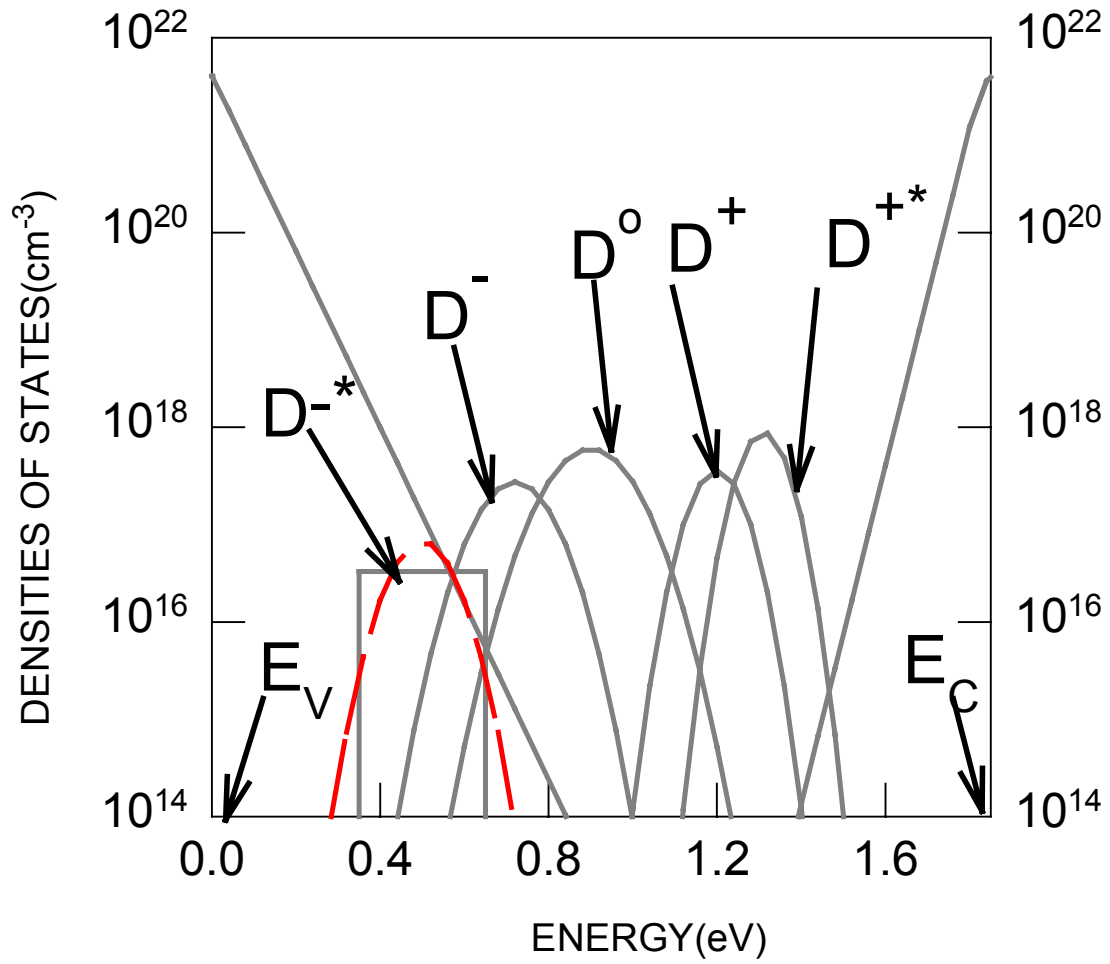


Figure II.1.5. Distribution of gap states used in the analysis of the Schotky barrier cell results in the 1 sun degraded steady state. D^0 are the neutral dangling bonds, D^{+} , D^{+*} are the positively charged and D^{-} , D^{-*} are the negatively charged states.

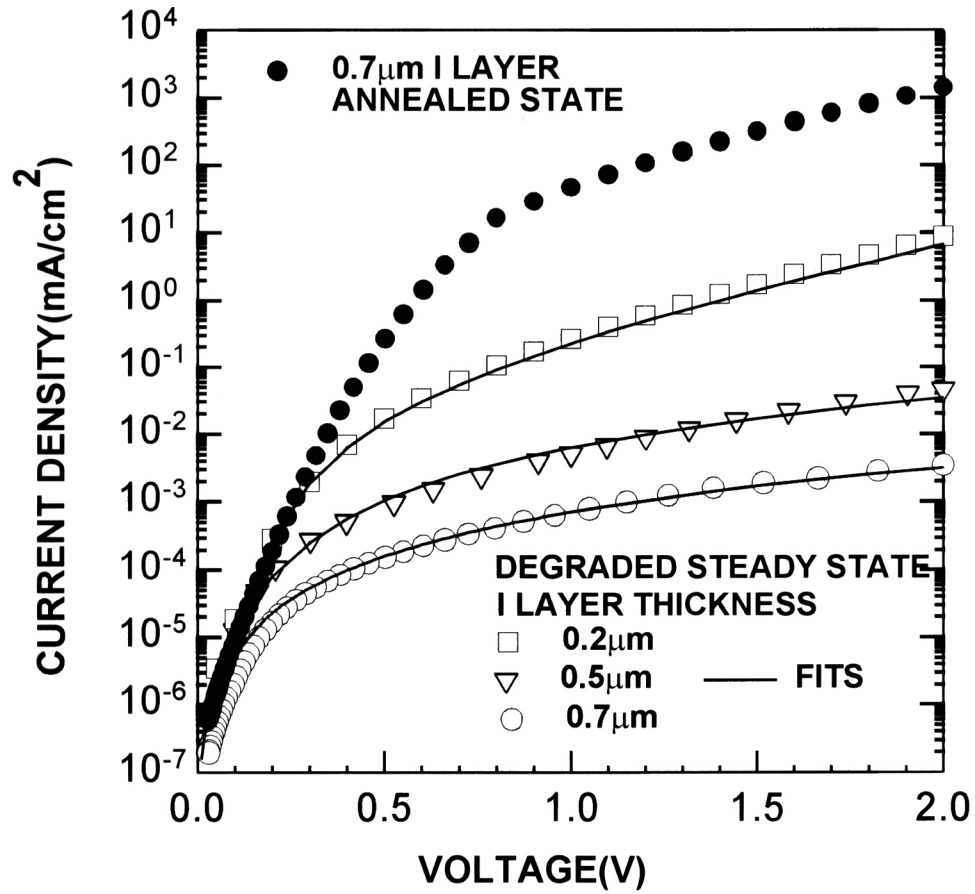


Figure II.1.6. Forward I-V characteristics of 0.2, 0.5 and 0.7 μm n-i Schottky barrier cells in the degraded steady state (DSS). Symbols are experimental results and solid lines are fits. Also shown are results for the 0.7 μm in the annealed state (solid symbols).

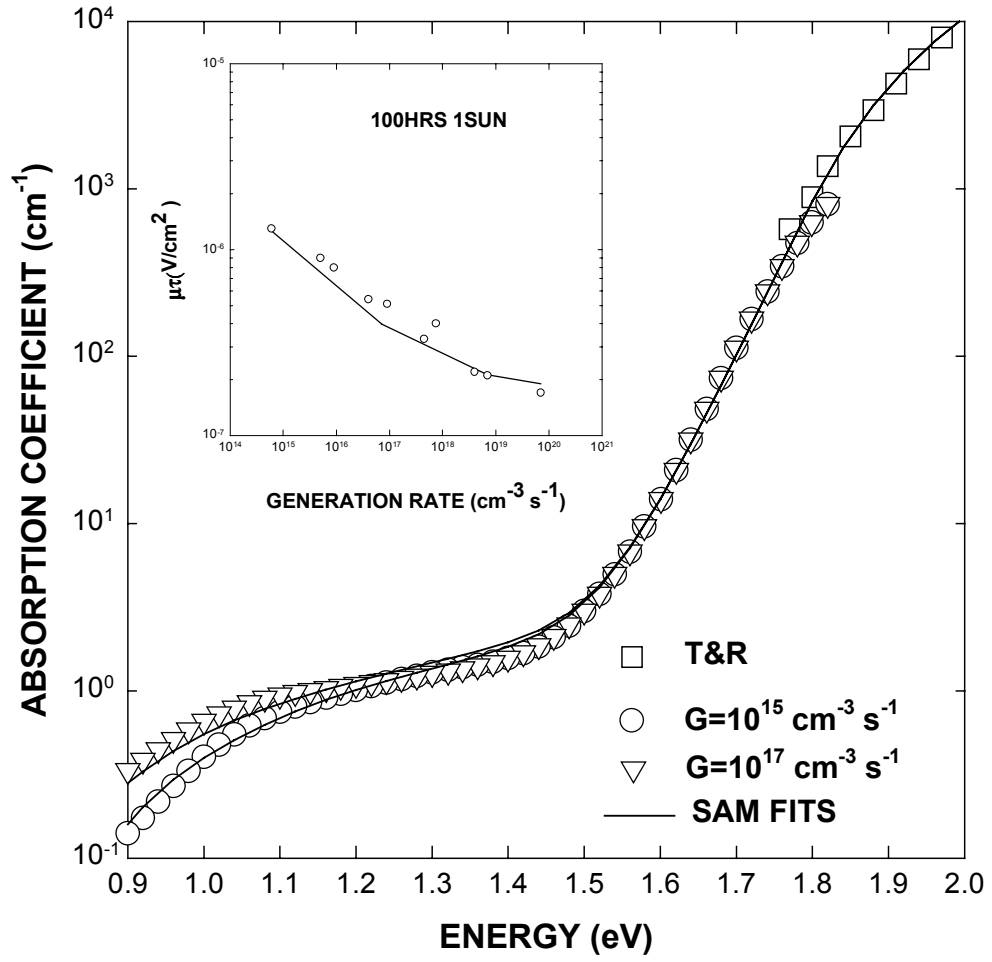


Figure II.1.7. Subgap absorption characteristics of PSU R=10 materials in the degraded steady state (DSS). Symbols are experimental results and solid lines are fits. Also shown are fit to mobility-lifetime products results in DSS.

TASK III: Optimization of Solar Cell Performance with Improved Intrinsic Layers

III.1. Optimization of p/i Interfaces

Motivation and Overview

Many studies relating the processing procedure to device characteristics have demonstrated the critical role of interfaces in the performance of hydrogenated amorphous silicon (a-Si:H) solar cells. [1] For example, controlled deposition of wider band gap layers at the p/i and i/p interfaces of a-Si:H p-i-n and n-i-p heterojunction solar cells has demonstrated effects on the open-circuit voltage V_{oc} at the monolayer (ML) level of incorporation. [2-4] Non-invasive real time spectroscopic ellipsometry (RTSE) is a powerful technique that can characterize changes in surface coverage on the order of 0.1 ML, and can provide the optical properties for layers as thin as ~ 5 Å. [5] In addition, the wide dynamic range of RTSE data provides the effective thickness evolution of a-Si:H films ranging from 0.1 Å to 5000 Å. In this Task, we have succeeded in identifying and quantifying three different effects that occur at the surface and sub-surface of the amorphous silicon-carbon (a-Si_{1-x}C_x:H) p-layer before a-Si:H i-layer deposition in the p-i-n solar cell configuration. These effects include (i) contamination of the p-layer surface, (ii) structural equilibration of the p-layer leading to H emission, and (iii) p-layer surface temperature variations. Only by separating the effects can RTSE unambiguously describe interface formation and thereby develop processing procedures for optimized devices.

Experimental Details

For the RTSE studies in which surface contamination dominates, 200 Å a-Si_{1-x}C_x:H p-layers were prepared by PECVD using diborane doping gas and flow ratios of [SiH₄]:[CH₄]:[B₂H₆]:[H₂] = 6:4:0.01:0.99 [in stand. cm³/min (sccm)]. Substrates for RTSE consist of 440 Å SnO₂:F on c-Si wafers, which provide relatively smooth surfaces

for p-layer overdeposition. [5] In the same runs, substrates for p-i-n solar cells were included, consisting of ~ 7500 Å $\text{SnO}_2\text{:F}$ layers on glass. Nominal substrate temperatures T_n of 250°C and 200°C were explored. A detailed description of the solar cell preparation appears elsewhere. [5,6] For RTSE studies of $\text{a-Si}_{1-x}\text{C}_x\text{:H}$ p-layer structural and thermal equilibration, 3000 Å p-layers were prepared on c-Si at $T_n=200^\circ\text{C}$ using trimethylboron doping gas and flow ratios of $[\text{SiH}_4]:[\text{CH}_4]:[\text{B}(\text{CH}_3)_3]:[\text{He}]=6:4:0.02:0.98$ (in sccm). In all depositions, the p-layer gas mixture at 0.13 Torr pressure was evacuated from the reactor immediately upon extinguishing the plasma, and replaced by a 100 sccm Ar purge at 0.69 Torr. The p-layer was maintained at T_n during the 50 min Ar purge before i-layer deposition.

RTSE was performed during $\text{a-Si}_{1-x}\text{C}_x\text{:H}$ p-layer preparation and Ar purging using a rotating-polarizer multichannel ellipsometer with acquisition times for spectra in the ellipsometry angles (ψ , Δ) from 0.8 to 3.2 s and repetition times from 3 to 120 s. [7] The spectral range of the ellipsometer for highest sensitivity is 1.5 to 4.0 eV. Data analysis procedures applied here are described in detail elsewhere. [5,6] Qualitative assessments of p-layer surface and sub-surface effects can be made from an inspection of the (ψ , Δ) trajectories at 2.5 eV, which are discussed and tabulated in the following.

Results and Discussion

First, we discuss processing of an $\text{a-Si}_{1-x}\text{C}_x\text{:H}$ p-layer prepared using B_2H_6 at 250°C . During the 50 min Ar purge of the reactor after p-layer PECVD on a c-Si/ $\text{SnO}_2\text{:F}$ substrate, (ψ , $|\Delta|$) at 2.5 eV exhibit continuous changes (final - initial) totaling $(-0.2^\circ, 1.8^\circ)$. We attribute the large increase in Δ to contamination of the p-layer *surface* by a SiB_x alloy film originating from residual species adsorbed on internal reactor walls and fixtures. [5,8] This conclusion is based on two observations. First, the large increase in Δ is not observed under identical p-layer PECVD and purging conditions when B_2H_6 is replaced by $\text{B}(\text{CH}_3)_3$, which is a more stable doping gas. Second, an even larger increase

in $|\Delta|$ ($>2^\circ$) characteristic of spontaneous SiB_x CVD is observed when the B_2H_6 containing p-layer gas mixture is not evacuated immediately upon plasma extinction. An analysis of the resulting thick contaminant film yields the dielectric function $\epsilon = \epsilon_1 + i\epsilon_2$ of the SiB_x material. The result is typical of an amorphous semiconductor, but with a broader and weaker ϵ_2 peak and a narrower $\epsilon_2^{1/2}$ optical gap than a-Si:H, suggesting high void and dopant contents. [8]

Figure III.1.1 shows contaminant film effective thicknesses d_{eff} versus time as deduced from analyses of RTSE data collected during Ar purging (circles). Purging is initiated at $t=0$ after preparation of the $\text{a-Si}_{1-x}\text{C}_x\text{:H}$ p-layers using B_2H_6 doping gas. These results were obtained from a two-layer model for the contaminant film, consisting of an interface roughness layer of thickness $d_i = 60\text{--}80$ Å and composition $(0.5/f_i/0.5-f_i)$ (p-layer/contaminant/voids) and an overlying surface roughness layer of thickness d_s and composition $(0.5/0.5)$ (contaminant/voids). [5] The Bruggeman effective medium theory is used to determine the dielectric functions of the composite layers from ϵ for the thicker SiB_x film. In Fig. III.1.1, $d_{\text{eff}} = f_i d_i + 0.5 d_s$ increases to 3.9 ± 0.1 Å and to 1.7 ± 0.1 Å after 50 min purges at $T_n = 250$ and 200°C , respectively. This result shows that although higher quality i-layers can be obtained at 250°C , [9] poorer quality p/i interfaces result owing to greater contamination of p-layers via adsorption of residuals. Figure III.1.1 also shows the evolution of d_{eff} for two cases in which the p-layer gas flow is continued even after extinguishing the p-layer plasma (triangles). A continuous build-up of SiB_x occurs at ~ 0.5 Å/min on a 250°C p-layer when using B_2H_6 for doping; however, no contamination occurs on a 200°C p-layer when using $\text{B}(\text{CH}_3)_3$.

To simplify study of the much weaker changes in Δ ($<0.5^\circ$) observed during Ar purging after $\text{a-Si}_{1-x}\text{C}_x\text{:H}$ p-layer preparation with $\text{B}(\text{CH}_3)_3$ doping gas, we used a structure consisting of a 3000 Å p-layer (opaque above 2.4 eV) on c-Si. For this structure, the change in (ψ, Δ) at 2.5 eV during the 50 min Ar purge is $(0.2^\circ, -0.2^\circ)$, whereas for contaminant film formation with $d_{\text{eff}} = 2$ Å the change is $(0.05^\circ, -1.5^\circ)$. Thus, we

conclude that $d_{\text{eff}} < 0.3 \text{ \AA}$ after the Ar purge. The relatively large change in ψ of 0.2° in this case is consistent with a *sub-surface* change in the $\text{a-Si}_{1-x}\text{C}_x\text{:H}$ p-layer properties during the Ar purge. [6] An analysis of RTSE data collected during p-layer growth yields ϵ at $T_n = 200^\circ\text{C}$ and the p-layer surface roughness thickness. Assuming that the change in (ψ, Δ) upon Ar purging arises solely from a sub-surface effect, then ϵ at the end of the Ar purge can be determined as well. A comparison of the dielectric functions just before and after the Ar purge reveals a narrowing of the $\text{a-Si}_{1-x}\text{C}_x\text{:H}$ p-layer optical gap and an increase in the amplitude of ϵ upon purging. We interpret such behavior by considering that a chemical equilibrium of H exists between the plasma and the sub-surface of the growing p-layer. [10] Upon extinguishing the plasma, this equilibrium is no longer sustained, and emission of bonded H occurs from the p-layer into the vacuum from a depth equal to the H mean free path in the p-layer (200-400 \AA). The loss of H is accompanied by structural equilibration in which Si-Si bonds reconstruct.

We have applied two methods for kinetic analysis of bulk $\text{a-Si}_{1-x}\text{C}_x\text{:H}$ p-layer modification by this effect. [6] In Fig. III.1.2 (triangles), we show the time evolution of the $\epsilon_2^{1/2}$ optical gap in the first 25 min of the Ar purge. The optical gap shows initial rapid narrowing followed by a relatively stable regime, and a total change of -0.03 eV . Using the correlation between the gap and H-content for as-deposited films, [11] this corresponds to a loss in H-content by $\sim 2 \text{ at.}\%$. In an alternative analysis method, we have employed the p-layer ϵ spectra before and after Ar purging to extract a Kramers-Kronig (K-K) consistent dielectric response [12] associated with the unstable Si-H bonds that are lost upon purging. From this response, the time evolution of the change in volume fraction associated with the unstable Si-H bonds can be determined as shown in Fig. III.1.2 (circles). We have fit the results over a 50 min purge to a sum of two emission rates, yielding time constants of 1×10^{-2} and $8 \times 10^{-4} \text{ s}^{-1}$. Assuming an attempt frequency in the range 10^{12} - 10^{13} s^{-1} , the activation energy for the fast process is $1.36 \pm 0.05 \text{ eV}$, which

is consistent with that of H diffusion in p-type a-Si:H. [13]

The H-emission effect upon plasma extinction was detected for a-Si_{1-x}C_x:H p-layers prepared using B(CH₃)₃ doping gas but not for undoped a-Si_{1-x}C_x:H. Our results are consistent with earlier studies of a-Si:H p-layers prepared using B₂H₆ that found (i) H-evolution from the p-layer after deposition when it was maintained at substrate temperature [14] and (ii) a dependence of the p-layer properties on intermission time for intermittent PECVD. [15] Thus, we conclude that H-emission is a general feature of a-Si:H based p-layers. The effect was not detected in the studies of p-layers prepared using B₂H₆, owing to the dominant effect of contaminant formation on the RTSE data.

The surface of a fully equilibrated a-Si_{1-x}C_x:H p-layer prepared using B(CH₃)₃ doping gas was studied after the 50 min Ar purge. We first evacuated the Ar and reintroduced the p-layer gas without igniting a plasma, then repeated the Ar purge in the absence of the H-emission effect, and finally introduced the i-layer gas (pure SiH₄) in an attempt to identify sub-ML contamination. In this experiment, (ψ , Δ) at 2.5 eV changed by (0.04°, -0.04°), upon introduction of the Ar and remained nearly stable thereafter. Further repetitions of this experiment showed that the changes in the RTSE data were reversible, in contrast to the H-emission effect, and that these changes tracked the substrate surface temperature as read by a thermocouple mounted on the substrate holder. Thus, the changes in RTSE data were attributed to temperature changes at the near-surface of the p-layer.

To quantify such changes, we have obtained ϵ for the a-Si_{1-x}C_x:H p-layer at different stabilized true temperatures T using a c-Si wafer as a calibration standard. [6] A parameterization of the ϵ spectra has been undertaken using K-K consistent expressions of Ref. [12]. Fitting the five free parameters in these expressions to linear functions of T yields sufficient information to compute ϵ for any value of T between 50 and 200°C. This allows us to incorporate T as a free parameter in the data analysis. The final results, shown in Fig. III.1.3(a), demonstrate that the 0.04° increase in $\psi(2.5 \text{ eV})$ corresponds to

an increase in T from 193 to 200°C owing to the addition of Ar at higher pressure, which improves the thermal contact between the sample and its holder. Figure III.1.3(b) shows concurrent temperature data measured by thermocouples at the surface and bulk of the sample holder, with the bulk one yielding T_n for temperature control. The validity of the RTSE analysis is confirmed by the excellent agreement between the variations in Figs. III.1.3(a) and (b) in spite of the 12°C difference, which is attributed to poor thermal contact of the surface-mounted thermocouple. The longer term fluctuations of $\sim 1\text{-}2^\circ\text{C}$ that appear in Figs. III.1.3(a) and 3(b) originate from the temperature controller. These are detected at the precision limit of RTSE [0.005° in $\psi(2.5\text{ eV})$]. Finally, since the changes in (ψ, Δ) can be fully accounted for by variations in T , we conclude that *the contamination level of the p-layer surface is $< 0.1\text{ \AA}$ (or 0.05 ML) during the 50 min Ar purge.*

Next, we describe the implications of our overall results for solar cell fabrication. It is known that contamination is the origin of p/i interface defects that reduce V_{oc} of the solar cell. [16] Cells in the p-i-n configuration in which the contaminant film thickness has been reduced from 3.9 \AA (B_2H_6 , 250°C) to $< 0.3\text{ \AA}$ [$\text{B}(\text{CH}_3)_3$, 200°C] exhibit increased V_{oc} from 0.74 to 0.84 V. [5] It is expected that the H-emission effect is also detrimental to V_{oc} since the $\text{a-Si}_{1-x}\text{C}_x\text{:H}$ p-layer optical gap decreases, and the equilibrated network may exhibit a higher dangling bond density. We find that a H_2 plasma treatment of the p-layer just prior to i-layer deposition is beneficial in reversing these effects. [6] In fact, a 6 min treatment using the same plasma power as the i-layer (50 mW/cm^2), when applied to a p-layer from $\text{B}(\text{CH}_3)_3$ at 200°C, has led to a further increase in V_{oc} to 0.87 V. Higher V_{oc} still results by improving the i-layer side of the interface using protocrystalline layers as described in Sec. I.1. [17]

Concluding Remarks

In summary, we have applied RTSE for separating the various effects on the apparent

optical properties of the near-surface of a-Si_{1-x}C_x:H p-layers, prepared and processed under different conditions for incorporation into p-i-n solar cells. As shown by the data in Table I obtained at a photon energy of 2.5 eV, contamination is the dominant effect at the surfaces of p-layers prepared using B₂H₆. This can be avoided with the use of B(CH₃)₃, leading to clean surfaces that allow detection of sub-surface equilibration of Si-Si and Si-H bonding upon terminating the plasma. Once the p-layer network has equilibrated, the remaining optical changes can be attributed to true temperature variations during reactor purging at the level of $\pm 1^\circ\text{C}$. Thus under best case conditions, an upper limit of 0.1 Å for contaminant formation at the p/i interface can be established.

References

1. W. Luft and Y. Tsuo, *Hydrogenated Amorphous Silicon Deposition Processes*, (Marcel Dekker, New York, 1993).
2. N. Bernhard, G. H. Bauer, and W. H. Bloss, Prog. Photovoltaics Res. Appl. **3**, 149 (1995).
3. R. E. I. Schropp, J. D. Ouwers, M. B. von der Linden, C. H. M. van der Werf, W. F. van der Weg, and P. F. A. Alkemade, Mater. Res. Soc. Symp. Proc. **297**, 797 (1993).
4. H. Fujiwara, J. Koh, J. S. Burnham, C. R. Wronski, and R. W. Collins, Appl. Phys. Lett. **72**, 2993 (1998).
5. J. Koh, Y. Lu, S. Kim, J. S. Burnham, C. R. Wronski and R. W. Collins, Appl. Phys. Lett. **67**, 2669 (1995).
6. H. Fujiwara, J. Koh, Y. Lee, C. R. Wronski, and R. W. Collins, J. Appl. Phys. **84**, 2278 (1998).
7. I. An, Y. M. Li, H. V. Nguyen, and R. W. Collins, Rev. Sci. Instrum. **63**, 3842 (1992).
8. R. W. Collins, Appl. Phys. Lett. **53**, 1086 (1988).
9. Y. M. Li, I. An, H. V. Nguyen, C. R. Wronski, and R. W. Collins, Phys. Rev. Lett. **68**,

- 2814 (1992).
10. R. A. Street, Phys. Rev. B **43**, 2454 (1991).
 11. L. Ley in *The Physics of Hydrogenated Amorphous Silicon II*, Vol. 56, edited by J.D. Joannopoulos and G. Lucovsky (Springer, Berlin, 1984), p. 61.
 12. G. E. Jellison, Jr., and F. A. Modine, Appl. Phys. Lett. **69**, 371 (1996); 69, 2137 (1996).
 13. R. A. Street, C. C. Tsai, J. Kakalios, and W. B. Jackson, Philos. Mag. B **56**, 305 (1987).
 14. W. Beyer, H. Wagner, and H. Mell, Solid State Commun. **39**, 375 (1981).
 15. T. Kamei, N. Hata, and A. Matsuda, J. Non-Cryst. Solids **198-200**, 999 (1996).
 16. A. Catalano and G. Wood, J. Appl. Phys. **63**, 1220 (1988).
 17. J. Koh, Y. Lee, H. Fujiwara, C. R. Wronski, and R. W. Collins, Appl. Phys. Lett. **73**, 1526 (1998).

Table I. Approximate changes in the ellipsometric parameters (ψ , Δ) measured at 2.5 eV generated by different effects detected during Ar purging immediately after the preparation of opaque a-Si_{1-x}C_x:H p-layers.

p-Layer Effect	Magnitude of Effect	Optical Change in (ψ, Δ)
Surface contamination	1 Å in d_{eff}	(0.03°, -1°)
Hydrogen emission	~1 at. % H	(0.1°, -0.1°)
Temperature variation	+2°C	(0.01°, -0.01°)

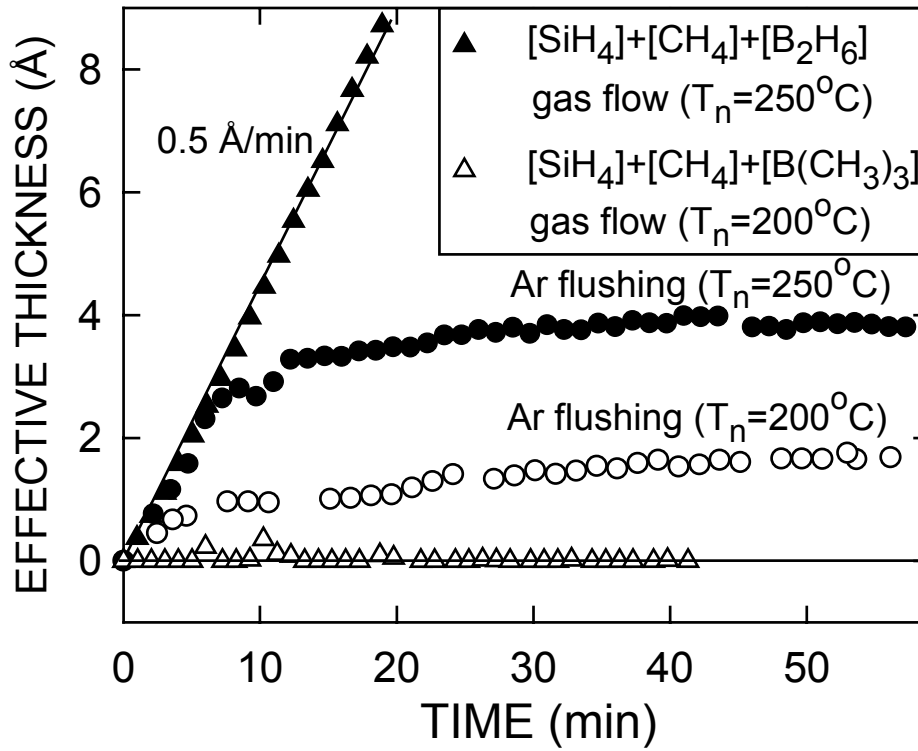


Figure III.1.1 Time evolution of the effective thicknesses of SiB_x contaminant layers that form on $\text{a-Si}_{1-x}\text{C}_x\text{:H}$ p-layers prepared by PECVD using B_2H_6 at $T_n=200^\circ\text{C}$ (open circles) and 250°C (filled circles). At $t=0$, the plasma is extinguished and the p-layer gas mixture is replaced by Ar for reactor purging. Also shown are the data collected upon extinguishing the p-layer plasma and continuing the deposition gas flow for the case of B_2H_6 at 250°C (filled triangles) and $\text{B}(\text{CH}_3)_3$ at 200°C (open triangles). During purging, the p-layer is maintained at T_n in all cases.

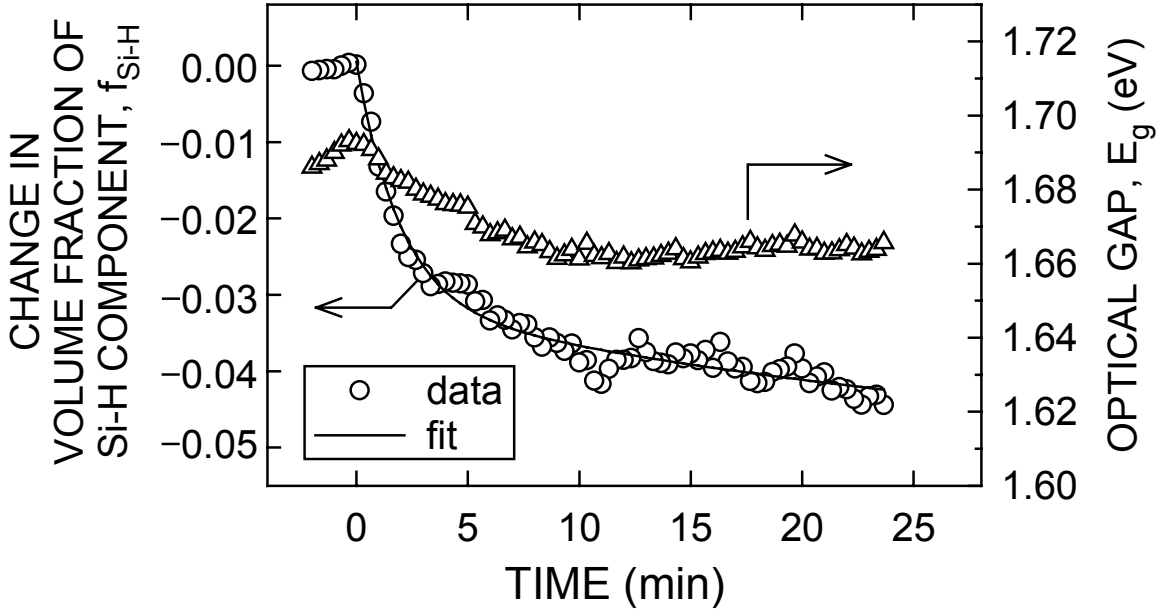


Figure III.1.2 Time evolution of the $\epsilon_2^{1/2}$ optical gap (triangles) and the change in volume fraction of the Si-H component (circles) during Ar purging for an $a\text{-Si}_{1-x}\text{C}_x\text{:H}$ p-layer prepared using $\text{B}(\text{CH}_3)_3$. These variations characterize structural equilibration of the p-layer. At $t=0$, the plasma is extinguished and the p-layer gas is replaced by Ar for reactor purging. During purging, the surface of the p-layer is maintained at $T_n=200^\circ$. The solid line represents a fit to the Si-H component volume fraction assuming two reaction rates for H-emission.

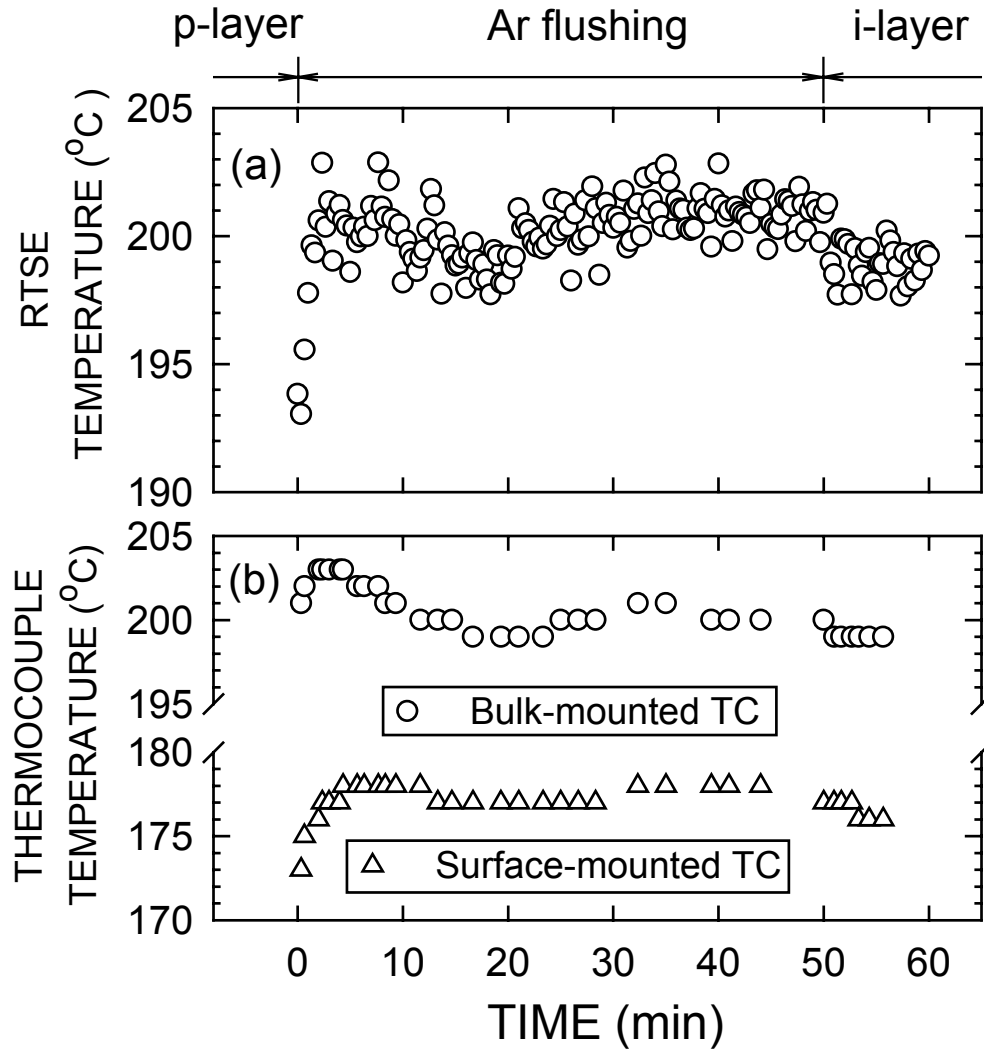


Figure III.1.3 Time evolution of the substrate temperature for an equilibrated $a\text{-Si}_{1-x}\text{C}_x\text{:H}$ p-layer as determined by (a) RTSE (yielding the true temperature T), (b) a thermocouple mounted at the surface of the substrate holder, and a thermocouple embedded within the substrate holder (yielding the nominal temperature T_n). In this experiment, the gases used for preparation of the p-layer are evacuated and replaced by Ar to initiate purging at $t=0$. SiH_4 is introduced at $t=50$ min to begin i-layer preparation.

III.2. p-Layers for n-i-p Solar Cells

Motivation and Overview

An important goal in the development and optimization of hydrogenated amorphous silicon (a-Si:H) substrate/(n-i-p) devices such as solar cells is the deposition of thin (100-200 Å) single-phase microcrystalline silicon ($\mu\text{c-Si:H}$) p-layers by plasma-enhanced chemical vapor deposition (PECVD) directly on top of a-Si:H i-layers at high nucleation density.[1] This goal is motivated by the fact that $\mu\text{c-Si:H}$ can be doped more efficiently than a-Si:H, and higher conductivities can be achieved. Such an improvement in doping can be exploited in a device, however, only if the crystallites nucleate immediately on the i-layer and coalesce to form a continuous p-layer within a thickness of < 100 Å. Three different dopant source gases, B_2H_6 , $\text{B}(\text{CH}_3)_3$, and BF_3 , can be used in the deposition of $\mu\text{c-Si:H}$ p-layers, yet few detailed studies of the resulting p-layers are available that compare the growth processes and properties for the thin layers in the actual device configuration, i.e., for < 200 Å thick p-layers on a-Si:H substrate films.

The use of B_2H_6 as a dopant source gas for p-type a-Si:H and $\mu\text{c-Si:H}$ deposition has a number of problems, including (i) contamination of film surfaces and interfaces due to spontaneous chemical vapor deposition (CVD), [2-4] (ii) clogging of flowmeters by decomposed gas, leading to controllability problems, (iii) possible incorporation of B–B bonds in the film, [5] and (iv) a narrow range in gas flow for optimum nucleation and growth. [6] Alternative dopant source gases have been employed to avoid these problems. For example, $\text{B}(\text{CH}_3)_3$ is a more stable gas that has been used often in the preparation of p-type amorphous silicon-carbon alloy ($\text{a-Si}_{1-x}\text{C}_x\text{:H}$) window layers in substrate/(p-i-n) solar cells. [5,7,8] In this application, the CH_n radicals ($n=1-3$) arising from the dopant source molecule are not detrimental to the growth process. In addition, BF_3 is even more stable and has been used in doping $\text{a-Si}_{1-x}\text{C}_x\text{:H}$ for p-i-n solar cells as well as in situations where C-incorporation may be undesirable, such as in doping $\mu\text{c-Si:H}$ p-layers in n-i-p solar cells. [9-11]

In this task, we have applied real time spectroscopic ellipsometry (RTSE) in a comparative study of the nucleation, coalescence, and growth processes of intended $\mu\text{c-Si:H}$ p-layers by rf PECVD using B_2H_6 , $\text{B}(\text{CH}_3)_3$, and BF_3 dopant source gases. RTSE is unique in that it can provide signatures that allow one to distinguish $\mu\text{c-Si:H}$ and a-Si:H p-layer deposition even for very thin layers in the n-i-p device configuration, i.e., for p-layers on a-Si:H i-layer substrates. [12] Insights into the deposition processes of the $\mu\text{c-Si:H}$ p-layers on a-Si:H i-layers are obtained here on the basis of the time evolution of the microstructure of the p-layer and the dielectric function ϵ of the bulk p-layer. We find that dense, single-phase $\mu\text{c-Si:H}$ p-layers can be obtained with any one of the three dopant source gases. BF_3 is unique and offers distinct advantages, however, owing to a combination of characteristics: (i) it avoids C incorporation that slows or suppresses Si crystallite growth when incorporated at sufficiently high levels [e.g., for $\text{B}(\text{CH}_3)_3$ at high plasma power and high dopant gas flow]; (ii) it has a low decomposition rate in the plasma that leads to a wider flow rate range for dense, single-phase $\mu\text{c-Si:H}$ p-layers; and (iii) as a result, it tolerates a higher plasma power flux that allows high rate $\mu\text{c-Si:H}$ p-layer growth (up to 1 Å/s) without microstructural degradation.

Experimental Procedures

Several test structures each consisting of an intended $\sim 100\text{-}200$ Å thick $\mu\text{c-Si:H}$ p-layer on top of a 3000 Å a-Si:H i-layer were fabricated on crystal Si wafers by rf PECVD. All thin film deposition and processing were performed at a substrate temperature of 200°C. The i-layers were prepared from pure SiH_4 with a gas flow of 20 stand. cm^3/min (sccm), a plasma power of 70 mW/cm^2 , and a pressure of 0.17 Torr. Prior to p-layer growth, a H_2 -plasma treatment was performed on the i-layer for 150 s using a H_2 flow of 200 sccm, a plasma power of 700 mW/cm^2 , and a pressure of 0.87 Torr. Under these conditions the bulk i-layer etch rate is 0.4 Å/s. The variable conditions and parameters for p-layer growth include the dopant source gas, which was selected from among B_2H_6 , $\text{B}(\text{CH}_3)_3$, and BF_3 . In addition, the H_2 dilution ratio $R=[\text{H}_2]/[\text{SiH}_4]$ was varied from 120 to 200, and the dopant source gas ratio $D=[X]/[\text{SiH}_4]$ was

varied from $D=0$ to 0.01 for $X=B_2H_6$, from $D=0$ to 0.05 for $X=B(CH_3)_3$, and from $D=0$ to 0.2 for $X=BF_3$. For H_2 dilution ratios from $R=120$ to 200, the H_2 gas flows were varied from 120 to 200 sccm, and the partial pressure of SiH_4 was fixed at 5 mTorr. Thus, the total pressure increased from 0.57 to 0.88 Torr with the increase in R . Two rf plasma power levels, 230 and 700 mW/cm², were also explored for the p-layers.

Electrical measurements of 250 Å p-layers prepared on i-layers under the conditions that yield dense, single-phase $\mu c-Si:H$, i.e., p-layers having optimum microstructure and optical properties for devices, suggest that successful p-type doping has been achieved. The activation energies of the conductivity for the optimized 250 Å p-layers are in the range of 0.04 to 0.17 eV, and the 25°C conductivities are in the range of $1-3 \times 10^{-3} (\Omega\text{-cm})^{-1}$.

During the i-layer treatments and p-layer depositions, RTSE was performed using a rotating polarizer multichannel ellipsometer. [13] Full spectra consisted of ~ 100 pairs of (Ψ, Δ) values from 1.5 to 4.3 eV. In monitoring the nucleation and growth of intended $\mu c-Si:H$ p-layers on the i-layer surfaces, the acquisition time for (Ψ, Δ) spectra was 1 s and the repetition time was 8 s. The (Ψ, Δ) spectra were analyzed using three and four layer models as described in detail elsewhere. [12] Insights into the deposition processes for the p-layers are obtained by assessing differences in the time evolution of the surface roughness and bulk layer thicknesses, d_s and d_b , respectively, as well as differences in the bulk layer dielectric functions.

Results and Discussion:

Effect of H_2 -Dilution on the Nucleation and Growth of $\mu c-Si:H$ p-Layers

We have explored the effect of H_2 -dilution level R on the microstructural evolution and optical properties of $\mu c-Si:H$ p-layers prepared on H_2 -plasma treated i-layers using $B(CH_3)_3$ and B_2H_6 doping gases. Because the results are similar for both gases, we focus here on p-layers prepared using $B(CH_3)_3$. Figures III.2.1 and 2 provide comparisons of the microstructural evolution and dielectric functions of $\mu c-Si:H$ p-layers prepared with $R=120$, 160, and 200. For all three p-layer depositions, the $B(CH_3)_3$ doping gas flow ratio is $D=0.01$ and the plasma power

is 230 mW/cm². The results in Fig. III.2.2 show that the three p-layers prepared over the range from R=120 to 200 are all microcrystalline. For the two films of lower R, however, a-Si:H fractions appear to be present in the films as indicated by the larger ϵ_2 values at lower energies. In addition, the peak heights in ϵ are reduced for the films of lower R, revealing that the development of the amorphous phase is also accompanied by a larger void fraction in the p-layers. From the overall results in Fig. III.2.2, we conclude that the highest H₂-dilution ratio of R=200 is most effective in generating high density, single-phase $\mu\text{c-Si:H}$ p-layers.

As shown in Fig. III.2.1, the general features of the evolution of d_b and d_s for all three films are similar and provide evidence for the propagation of p-layer crystallites from nuclei generated in the initial H₂-plasma treatment. There are two clear effects of the H₂-dilution level on the microstructural evolution. First, the stabilized bulk layer deposition rate decreases from 0.43 to 0.29 Å/s as R is increased from 120 to 200. Second, the deposition rate during the initial growth of the bulk layer also decreases from 0.15 to 0.10 Å/s with increasing R, indicating an “induction period” that becomes more pronounced at larger R. It is likely that a pronounced induction period results when growth and etching processes are near equilibrium in the initial growth of $\mu\text{c-Si:H}$. [14] Under these conditions the amorphous component that would otherwise develop when crystalline nuclei coalesce is suppressed by etching reactions. As the equilibrium is shifted to favor growth over etching (i.e., as R is decreased), the induction behavior is weakened and an amorphous phase develops during coalescence that propagates throughout the growth of the bulk film. Further evidence for this interpretation is presented in the next two parts, as well.

Results and Discussion:

Effect of Doping Level on the Nucleation and Growth of $\mu\text{c-Si:H}$ p-Layers

Next, we compare the effects of doping level on the microstructural evolution for p-layers prepared on H₂-plasma treated i-layers using B(CH₃)₃, BF₃, and B₂H₆ doping gases. We have avoided using B₂H₆ at levels higher than D=0.01 in this study due to the ease with which B₂H₆

is dissociated in the plasma, as well as the enhanced spontaneous CVD and contamination that occurs at high doping levels. [2] Figures III.2.3 and 4 show the microstructural evolution and dielectric functions for three films prepared using $B(CH_3)_3$ as the dopant source gas with $D=0$, 0.01, and 0.05. Figures III.2.5 and 6 show the corresponding results for three films prepared using BF_3 as the dopant source gas with $D=0$, 0.015, and 0.10. For all five depositions, the H_2 -dilution ratio is $R=200$ and the plasma power is 230 mW/cm^2 .

For the control film of Figs. III.2.3-6 which is prepared at $R=200$ and 230 mW/cm^2 without doping ($D=0$), there is a very long initial induction period lasting $\sim 700 \text{ s}$ ($100 < t < 800 \text{ s}$). This represents a period during which roughness develops on the p-layer surface, but bulk layer growth is extremely slow, $\sim 0.03 \text{ \AA/s}$. Such behavior is expected if growth and etching are near equilibrium and proceed simultaneously over different regions of the i-layer surface. This leads to a low nucleation density, a large spacing between nuclei, a broader distribution of nuclei sizes, and thus, weaker coalescence. In fact, because of the strong etching environment, the initial H_2 -plasma treatment in this case does not have a significant effect on the nucleation of the undoped material. This unique growth behavior for the undoped film is also evident from the dielectric function of the "bulk layer", shown as the control sample ($D=0$) in both Figs. III.2.4 and 6. This dielectric function exhibits very low peak amplitudes, indicating a high void volume fraction attributable to an incompletely coalesced film. In addition, a stronger low energy tail appears in ϵ_2 . The tail is attributable in this case, not to an amorphous component, but rather to large defective Si crystallites with strongly broadened, but bulk-like, electronic transitions. Next, we will describe how the additions of $B(CH_3)_3$, BF_3 , and B_2H_6 alter the growth characteristics and optical properties.

Figure III.2.3 shows that the addition of $B(CH_3)_3$ at the level of $D=0.01$, leads to a significant decrease in the induction period (from $\sim 700 \text{ s}$ to $\sim 250 \text{ s}$), and an enhancement in the bulk layer growth rate (from 0.19 \AA/s to 0.29 \AA/s). Thus, with the addition of $B(CH_3)_3$ at $D=0.01$, coalescence occurs to form a high density single-phase $\mu\text{c-Si:H}$ p-layer as shown by the dielectric function in Fig. III.2.4 (solid line). In addition, Fig. III.2.3 shows that the addition of

$\text{B}(\text{CH}_3)_3$ at the level of $D=0.05$, leads to a complete elimination of the induction period and a virtually time independent surface roughness layer thickness of $d_s=19 \text{ \AA}$. This latter behavior is characteristic of amorphous film growth, and the shape of the dielectric function in Fig. III.2.4 (dotted line) corroborates this conclusion. This example demonstrates the ability of RTSE to identify the dramatic effects of doping on the microstructural evolution of the p-layers.

In contrast to these results for $\text{B}(\text{CH}_3)_3$, Figs. III.2.5 and 6 show that the addition of BF_3 at the level of $D=0.015$ has comparatively little effect on the induction period, microstructural evolution, film homogeneity, and optical properties after 120 \AA . One difference that can be noted in Fig. III.2.5 is the stabilization of the roughness layer thickness at somewhat smaller values for the doped film ($\sim 40 \text{ \AA}$ versus $\sim 55 \text{ \AA}$ for the undoped film). This suggests a weak increase in the nucleation density and, thus, a reduction in crystallite size and improvement in the coalescence behavior with the addition of BF_3 at $D=0.015$. This effect also appears in the optical properties of Fig. III.2.6, but is much weaker in comparison to the corresponding effect for $\text{B}(\text{CH}_3)_3$ doping gas. In order to generate an improvement in homogeneity comparable to that obtained by a $\text{B}(\text{CH}_3)_3$ addition at $D=0.01$, more than a factor of ten higher flow rate of BF_3 must be added to the gas phase. This should be clear from the results in Figs. III.2.5(c) and 6. The addition of BF_3 at $D=0.10$ leads to a decrease in the induction period (from 700 to 300 s), and an enhancement in the bulk layer growth rate (from 0.19 \AA/s to 0.31 \AA/s), similar to the results obtained using $\text{B}(\text{CH}_3)_3$ at $D=0.01$. Finally, we have found that additions of B_2H_6 at the level of $D=0.01$, completely eliminate the induction period (not shown). This suggests a much higher sensitivity of the deposition process and film microstructural evolution to doping using B_2H_6 in comparison with $\text{B}(\text{CH}_3)_3$. In contrast to the results in Fig. III.2.3(c) for $\text{B}(\text{CH}_3)_3$ at the level of $D=0.05$, in which the induction period is eliminated and an amorphous structure is obtained, the results for B_2H_6 at $D=0.01$ yield a completely-coalesced microcrystalline p-layer.

The general observations of this section, in which we have found that the use of $\text{B}(\text{CH}_3)_3$ at $D=0.01$ or BF_3 at $D=0.10$ *enhances* the structural homogeneity and density of the $\mu\text{-Si:H}$ p-layers when prepared on a H_2 -plasma *treated* i-layers, appear to be in contradiction with our

previous results [15], in which the incorporation of these dopant gases in the plasma *suppresses* the onset of $\mu\text{c-Si:H}$ p-layer nucleation on *untreated* i-layers. However, both sets of observations can be interpreted consistently to suggest that the use of the doping gases shifts the growth-etching equilibrium toward the growth direction. For the untreated i-layer, this shift leads to an enhancement in the propagation of the amorphous network that exists at the i-layer surface, whereas for the H_2 -plasma treated i-layer, the shift leads to an enhancement in the growth of the crystalline phase from the crystalline nuclei that exist at the i-layer surface. Thus, a reduction in etching processes for the untreated i-layer surface is detrimental because it prevents microcrystalline p-layer nuclei formation on the i-layer and allows the amorphous network to propagate. A reduction in the etching processes is desirable for the treated i-layer since in this case etching removes existing nucleation sites and reduces the nucleation density; [see, e.g., Figs. III.2.5(a) and (b)].

The observations of Figs. III.2.3-6 suggest that B-containing radicals such as BCH_3 , BF_2 , or BH_3 incorporated at the surface of the substrate i-layer in the initial stages of p-layer growth act as catalysts to shift the growth-etching equilibrium toward the growth direction. [16] In fact, the increase in the apparent activity of B from $\text{BF}_3 \rightarrow \text{B}(\text{CH}_3)_3 \rightarrow \text{B}_2\text{H}_6$, observed as a decrease in the prominence of the induction behavior for this sequence, matches the trend in bond energies $E(\text{B-F}) > E(\text{B-C}) > E(\text{B-B})$. [17] As a result of this trend, BF_3 is the most difficult to dissociate in the plasma, whereas B_2H_6 is the easiest (and even spontaneously decomposes in the absence of the plasma). Thus, for a given set of gas phase conditions, the B-containing radical concentration near the i/p interface in the initial stages of p-layer growth is expected to increase in the order $\text{BF}_3 \rightarrow \text{B}(\text{CH}_3)_3 \rightarrow \text{B}_2\text{H}_6$. One might expect that the additional increase in the doping level with $\text{B}(\text{CH}_3)_3$ from $D=0.01$ to 0.05 would lead to a further improvement in p-layer homogeneity. However, the increase in Si-BCH_3 units in the p-layer may shift the growth-etching equilibrium even further to the growth direction, to the point where the propagation of the crystalline network across the i/p interface is hindered and the amorphous phase develops. In the case of BF_3 at $D=0.10$ and B_2H_6 at $D=0.01$ insufficient doping gas

molecules are dissociated to enter the amorphous growth regime. In fact, for p-type doping using these gases, it is possible that a higher concentration of incorporated B is needed to enter the amorphous regime since any Si-BH_n or Si-BF_n structures trapped in the film would have a less perturbing influence on the network than Si-BCH_n structures.

Results and Discussion:

Effect of Plasma Power on the Nucleation and Growth of μ c-Si:H p-Layers

Lastly, we describe the effects of plasma power on the nucleation and growth of intended μ c-Si:H p-layers atop H₂-plasma treated i-layers. In this section, we focus on undoped layers and p-layers prepared using B(CH₃)₃ and BF₃ dopant source gases. Because B₂H₆ is so easily dissociated in the plasma, we avoid studies of p-layers prepared at high plasma power using B₂H₆ in order to avoid excessive contamination of the PECVD reactor. Figures III.2.7 and 8 show the microstructural evolution and dielectric functions for two films prepared without doping (D=0) using plasma powers of 230 and 700 mW/cm². Figures III.2.9 and 10 show the corresponding results using B(CH₃)₃ for doping at D=0.01, and Figs. III.2.11 and 12 show the results using BF₃ at D=0.015. For all six depositions of Figs. III.2.7-12, the H₂-dilution ratio is R=200.

Figure III.2.7 shows the significant effect of plasma power on the microstructural evolution for undoped μ c-Si:H growth. First, with the increase in plasma power, the induction period decreases from 700 to 75 s and the bulk layer growth rate increases from 0.19 to 0.67 Å/s. In addition, the roughness layer stabilizes at ~40 Å after 200 s at the higher power setting, lower than the value of ~55 Å obtained after 1000 s at the lower power. The appearances of the induction period and the surface roughening effect suggest that a μ c-Si:H film is obtained in the deposition at higher power. This is corroborated by the dielectric function in Fig. III.2.8, which shows that a significant densification of the microcrystalline structure occurs when the plasma power is increased. Similar trends are observed for the microstructural evolution of the p-layers in Figs. III.2.9 and 11. In fact for p-layers doped using a low level of BF₃ gas (D=0.015), the

effect of power on the growth pattern is similar to that for undoped layers as can be seen by comparing Figs. III.2.7 and 11. The primary difference is the higher deposition rate (0.93 vs. 0.67 Å/s) obtained by adding the dopant gas at the higher power. For p-layers doped using a low level of $\text{B}(\text{CH}_3)_3$, the presence of the doping gas has already significantly reduced the induction period and enhanced the bulk layer growth rate as described in the previous section. However, Fig. III.2.9 shows that increasing the plasma power to 700 mW/cm² completely eliminates the induction period, while retaining a microcrystalline film structure as indicated by the roughening in Fig. III.2.9(b) and by the dielectric function in Fig. III.2.10 (dashed lines). A comparison of the dielectric functions in Fig. III.2.10 for low and high power depositions with $\text{B}(\text{CH}_3)_3$ shows that the complete suppression of the induction period is accompanied by an increase in the amorphous and void components in the layer.

At the higher plasma power, the results in Figs. III.2.7-12 suggest that the nucleation process is no longer controlled by the catalytic effects of B-containing radical incorporation in the i/p interface region. Instead, we propose that nucleation is controlled by the bombardment effects of Si-containing ions. Thus, with increasing plasma power the nucleation density is increased, and enhanced coalescence occurs that generates relatively dense films even without doping (or even at low gas phase levels of doping using BF_3). In fact, a comparison of the results in this section and those in the previous subsection demonstrate that the effects of an increase in plasma power are similar to the effects of doping gas additions to the plasma. The similarity can be seen most clearly by considering Figs. III.2.3(a) and (b) for additions of $\text{B}(\text{CH}_3)_3$ at $D=0.01$ in comparison with Figs. III.2.7(a) and (b) for an increase in power from 230 to 700 mW/cm². Thus, we conclude that the role of the plasma power increase is also to shift the growth-etching equilibrium toward the growth direction. In the case of $\text{B}(\text{CH}_3)_3$ at $D=0.01$, the combined effects of the increased plasma power and doping are to reduce etching processes to the point where no induction period is evident and an amorphous phase develops between coalescing crystallites. In contrast, for BF_3 over the range from $D=0.015$ to $D=0.1$, these

combined effects do not appear to be as detrimental as for $\text{B}(\text{CH}_3)_3$; (compare Figs. III.2.10 and 12).

Figure III.2.13 provides a comparison of the microstructural evolution of films prepared using BF_3 at different gas phase doping levels from $D=0$ to 0.1 for the higher plasma power level of 700 mW/cm^2 . Although the induction period is suppressed (from 75 to 40 s) and the bulk layer growth rate during this period increases with increasing doping level (from 0.20 to 0.47 \AA/s), a well defined induction period remains even for D as high as 0.10. Thus, in contrast to the $\text{B}(\text{CH}_3)_3$ dopant source gas, relatively strong etching processes remain for the BF_3 source gas, and this prevents the development of an amorphous component in the film. Figure III.2.14 shows the dielectric functions for an even wider range of doping levels for p-layers prepared using BF_3 at the higher power. Although there is a weak optimum in the crystalline quality and bulk layer density near $D=0.05$, overall the effect of doping gas level is nearly undetectable at the higher power. Thus, dense, single-phase $\mu\text{c-Si:H}$ p-layers are obtained for a wide range of gas phase doping levels using BF_3 .

For the BF_3 doping source gas, we suggest that at the higher plasma power levels, although more B-containing radicals are generated, a more reactive environment exists that can etch the film and also remove F atoms from BF_n units bonded to Si at the film surface. A comparison of Figs. III.2.7(b) and 9(b) shows that the addition of $\text{B}(\text{CH}_3)_3$ at $D=0.01$ reduces the bulk layer deposition rate in comparison to $D=0$ by 40%. In contrast, a comparison of Figs. III.2.7(b) and 11(b) shows that the addition of BF_3 at $D=0.015$ enhances the bulk layer deposition rate by $\sim 40\%$. We attribute this difference to the differing roles of CH_3 and F radicals in affecting the propagation of the crystalline Si network. We expect that CH_n incorporation at the crystallite surface slows the ability of atomic H to promote crystallite propagation. In contrast, F is effective at removing H from the surface of the growing crystallites, thus allowing sites for SiH_3 attachment and more rapid propagation of the crystalline network.

Concluding Remarks

Real time spectroscopic ellipsometry (RTSE) has been used to investigate the nucleation, coalescence, and growth of intended microcrystalline silicon ($\mu\text{c-Si:H}$) p-layers by plasma-enhanced chemical vapor deposition (PECVD) on amorphous silicon (a-Si:H) i-layers for applications in devices in the substrate/(n-i-p) configuration. The microstructural evolution and optical properties of the p-layers have been determined as a function of the preparation procedure and variables. We have studied the effects of (i) the dopant source gas from among B_2H_6 , $\text{B}(\text{CH}_3)_3$, and BF_3 , (ii) hydrogen dilution flow ratio $R=[\text{H}_2]/[\text{SiH}_4]$, (iii) dopant gas flow ratio $D=[\text{X}]/[\text{SiH}_4]$ where X is B_2H_6 , $\text{B}(\text{CH}_3)_3$, or BF_3 , and (iv) rf plasma power. The goal of these studies is to understand the effect of these parameters on the microstructure of the p-layer and to identify PECVD strategies that yield single-phase $\mu\text{c-Si:H}$ p-layers of high density on a-Si:H i-layer surfaces even after $\sim 100 \text{ \AA}$.

For undoped film growth at low power and a high H_2 -dilution level of $R=200$ on H_2 -plasma treated substrates, $\mu\text{c-Si:H}$ nucleates but the growth and etching processes are nearly in balance. This leads to a very long induction period, a low nucleation density, and thus an incompletely coalesced film after 120 \AA . This behavior suggests that the crystalline nuclei at the surface of the i-layer generated by the initial H_2 -plasma treatment are removed in the strong etching environment. We find that additions of any one of the three doping gases or an increase in plasma power, or a combination of the two effects shift this growth-etching balance in favor of growth. As a result under these conditions, $\mu\text{c-Si:H}$ layers nucleate at high density, and coalesce to form a continuous film well before 120 \AA without a long induction period. Thus, the incorporated dopant species act as catalysts that hinder etching and allow the existing network at the i-layer surface to propagate, irrespective of its phase (i.e., amorphous or crystalline). As long as the growth-etching balance is not shifted too far in the growth direction, nuclei coalesce to form a single-phase $\mu\text{c-Si:H}$ without any a-Si:H at the grain boundaries. This accounts for the novel optical properties of the

bulk $\mu\text{c-Si:H}$ layer, namely the abrupt absorption onset near 2.5 eV attributed earlier to quantum confinement in 30 Å crystallites. [12]

In summary, Fig. III.2.15 shows the dielectric functions for 120 Å single-phase microcrystalline p-layers obtained using B_2H_6 , $\text{B}(\text{CH}_3)_3$, and BF_3 under conditions optimized to yield dense, single-phase $\mu\text{c-Si:H}$. The ability to obtain results for $\text{B}(\text{CH}_3)_3$, and BF_3 comparable to those for B_2H_6 provides alternative approaches for p-layers that avoid the undesirable contamination effects associated with B_2H_6 gas. However, we have found here that p-layer deposition using $\text{B}(\text{CH}_3)_3$, and BF_3 require distinctly different strategies. For BF_3 , p-layers are optimized at high plasma power, and under these conditions, the gas phase doping level has little effect on the microstructure and optical properties over a wide range from $D=0.01$ to 0.20. For $\text{B}(\text{CH}_3)_3$, however, p-layers are optimized at lower power, and the doping level has a strong effect on the microstructure. In this case, a well-defined optimum is observed at low doping level below which voids develop and above which an amorphous component develops. The difference is attributed to the differing roles of F versus CH_3 radicals generated in the plasma upon dissociation of the dopant gas. We conclude that doping using BF_3 can provide advantages for the preparation and optimization of $\mu\text{c-Si:H}$ p-layers in n-i-p devices such as solar cells, not only due to the much broader range in parameter space over which dense, single-phase $\mu\text{c-Si:H}$ can be deposited, but also due to the higher attainable rates.

References

1. S. Guha, J. Yang, P. Nath, and M. Hack, Appl. Phys. Lett. **49**, 218 (1986).
2. R.W. Collins, Appl. Phys. Lett. **53**, 1086 (1988).
3. P. Roca i Cabarrocas, S. Kumar, and B. Drevillon, J. Appl. Phys. **66**, 3286 (1989).
4. J. Koh, Y. Lu, S. Kim, J.S. Burnham, C.R. Wronski, and R.W. Collins, Appl. Phys. Lett. **67**, 2669 (1995).

5. H. Tarui, T. Matsuyama, S. Okamoto, H. Dohjoh, Y. Hishikawa, N. Nakamura, S. Tsuda, S. Nakano, M. Ohnishi, and Y. Kuwano, *Jpn. J. Appl. Phys.* **28**, 2436 (1989).
6. R. Fluckiger, J. Meier, A. Shah, A. Catana, M. Brunel, H.V. Nguyen, R.W. Collins, and R. Carius, *Mater. Res. Soc. Symp. Proc.* **336**, 511 (1994).
7. Y.-M. Li, F. Jackson, L. Yang, B.F. Fieselmann, and L. Russell, *Mater. Res. Soc. Symp. Proc.* **336**, 663 (1994).
8. A. Lloret, Z.Y. Wu, M.L. Theye, I. El Zawawi, J.M. Siefert, and B. Equer, *Appl. Phys. A* **55**, 573 (1992).
9. A. Asano and H. Sakai, *Appl. Phys. Lett.* **54**, 904 (1989).
10. H. Kakinuma, M. Mohri, and T. Tsuruoka, *J. Appl. Phys.* **74**, 4614 (1993).
11. J.J. Gandia, M.T. Gutierrez, and J. Carabe, *Thin Solid Films* **223**, 161 (1993).
12. J. Koh, H. Fujiwara, C.R. Wronski, and R.W. Collins, *Sol. Energy Mater. Sol. Cells* **49**, 135 (1997).
13. R.W. Collins, *Rev. Sci. Instrum.* **61**, 2029 (1990).
14. C.C. Tsai, "Amorphous Silicon and Related Materials", Vol. A, edited by H. Fritzsche, (World Scientific, Singapore, 1989) p. 123.
15. Joohyun Koh, H. Fujiwara, R.J. Koval, C.R. Wronski, and R.W. Collins, *J. Appl. Phys.* **85**, 4141 (1999).
16. J. Perrin, Y. Takeda, N. Hirano, Y. Takeuchi, and A. Matsuda, *Surf. Sci.* **210**, 114 (1989).
17. T.L. Cottrell, "The Strength of Chemical Bonds, 2nd Ed.", (Butterworths, London, 1958).

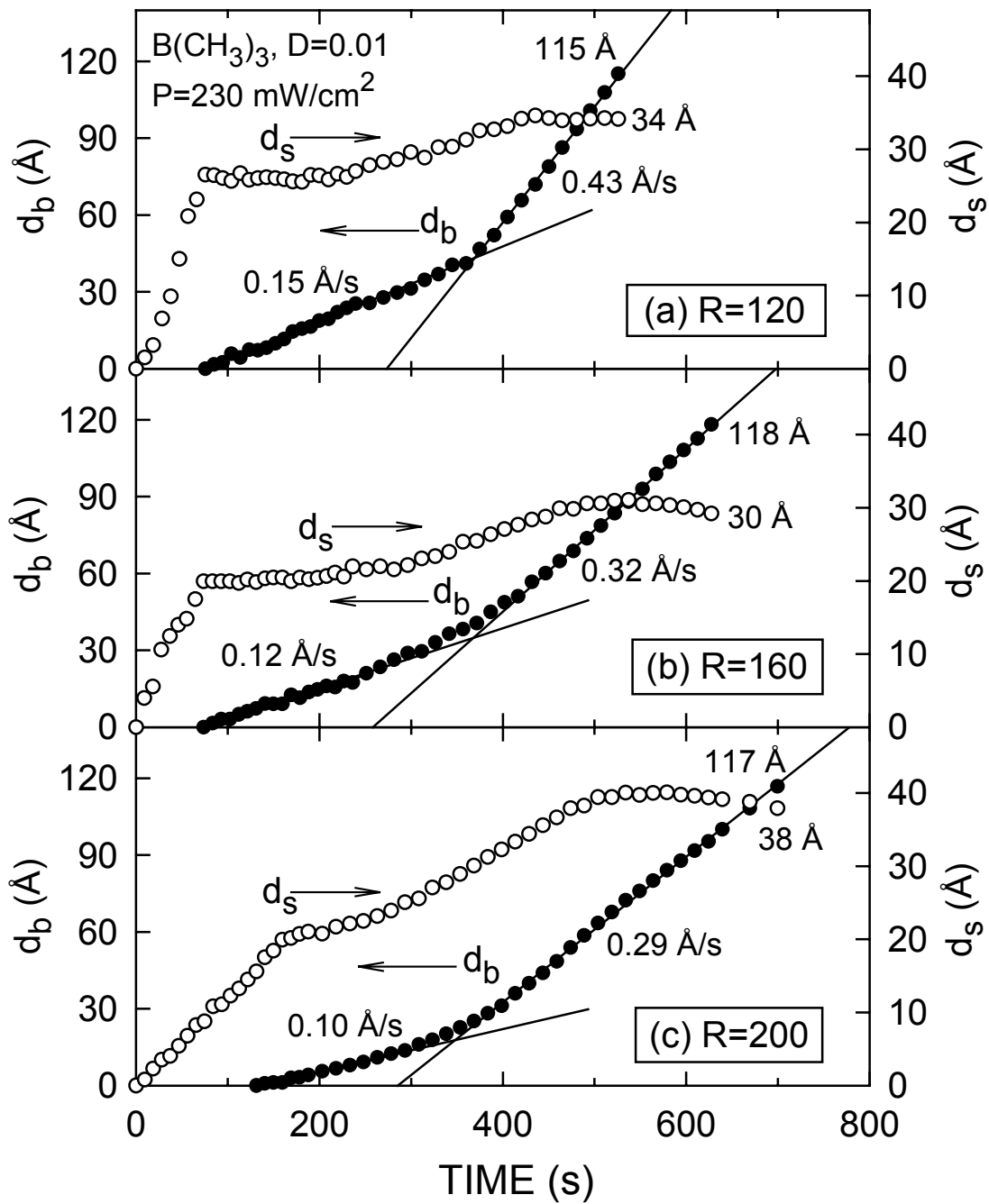


Figure III.2.1 Evolution of the surface roughness layer thickness d_s (open points) and bulk layer thickness d_b (closed points) for 115-120 Å (bulk) p-layers prepared on H_2 -plasma treated i-layers using $B(CH_3)_3$ doping gas with $D=0.01$, a plasma power of 230 mW/cm^2 , and H_2 dilution ratios of (a) $R=120$; (b) $R=160$; and (c) $R=200$.

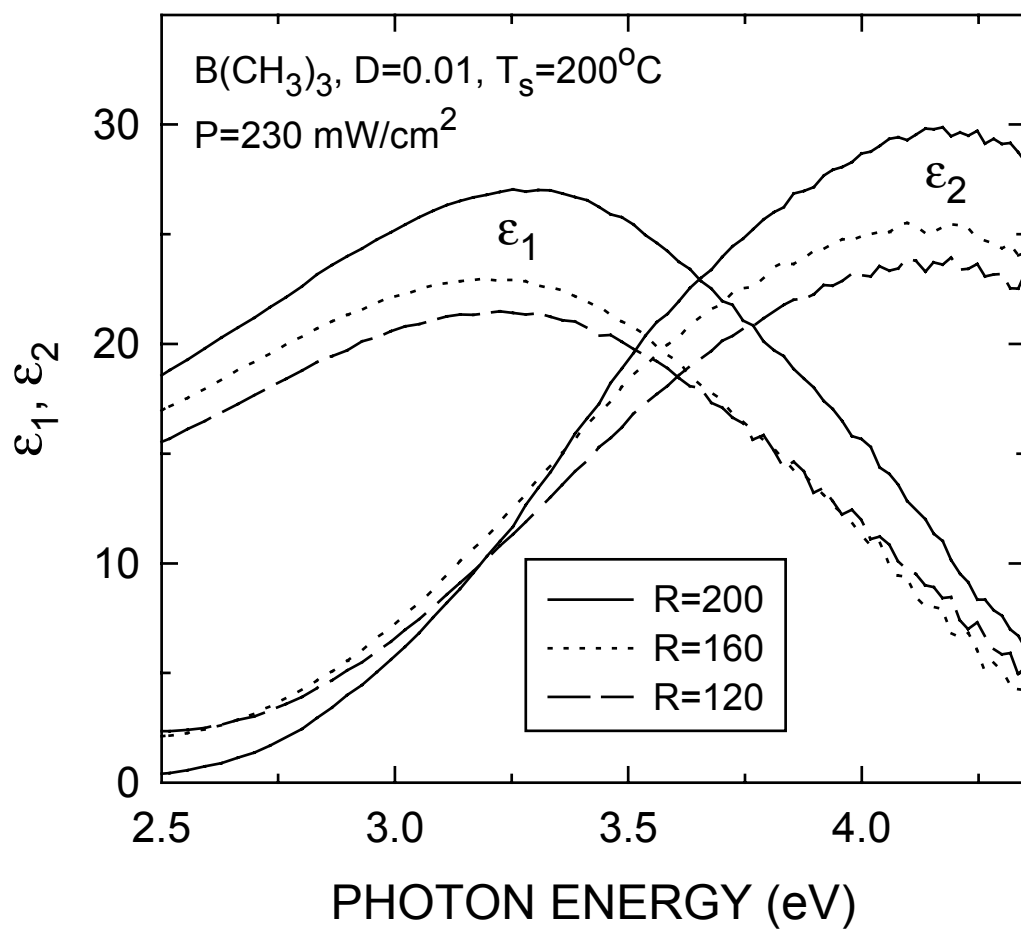


Figure III.2.2 Dielectric functions for 115-120 Å (bulk) p-layers prepared on H_2 -plasma treated i-layers using $B(CH_3)_3$ doping gas with $D=0.01$, a plasma power of 230 mW/cm^2 , and H_2 dilution ratios of $R=120$ (dashed line); (b) $R=160$ (dotted line); and (c) $R=200$ (solid line).

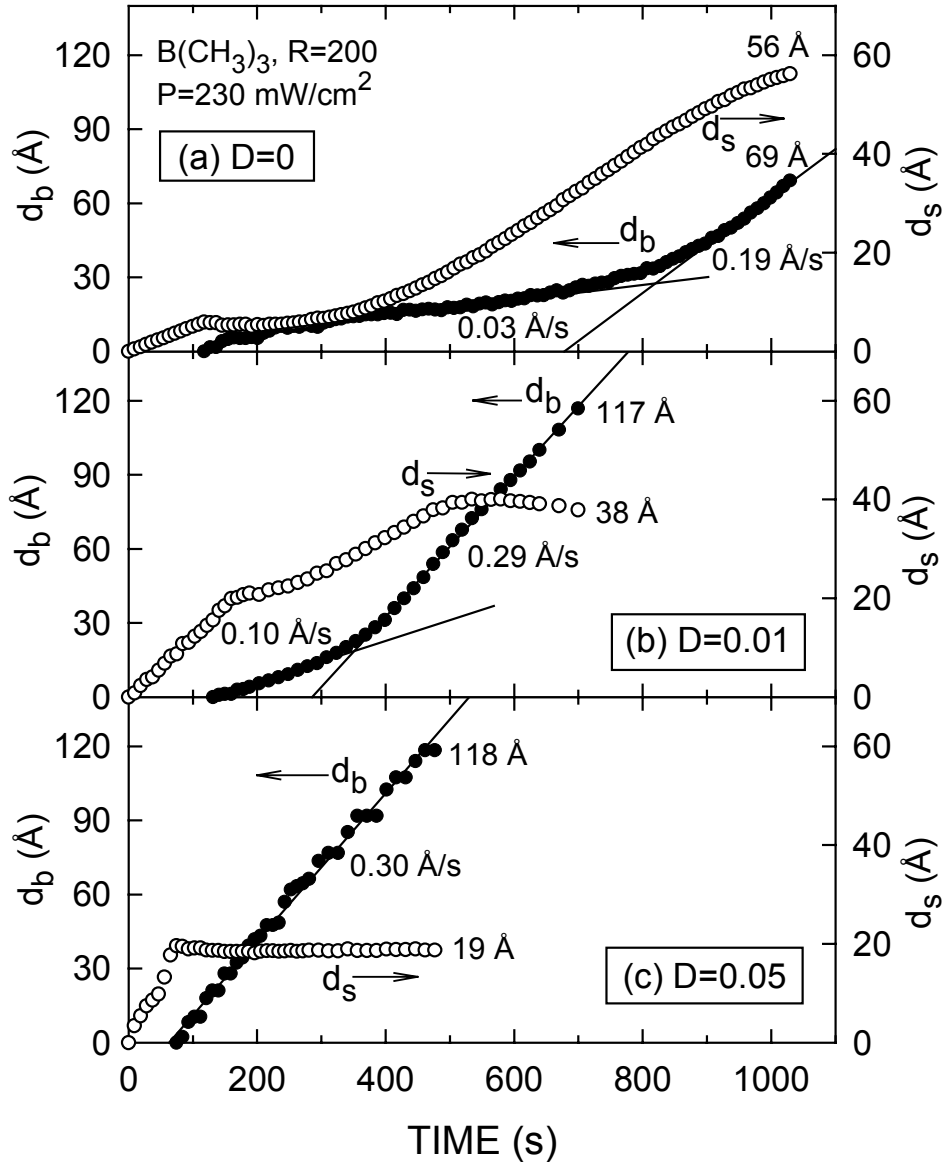


Figure III.2.3 Evolution of the surface roughness layer thickness d_s (open points) and bulk layer thickness d_b (closed points) for 70-120 Å (bulk) p-layers prepared on H_2 -plasma treated i-layers using a H_2 dilution ratio of $R=200$, and a plasma power of 230 mW/cm^2 . Different $B(CH_3)_3$ doping gas flow ratios of (a) $D=0$, (b) $D=0.01$, and (c) $D=0.05$ were employed.

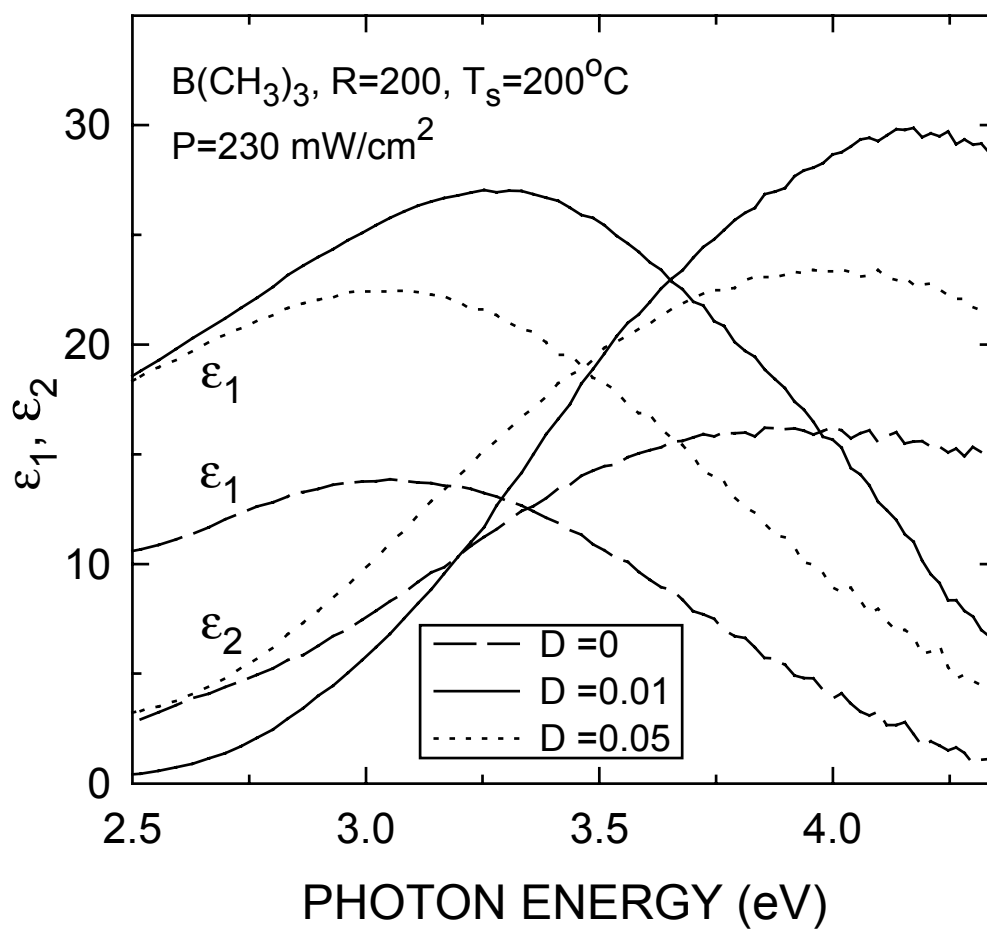


Figure III.2.4 Dielectric functions for 70-120 Å (bulk) p-layers prepared on H₂-plasma treated i-layers using a H₂ dilution ratio of R=200, and a plasma power of 230 mW/cm². Different B(CH₃)₃ doping gas flow ratios of D=0 (dashed line), (b) D=0.01 (solid line), and (c) D=0.05 (dotted line) were employed.

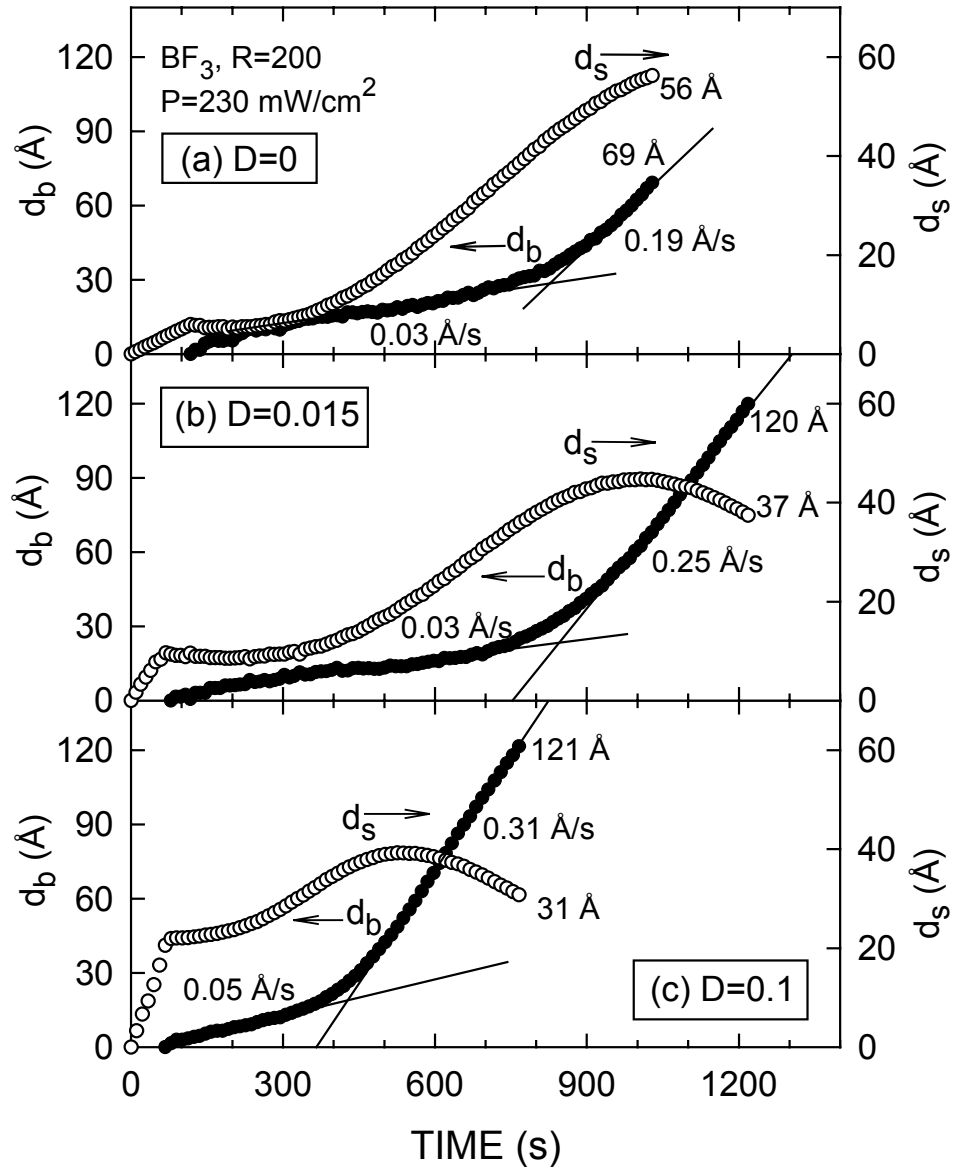


Figure III.2.5 Evolution of the surface roughness layer thickness d_s (open points) and bulk layer thickness d_b (closed points) for 70-120 Å (bulk) p-layers prepared on H₂-plasma treated i-layers using a H₂ dilution ratio of R=200, and a plasma power of 230 mW/cm². Different BF₃ doping gas flow ratios of (a) D=0, (b) D=0.015, and (c) D=0.10 were employed.

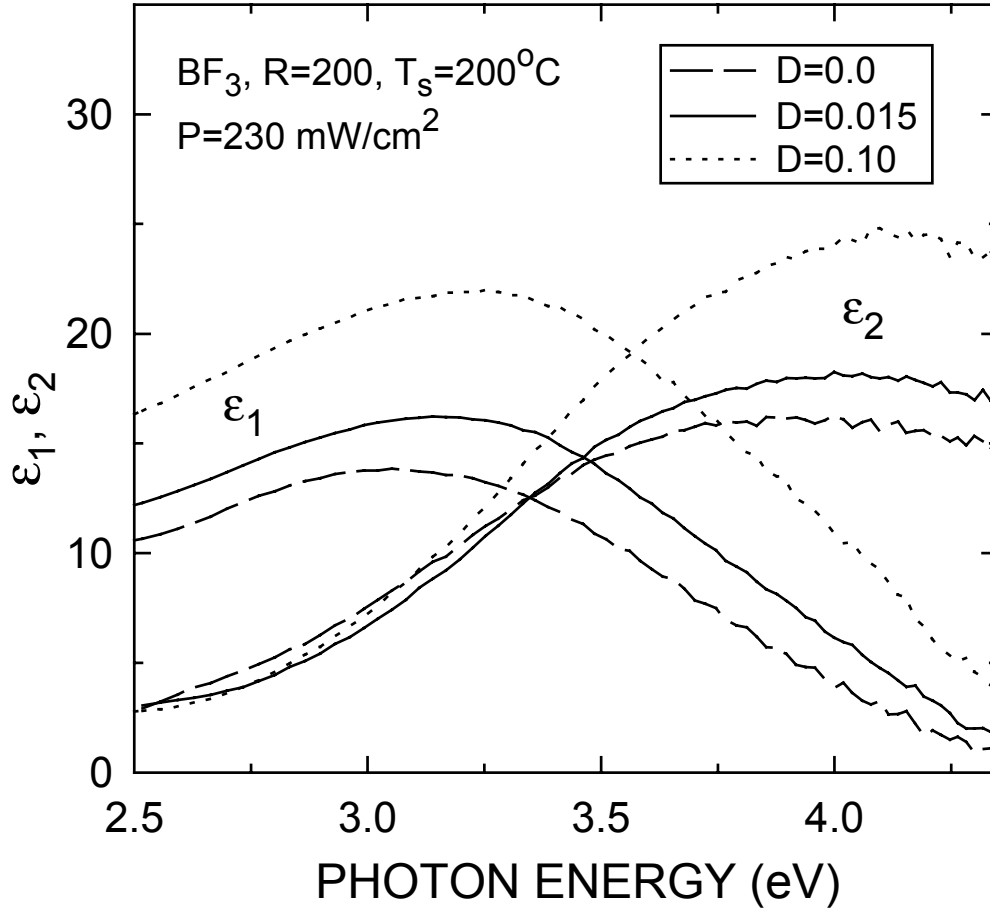


Figure III.2.6 Dielectric functions for 70-120 Å (bulk) p-layers prepared on H₂-plasma treated i-layers using a H₂ dilution ratio of R=200, and a plasma power of 230 mW/cm². Different BF₃ doping gas flow ratios of D=0 (dashed line), D=0.015 (solid line), and D=0.10 (dotted line) were employed.

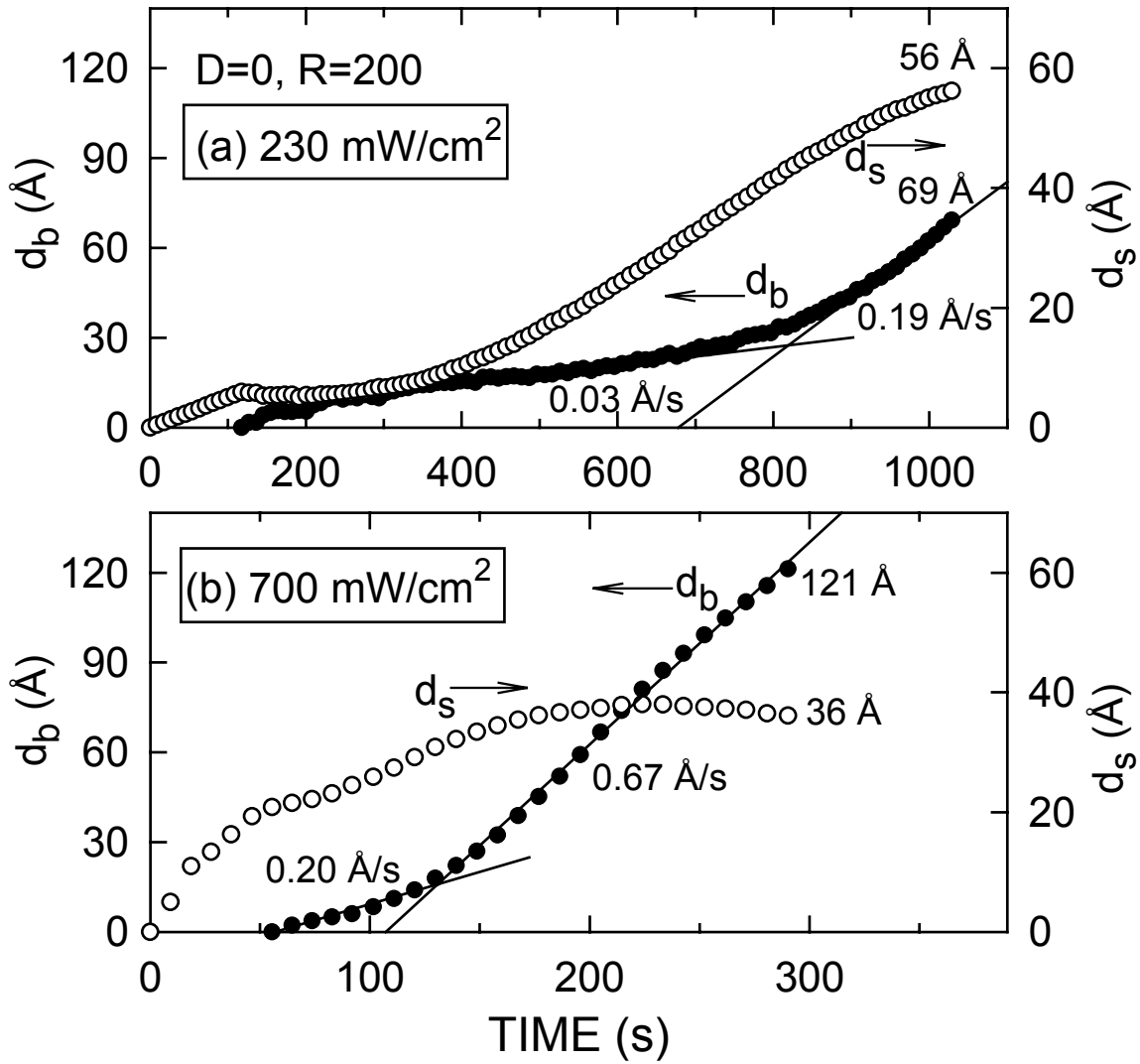


Figure III.2.7 Evolution of the surface roughness layer thickness d_s (open points) and bulk layer thickness d_b (closed points) for 70-120 Å (bulk) undoped $\mu\text{-Si:H}$ films prepared on H_2 -plasma treated i-layers using a H_2 dilution ratio of $R=200$, and plasma powers of (a) 230 mW/cm^2 and (b) 700 mW/cm^2 .

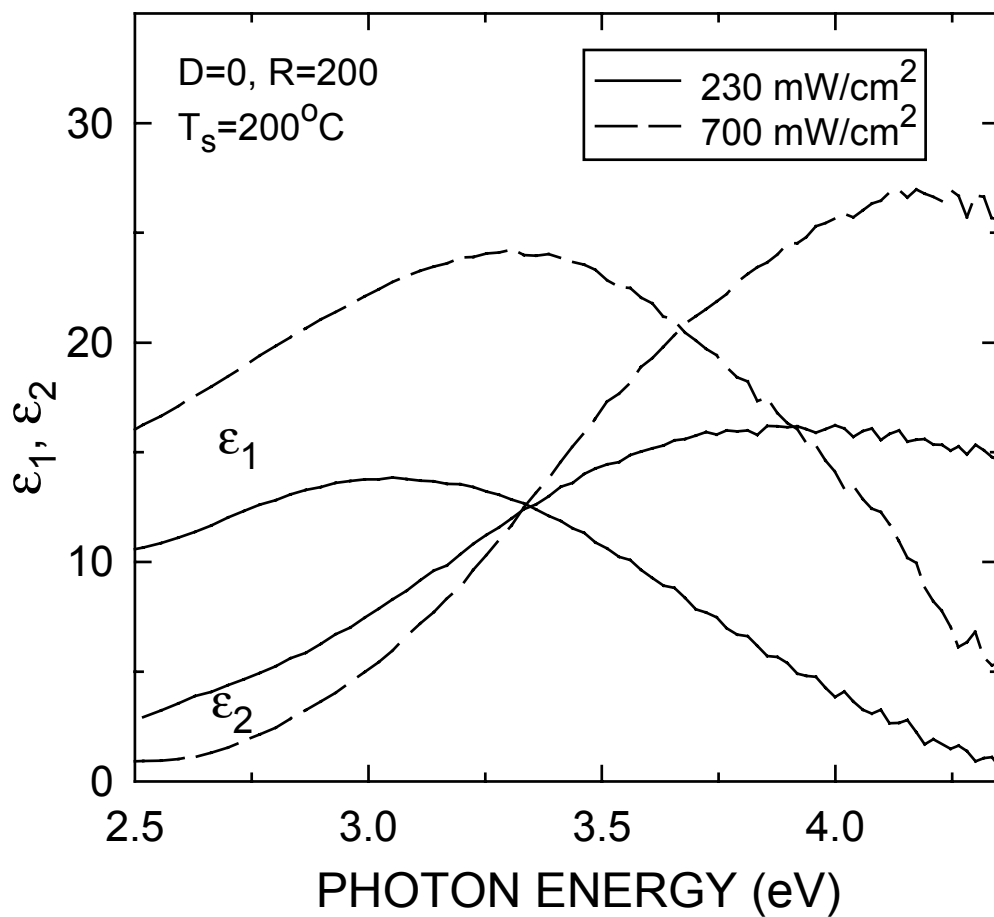


Figure III.2.8 Dielectric functions for 70-120 Å (bulk) undoped $\mu\text{c-Si:H}$ films prepared on H_2 -plasma treated i-layers using a H_2 dilution ratio of $R=200$, and plasma powers of 230 mW/cm² (solid line) and 700 mW/cm² (dashed line).

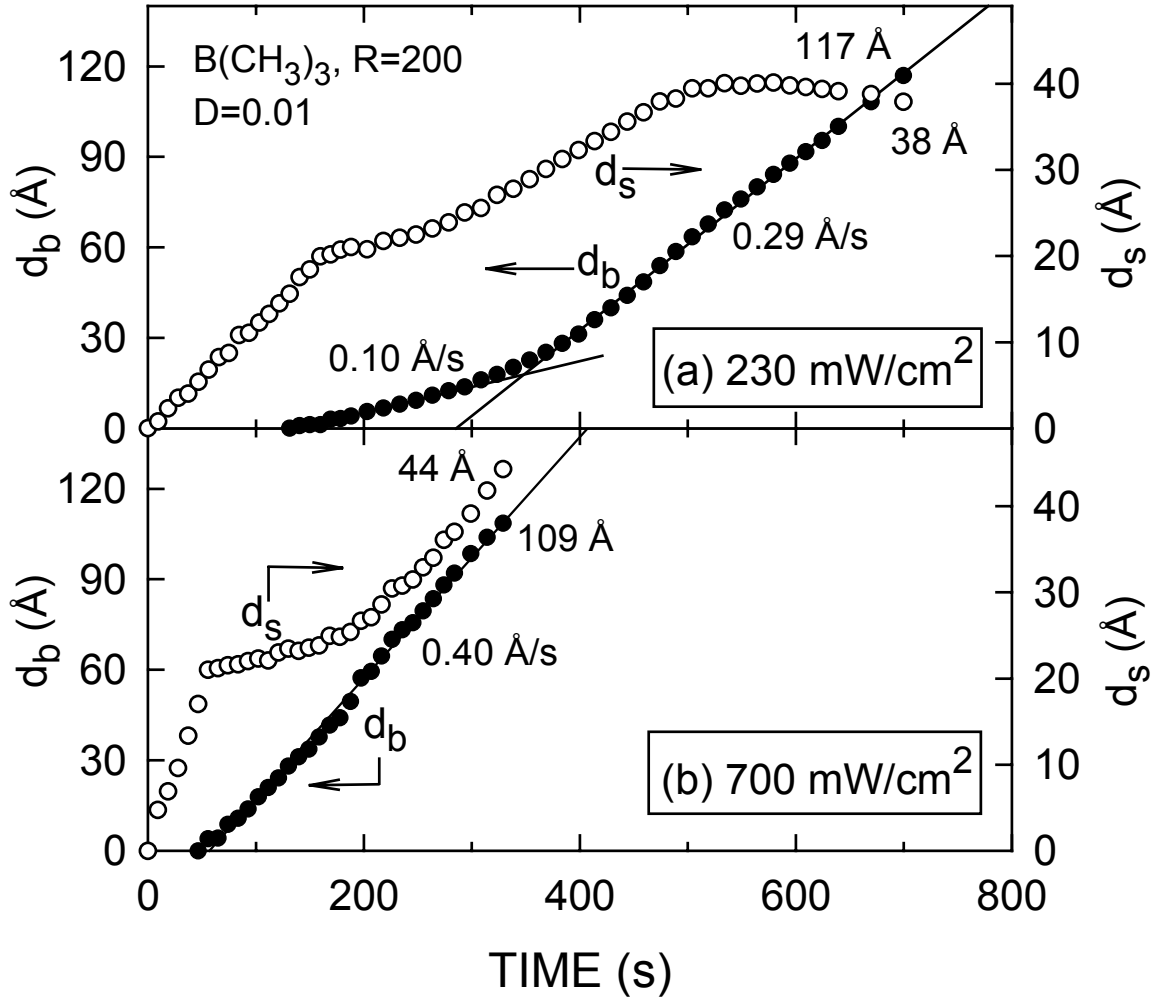


Figure III.2.9 Evolution of the surface roughness layer thickness d_s (open points) and bulk layer thickness d_b (closed points) for 110-120 Å (bulk) p-layers prepared on H₂-plasma treated i-layers using B(CH₃)₃ doping gas with $D=0.01$, a H₂ dilution ratio of $R=200$, and plasma powers of (a) 230 mW/cm² and (b) 700 mW/cm².

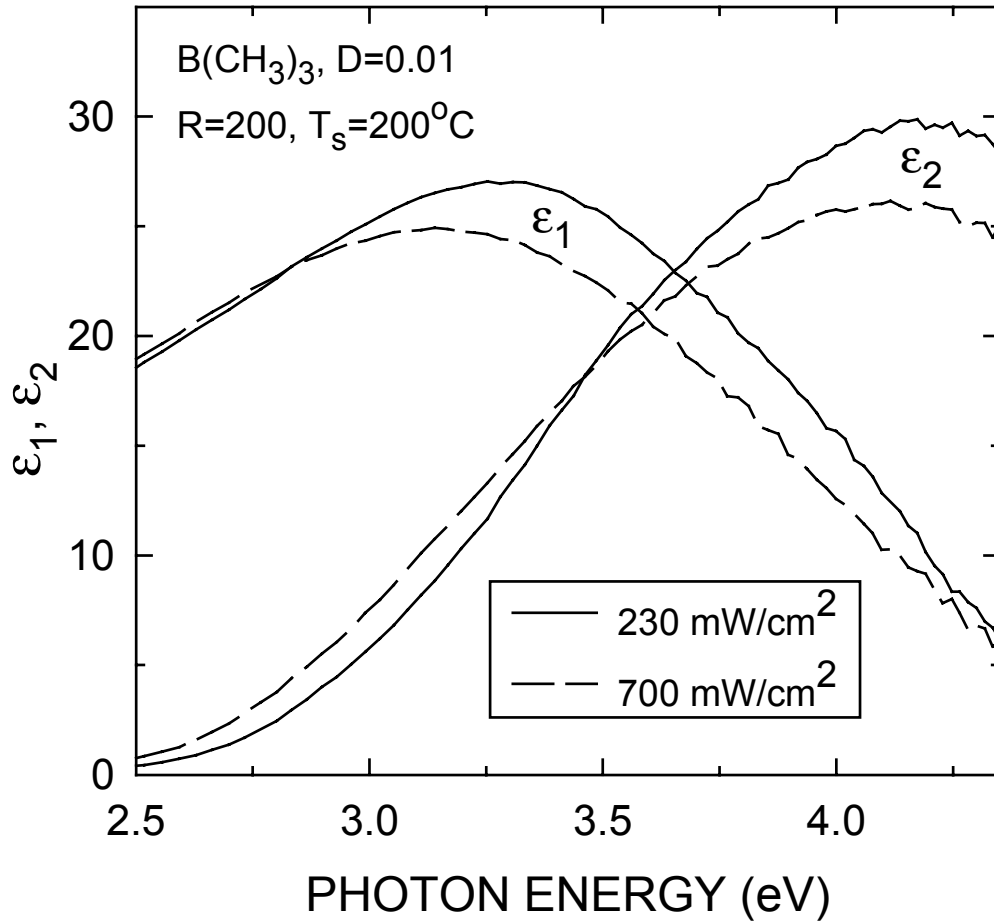


Figure III.2.10 Dielectric functions for 110-120 Å (bulk) p-layers prepared on H₂-plasma treated i-layers using B(CH₃)₃ doping gas with D=0.01, a H₂ dilution ratio of R=200, and plasma powers of 230 mW/cm² (solid line) and 700 mW/cm² (dashed line).

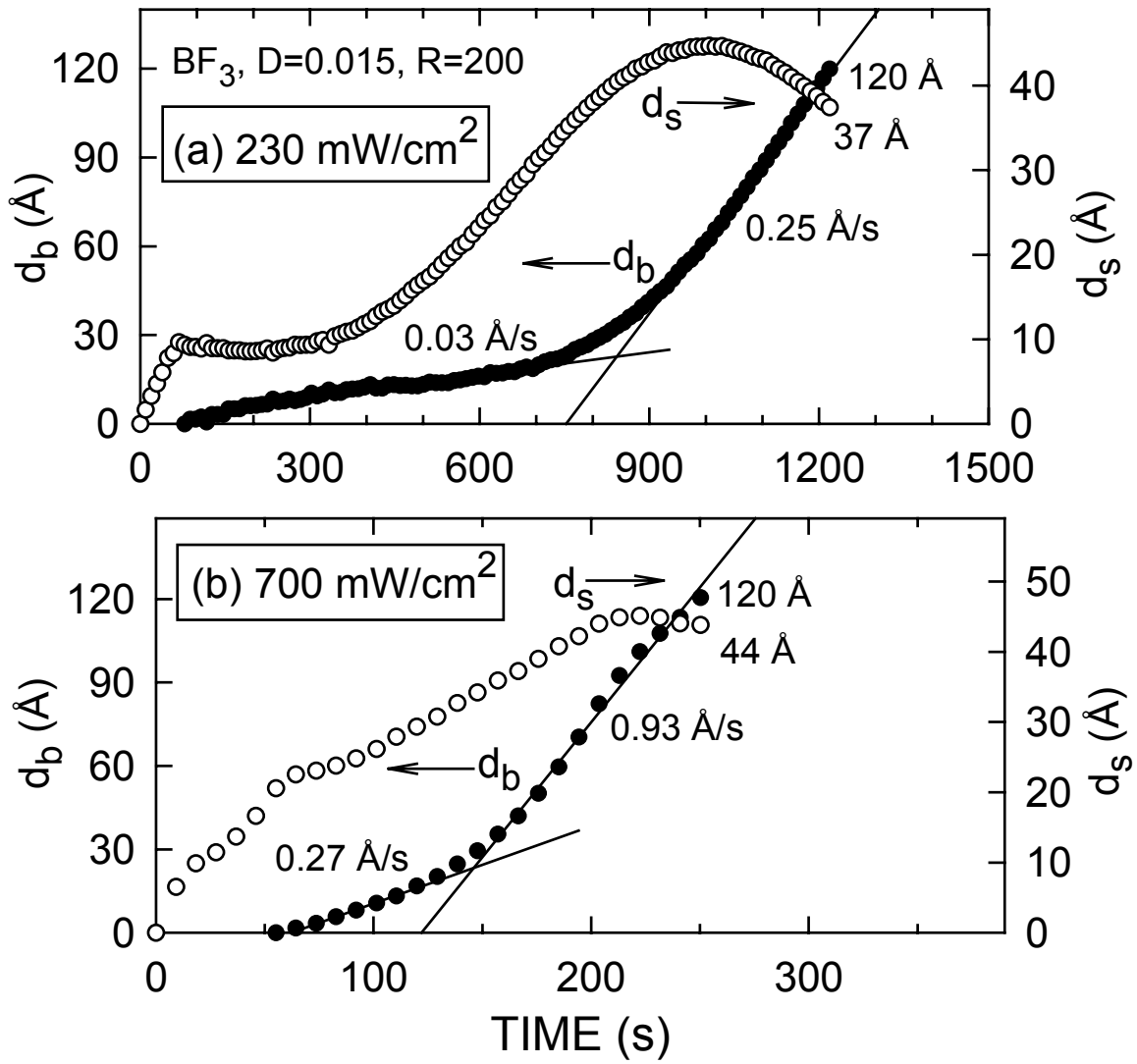


Figure III.2.11 Evolution of the surface roughness layer thickness d_s (open points) and bulk layer thickness d_b (closed points) for 120 Å (bulk) p-layers prepared on H₂-plasma treated i-layers using BF₃ doping gas with $D=0.015$, a H₂ dilution ratio of $R=200$, and plasma powers of (a) 230 mW/cm² and (b) 700 mW/cm².

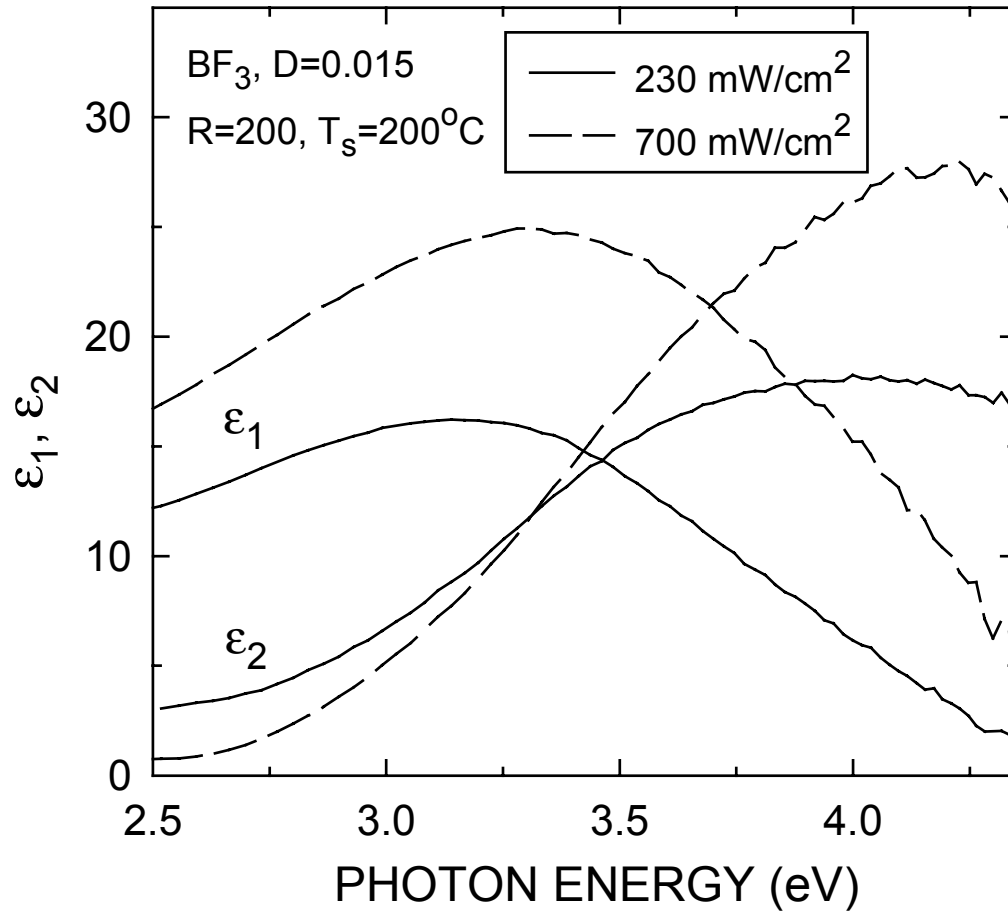


Figure III.2.12 Dielectric functions for 120 Å (bulk) p-layers prepared on H₂-plasma treated i-layers using BF₃ doping gas with D=0.015, a H₂ dilution ratio of R=200, and plasma powers of 230 mW/cm² (solid line) and 700 mW/cm² (dashed line).

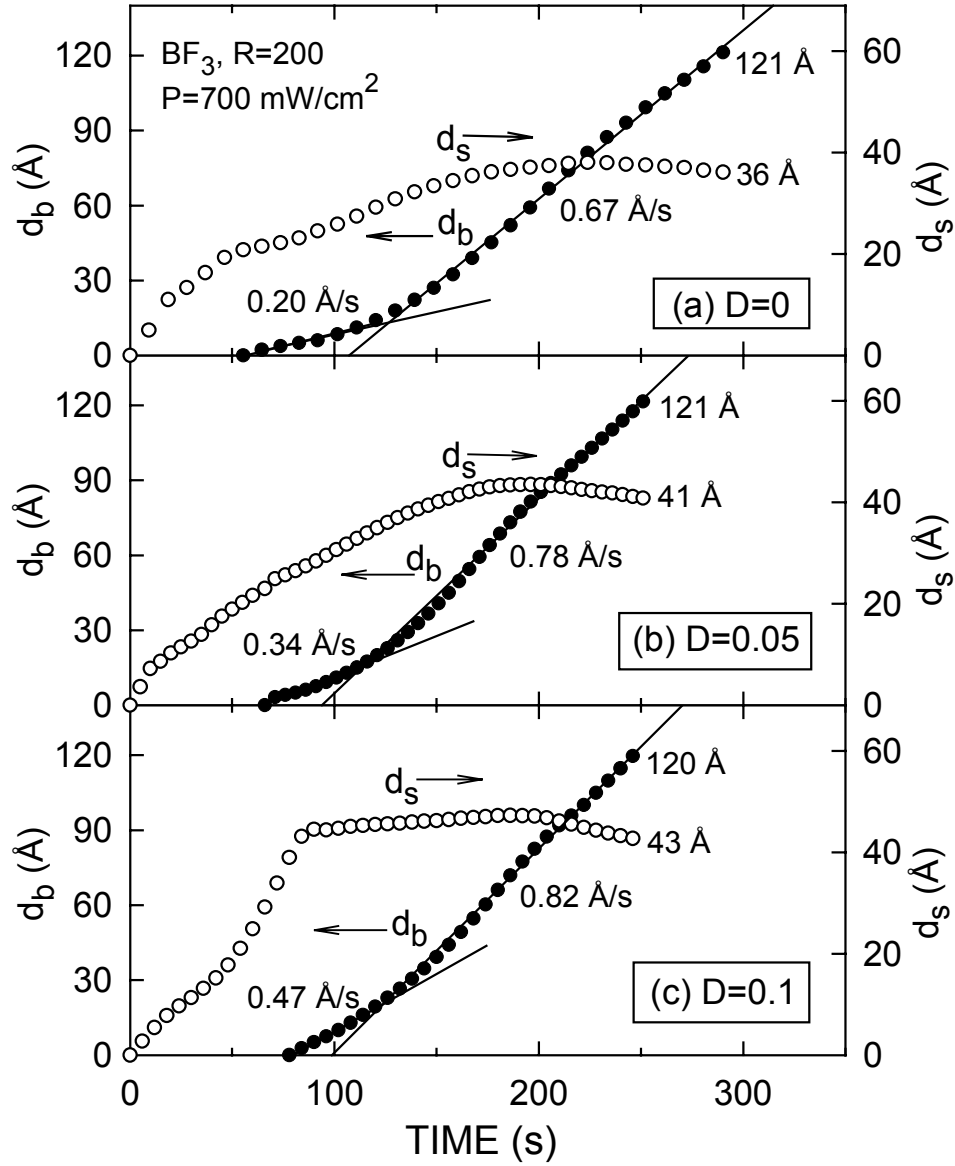


Figure III.2.13 Evolution of the surface roughness layer thickness d_s (open points) and bulk layer thickness d_b (closed points) for 120 Å (bulk) p-layers prepared on H₂-plasma treated i-layers using a H₂ dilution ratio of R=200, and a plasma power of 700 mW/cm². Different BF₃ doping gas flow ratios of (a) D=0, (b) D=0.05, and (c) D=0.10 were employed.

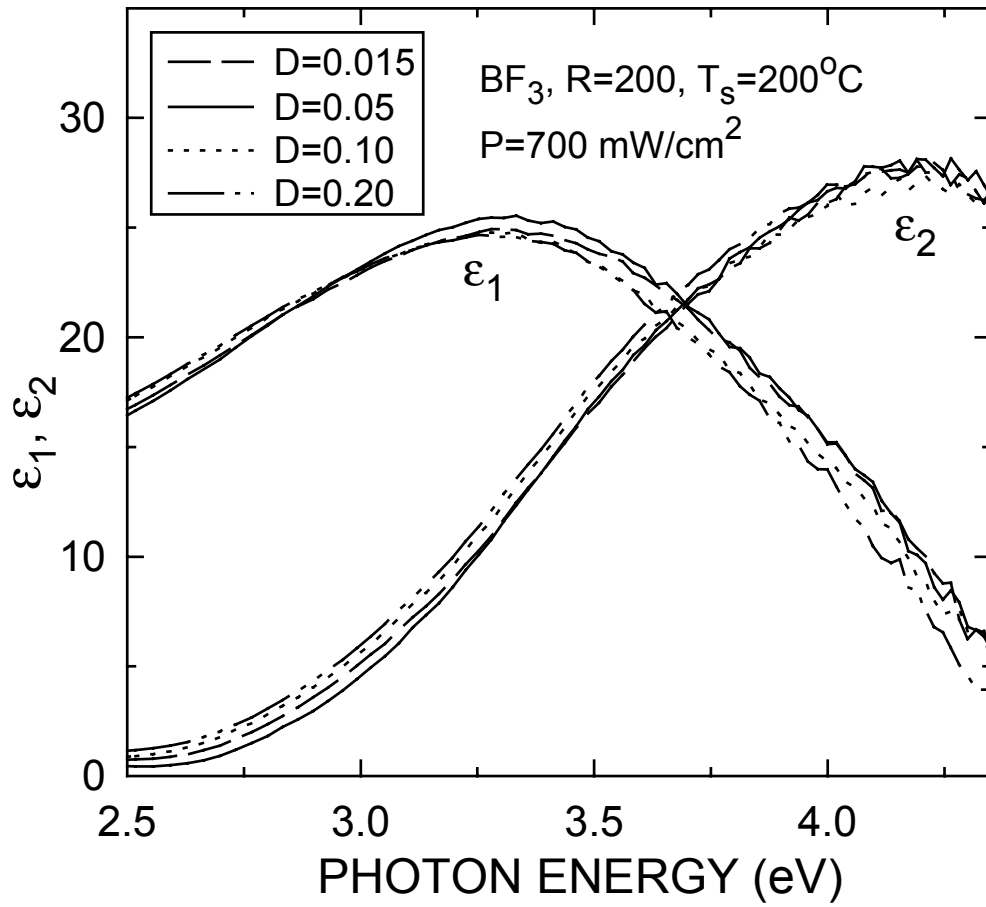


Figure III.2.14 Dielectric functions for 120 Å (bulk) p-layers prepared on H_2 -plasma treated i-layers using a H_2 dilution ratio of $R=200$, and a plasma power of 700 mW/cm^2 . Different BF_3 doping gas flow ratios of $D=0.015$ (dashed line), $D=0.05$ (solid line), $D=0.10$ (dotted line), and $D=0.20$ (dash-dotted line) were employed.

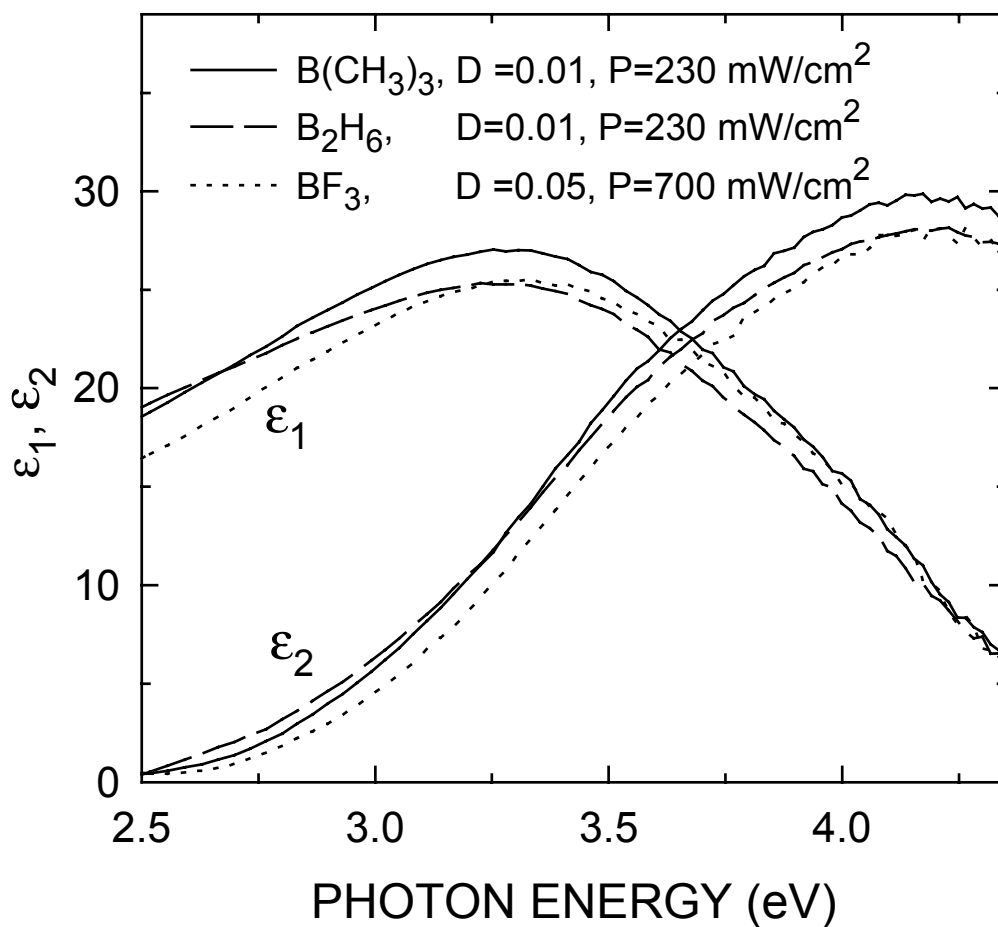


Figure III.2.15 Dielectric functions for 120 Å (bulk) optimum p-layers prepared on H_2 -plasma treated i-layers using a H_2 dilution ratio of $R=200$. Different doping gases were employed, including $B(CH_3)_3$ at $D=0.01$ and a plasma power of 230 mW/cm^2 (solid line), B_2H_6 at $D=0.01$ and a plasma power of 230 mW/cm^2 (dashed line), and BF_3 at $D=0.05$ and a plasma power of 700 mW/cm^2 (dotted line).

III.3. Protocrystalline Intrinsic Layers

Motivation and Overview

Significant progress has been made in improving the performance and stability of a-Si:H based p-i-n and n-i-p solar cells using intrinsic layers prepared with hydrogen dilution of silane [1-5]. It is found that both materials and solar cells prepared with H₂ dilution of SiH₄ exhibit degradation kinetics distinctly different from their undiluted counterparts. They not only exhibit less degradation under AM1.5 illumination (100mW/cm²), but they also reach a degraded steady state within approximately 100 hours [5]. These are distinguishing characteristics of what are called protocrystalline materials—a term used to describe a-Si:H grown close to the microcrystalline phase boundary [1,6,7]. However, there are many unanswered questions not only about the growth of these materials but also about the nature and properties of the amorphous phase, and in particular about the material in the optically deduced transition region between the amorphous and microcrystalline regimes.

The optical properties and microstructural evolution of the transition region can be characterized using real-time spectroscopic ellipsometry (RTSE) which can guide systematic studies on further evaluating the basic material properties as well as their effects on the stabilized performance of solar cells [8]. However, it is very difficult to characterize the basic electronic properties of such a transition region even from quite sophisticated thin film measurements due to the limitations of the experimental techniques with respect to depth profiling [9]. Since the protocrystalline materials by their very nature evolve with thickness, the operation of the coplanar structures used in such thin film measurements is such that the transition material is probed in parallel with the amorphous phase rather than in series. Since in p-i-n (n-i-p) solar cells two such constituent materials are effectively in series, the solar cell can be used to obtain insights not only about the “sharpness” of these transitions but also about changes which are on the order of 10¹⁷cm⁻³ and cannot be detected with optical techniques such as RTSE. However, since p-i-n (n-i-p) cell structures are complex, it is very important to establish that the cell

characteristics being studied, particularly in the degraded steady state (i.e., “end-of-life”), are determined by the bulk intrinsic layer and not by the p-layer and/or the p/i interface region.

A detailed study was carried out on a variety of a-Si:H p-i-n cells whose structures were guided by an evolutionary phase diagram obtained via RTSE. These cells of different thicknesses were fabricated from two types of p contacts and i-layer materials, in which the i-layers were prepared using H₂ dilution ratios, $R=[H_2]/[SiH_4]$, ranging from 0 to 20. The effects of protocrystalline material and its phase transition to microcrystallinity in the i-layers of the p-i-n cell structures were characterized by studying the solar cell characteristics from their annealed states to their AM1.5 degraded steady states.

Experimental Procedures

The a-SiC:H (p)/a-Si:H (i)/ μ c-Si:H (n) structures were deposited in a Tek-Vak MPS 4000 LS multi-chamber rf PECVD system at $T_s=200^\circ\text{C}$ on specular SnO₂. Two different a-SiC:H p-layers (p₁ and p₂) were deposited from the same feedstock gases [SiH₄, B(CH₃)₃, CH₄], with the only difference being their relative doping ratios. p₁ used a doping ratio of $D=[B(CH_3)_3]/[SiH_4]=0.01$ and p₂ used a doping ratio $D=0.005$. Two types of intrinsic layers (i₁ and i₂) were incorporated into the structures using the same deposition conditions but with different electrode spacings (1.91 cm and 2.54 cm, respectively) and hence different deposition rates. The majority of the experiments were carried out with the i₂ intrinsic materials deposited at a rate of 0.36Å/s for $R=10$. The cells were fabricated with 250Å p-type a-SiC:H layers, 350Å n-type μ c-Si:H layers, and 1000Å Cr contacts under deposition conditions that have been reported earlier [5].

The light I-V characteristics of the p-i-n solar cells at 25°C were obtained with AM1.5 illumination from an Oriel model 6258 solar simulator. The light-induced degradation kinetics were obtained under illumination by the solar simulator and by ELH tungsten-halogen lamps, with IR and KG2 filters, calibrated for AM1.5. The cells were illuminated until a degraded

steady state was reached at 25°C. Similar results were obtained using the solar simulator and the ELH lamps.

Results and Discussion

RTSE was used to investigate the structural evolution of films deposited with different H₂ dilution ratios R on a-Si:H (R=0) substrates and under conditions similar to those used in the fabrication of the p-i-n solar cells. The deduced structural evolution identifies the regimes of film thickness and H₂-dilution ratio within which the a-Si:H and the μ c-Si:H phases are obtained. The resulting deposition phase diagram was then used to guide the fabrication of the i-layers for the different cell structures in this study.

Figure III.3.1 shows the surface roughness layer thickness (d_s) versus bulk layer thickness (d_b) for three Si films prepared with R=15, 30, and 80 reproduced from the work of Task I. The initial roughness value at the first monolayer of bulk film growth ($d_b=2.5\text{\AA}$, vertical broken line) is controlled by the roughness of the underlying R=0 a-Si:H substrate film. The key features in Figure III.3.1 are the abrupt increases in surface roughness layer thickness which signify the amorphous to microcrystalline transition for the different R values. These results give rise to the evolutionary phase diagram reproduced in Figure III.3.2. This phase boundary separates the deposition of a-Si:H (left) and μ c-Si:H (right) thin films as a function of layer thickness d_b and H₂ dilution ratio R on a-Si:H (R=0) substrates. Even though the intrinsic layers of the p-i-n cells used in this study were deposited in a different processing chamber and onto different substrates (p-type a-SiC:H), these results can be used as a guide based on the correlations described later in this section. Although studies reported below suggest that for $R \geq 15$ the phase boundary is the same for a-SiC:H p-layers and a-Si:H (R=0) film substrates, additional studies need to be performed at lower R values.

The information about the protocrystalline materials and the onset of the phase transition was obtained primarily from the fill factors of the different cell structures. As a result, studies were carried out first to establish the thickness range of the i-layers over which the fill factors in

the degraded steady state were determined solely by the bulk. As a first step, the dependence of fill factor on the i-layer thickness in the annealed state was investigated for R=10 cells with the same p-layers and p/i interfaces. The results obtained with p_2 -i₂ (R=10)-n structures are shown in Figure III.3.3. There is a systematic increase in the annealed state fill factors from 0.67 at 5500Å to 0.75 at 1800Å after which there is no further increase. Similarly, the fill factors in the degraded steady state increase from 0.56 at 5500Å to 0.70 at 1800Å. These results indicate that above a thickness of 1800Å the fill factors are not limited by the contacts even in the annealed state. It is pointed out here that in this region excellent fill factors are obtained in the degraded steady state, for example 0.70 for 1800Å and 0.65 for 3300Å thick i-layers.

Even though these results indicate bulk domination of the fill factors, it is necessary to ensure that there are no effects on the degraded steady state fill factor due to possible light induced changes in the material near the p/i interfaces [10]. The absence of such effects is indicated by the stability of the open circuit voltages to prolonged illumination. This is illustrated in Figure III.3.4 where the open circuit voltages are shown as a function of AM1.5 illumination time for different thickness p_2 -i₂-n cells with an R=10 i-layer. Since V_{oc} is very sensitive to the p/i interface region [11], the results in Fig. III.3.4 lead to the conclusion that there is no effect of the p/i interface on the stabilized fill factors. The stability of the V_{oc} under AM1.5 illumination indicates that there are not major increases in the defect density in the i-layer near the p/i interface region, a fact that results in fill factors dominated by the bulk i-layer in the degraded steady state. The absence of such an increase in defect density at the p/i interface as well as a contribution of the p-layer to the degraded steady state of the fill factor was further established by comparing the degradation kinetics of cells with different p-layer contacts. Even though the initial fill factors were up to 0.04 higher for cells having p_2 layers and thicknesses from 1800 to 3300Å (compared to cells with p_1 layers) the fill factors were the same in the degraded steady state. This is illustrated in Fig. III.3.5 with the results obtained on two p -i₁-n solar cells with a 3300Å thick R=10 i-layers.

To assess what improvements in cell performance and stability occur with increasing hydrogen dilution and the corresponding changes in the protocrystalline intrinsic materials, p-i-n cells were studied in which the 3300Å i-layer was deposited with $R=0$ to $R=20$. These cells exhibit improved AM1.5 stabilized fill factors as R increases from 0 to 10 and then remain the same up to $R=20$. This is illustrated in Figure III.3.6 where the degradation kinetics are shown from the annealed to the degraded steady states for p_1-i_1 -n cells with $R=5$, $R=10$ and $R=20$ intrinsic layers. Figure III.3.6 also illustrates that the fill factors in the annealed state are constant below $R=10$ and then decrease significantly for $R>10$. The observed decreases in the initial fill factor for $R>10$ are not related to any degradation of the p/i interface region since the insertion of a 200Å $R=20$ p/i interface region in a cell with $R=10$ bulk i-layers leads to improved open circuit voltages in both the initial and degraded steady state [11]. The same trend is also present in the p-i-n cells with i_2 intrinsic layers. Based on the deposition phase diagram, however, such decreases in annealed state fill factors can be attributed to the phase transitions in the i-layers.

Specifically, Fig. III.3.2 shows that the phase boundary to microcrystallinity for $R=15$ and $R=20$ occurs at thicknesses of about 3000Å and 1000Å, respectively.

To further assess the nature of protocrystalline materials (i.e., materials prepared just on the amorphous side of the boundary), the onset of the phase transition, and their effects on solar cell characteristics, cells with R ranging from 10 to 20 and i-layer thicknesses ≤ 3300 Å were investigated. It is found that as the thickness of the i-layers and hence the contribution from the material in the transition region decreases, the values of the annealed state fill factors of the $R=15$ and $R=20$ cells approach the values for the $R=10$ cells. This is illustrated in Fig. III.3.7 where results are shown for cells with 1800Å and 3300Å thick i_2 layers having $R=10$ and 20. Because the fill factors in cells less than 1800Å are limited by the contacts, the initial and degraded steady state fill factors obtained with 1100Å thick i-layers with $R=10$ and $R=20$ were the same. Because of this, the changes that accompany the transition with decreasing thickness across the boundary in Fig. III.3.2 into the amorphous regime could not be evaluated for $R=20$.

Such a transition with decreasing thickness could be studied, however, with $R=15$ i-layers because a thickness less than 3000\AA should be amorphous according to Figure III.3.2. In this case $R=10$ and 15 cells with 2400\AA and 1800\AA thick i-layers gave identical fill factors both in the annealed and degraded states and their light induced changes were identical as well. These results clearly demonstrate the absence of deleterious effects on the annealed state of the materials associated with the phase transition range. The results also indicate that in this region of thickness the properties of the protocrystalline materials fabricated with $R=10$ and $R=15$ are indistinguishable. Thus, there appears to be no significant benefit in increasing R from 10 to 15 while remaining in the amorphous regime (thicknesses less than 3300\AA). This is consistent with optical studies that have shown that the largest improvement in ordering occurs in the protocrystalline regime of larger R (~ 40) and thinner layers ($\sim 200\text{\AA}$) [1].

Concluding Remarks

A study has been carried out on p-i-n solar cells with protocrystalline intrinsic materials which was guided by an evolutionary phase diagram obtained from real-time optics. New information was obtained about the nature of the protocrystalline materials and the transitions to the microcrystalline phase. In this study, a range of cell thicknesses was identified for which the fill factors could be directly related to the bulk i-layer material. From results on fill factors in the annealed and AM1.5 degraded steady states, the presence and the effects of the transition region from the amorphous to the microcrystalline phase were evaluated. The results clearly show that the i-layer materials with $R=15$ and 20 deposited to a thickness that spans the amorphous to microcrystalline transition have inferior properties in the annealed state but exhibit higher stability than materials that remain amorphous throughout the entire thickness. By maintaining the amorphous phase throughout the entire thickness for $R=15$ intrinsic layers it was found that their contributions to cell performance and stability were indistinguishable from $R=10$ materials. Additional studies must be carried out to further characterize the protocrystalline materials and

the nature of the phase transitions on the nanoscale and its effects on defect densities less than 10^{17} cm^{-3} .

References

1. J. Koh, Y. Lee, H. Fujiwara, C.R. Wronski, R.W. Collins, Appl. Phys. Lett. **73**, 1526 (1998).
2. J. Yang, X. Xu, and S. Guha, Mater. Res. Soc. Symp. Proc. 336, 687 (1994).
3. M. Bennett, K. Rajan, and K. Kritikson, Conf. Record of 23rd IEEE PVSC, (IEEE, New York, 1994), p. 845.
4. L. Yang and L.-F. Chen, Mater. Res. Soc. Symp. Proc. 336, 669 (1994).
5. Y. Lee, L. Jiao, H. Liu, Z. Lu, R.W. Collins, and C.R. Wronski, Conf. Record of the 25th IEEE PVSC, (IEEE, New York, 1996), p.1165.
6. Y. Lu, S. Kim, M. Gunes, Y. Lee, C.R. Wronski, R.W. Collins, Mater. Res. Soc. Symp. Proc. 336, 595 (1994).
7. D.V. Tsu, B.S. Chao, S.R. Ovshinsky, S. Guha, and J. Yang, Appl. Phys. Lett. 71, 1317 (1997).
8. Joohyun Koh, Y. Lu, S. Kim, J. S. Burnham, C. R. Wronski, and R. W. Collins, Appl. Phys. Lett. 67, 2669 (1995).
9. L. Jiao, Ph.D. Thesis, The Pennsylvania State University, 1998.
10. R. Platz, D. Fischer, C. Hof, S. Dubail, J. Meier, U. Kroll, and A. Shah, Mater. Res. Soc. Symp. Proc. 420, 51 (1996).
11. Y. Lee, A.S. Ferlauto, Z. Lu, J. Koh, H. Fujiwara, R.W. Collins, and C.R. Wronski, 2nd World Conference and Exhibition on Photovoltaic Solar Energy Conversion, (Arte Stampa, Daverio [VA], 1998), p. 940.

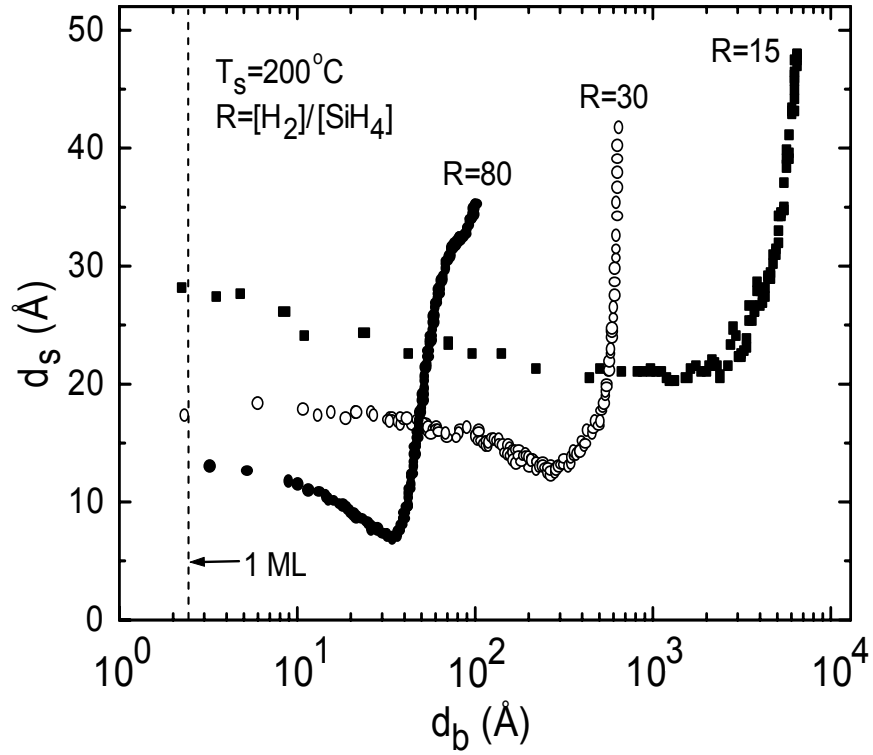


Figure III.3.1. Surface roughness layer thickness (d_s) versus bulk layer thickness (d_b) obtained from RTSE measurements during the growth of three Si:H films prepared with $R=[H_2]/[SiH_4]$ of 15, 30, and 80. The underlying substrate is a-Si:H prepared with $R=0$. The vertical line at $d_b \sim 2.5$ Å corresponds to a monolayer thickness [11].

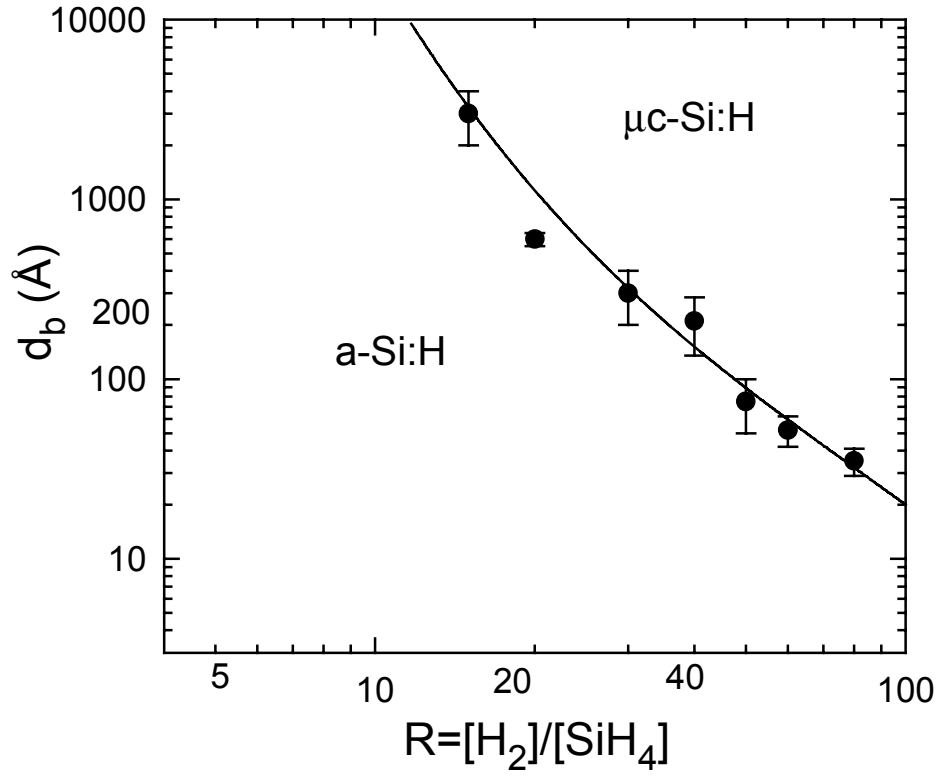


Figure III.3.2. Evolutionary phase boundary separating the deposition of a-Si:H (left) and μc-Si:H (right) thin films as a function of layer thickness d_b and H_2 dilution ratio R on an a-Si:H ($R=0$) substrate [11].

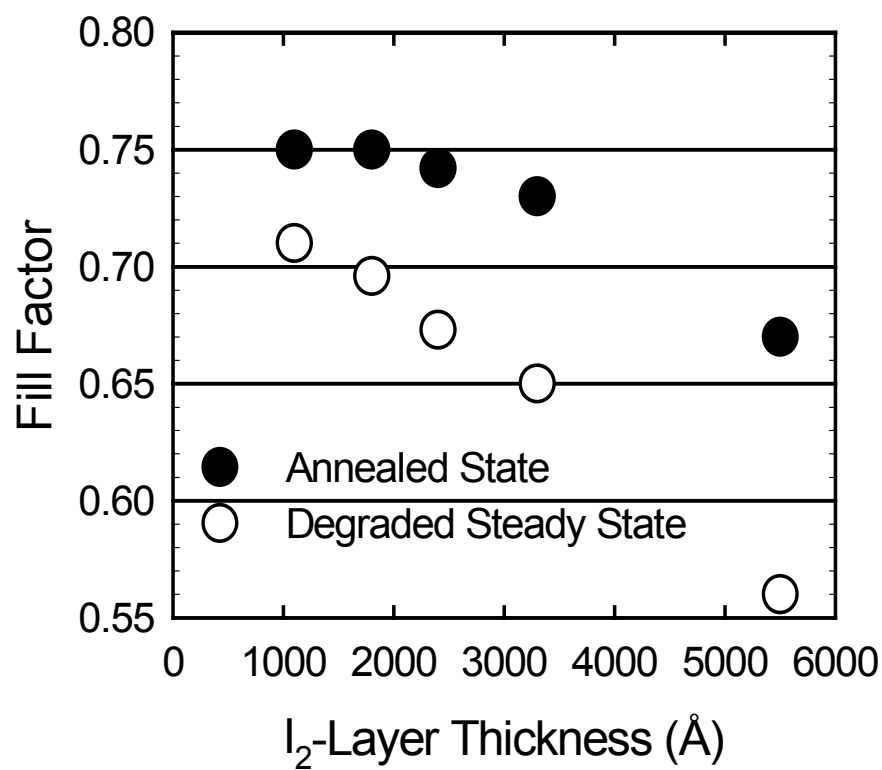


Figure III.3.3. Annealed and degraded steady state fill factors of R=10 p₂-i₂-n cells versus cell thickness.

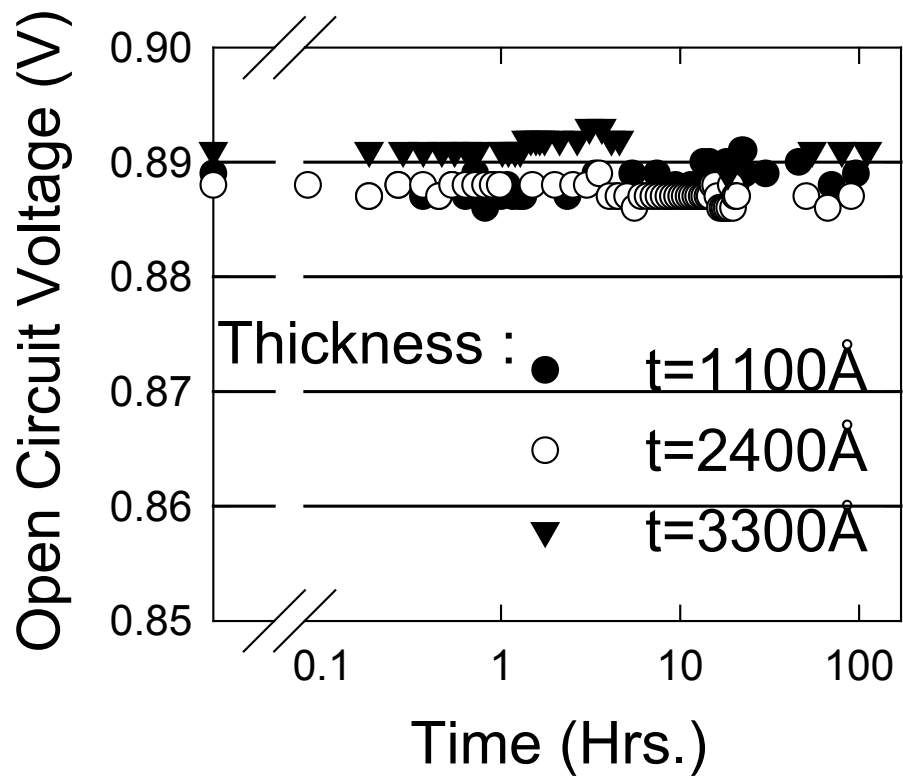


Figure III.3.4. AM1.5 25°C degradation of the V_{oc} of $p_2-i_2(R=10)-n$ cells of different thickness.

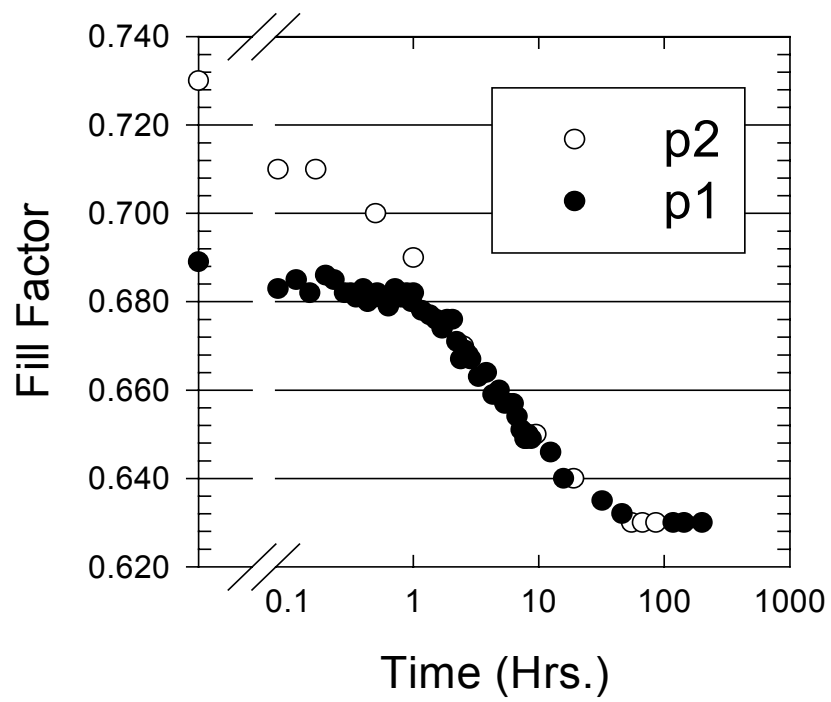


Figure III.3.5. AM1.5 25°C degradation of p-i₁(R=10)-n cells having different p-layers.

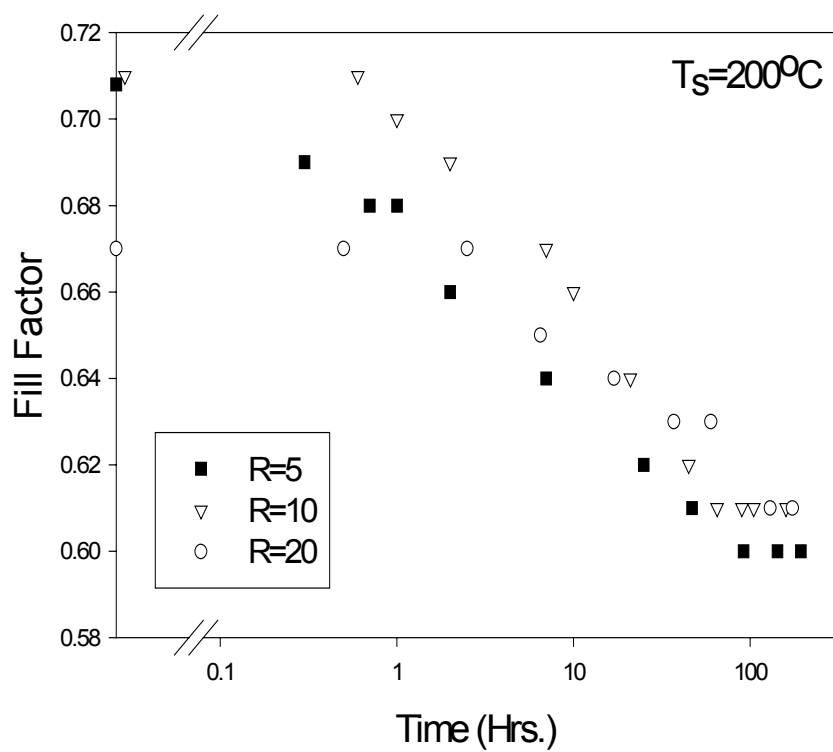


Figure III.3.6. AM1.5 25°C degradation of 3300Å p₁-i₁-n cells with R=5, 10, 20.

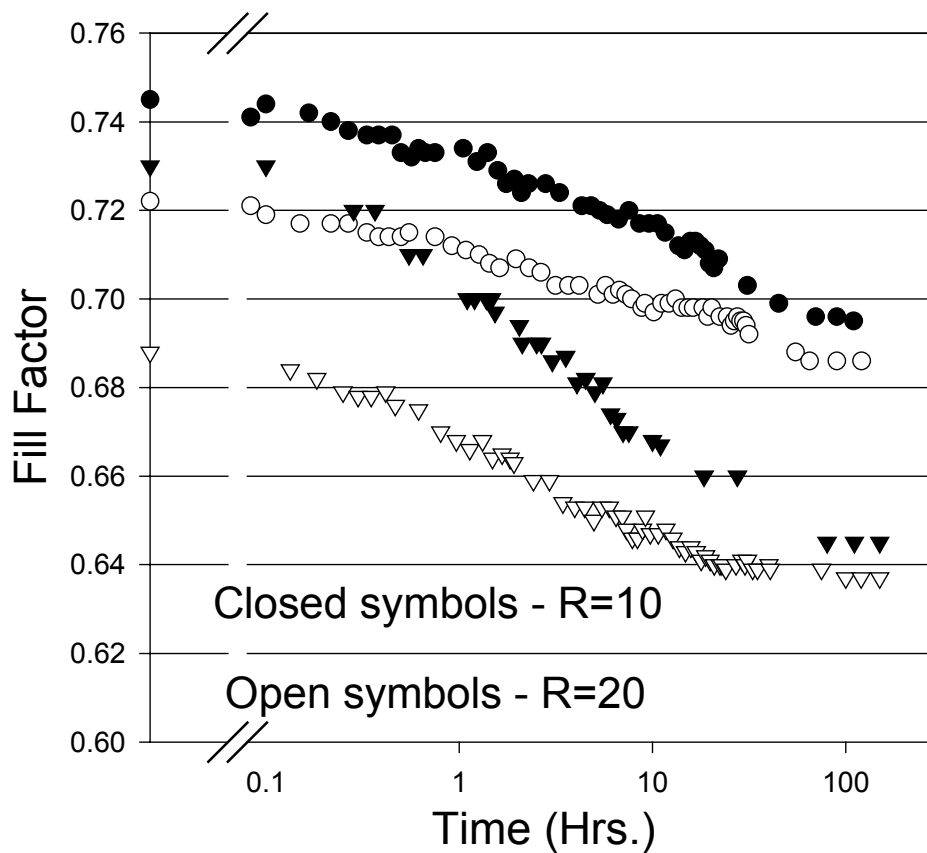


Figure III.3.7. AM1.5 25°C degradation of a-Si:H (R=10,20) p₂-i₂-n cells with i-layer thicknesses of 1800 and 3300 Å illustrating the effect of phase transitions in the i-layers on the cell in both the annealed and degraded steady states.

TASK IV: Optimization of Multijunction Solar Cells

IV.1 Textured TCO Studies

Motivation and Overview

Studies of the optics of textured surfaces and interfaces in hydrogenated amorphous silicon

(a-Si:H) solar cells are important for two reasons. First, analytical descriptions of the processes of specular reflection and transmission, and non-specular scattering at the textured surfaces and interfaces of a-Si:H solar cells are required to develop realistic multilayer optical models that can direct improvements in the optical engineering of the devices used in production. Second, real time optical characterization methods suitable for textured surfaces are in demand because they permit production line monitoring of the processes used in industry.

The roughness associated with textured surfaces and interfaces exists over a range of scales. For the purposes of optical modeling, we define microroughness as having in-plane correlation lengths L smaller than the minimum wavelength λ_m of the light of interest for solar cell collection, and macroroughness as having correlations lengths on the same order as the wavelength (λ) range of interest. The effect of microroughness on the incident light beam can be modeled using an effective medium theory (EMT). In this case, the roughness can be simulated as an additional layer of the solar cell whose optical properties are determined from the EMT as a microscopic mixture of the underlying and overlying materials. [1,2] The effect of macroroughness can be modeled using a variety approaches from simple scalar diffraction to first principles theories. [3,4]

RTSE studies performed prior to 1998 employed the rotating polarizer multichannel ellipsometer configuration. [5] Such an instrument is unsuitable for characterizing textured surfaces owing to the scattering and non-uniformity that lead to depolarization of the incident polarized beam upon reflection ($p < 1$). A rotating polarizer instrument erroneously interprets a randomly polarized component superimposed on linearly polarized light, for example, as

elliptically polarized light. In contrast, the recently developed rotating compensator multichannel ellipsometer allows one to analyze polarized and unpolarized components of the beam separately. [6] Thus, it provides not only (ψ, Δ) versus E and t , which characterize the polarization change induced by the sample, but also the degree of polarization p which characterizes the depolarization. The rotating compensator instrument has also been developed with the capability of determining the spectroscopic reflectance. [7] As a result, the spectra in (ψ, Δ) can be analyzed to determine the microscopic structure of the film stack at any given time during the growth process, whereas the deviation of the measured reflectance spectrum from that predicted theoretically from the analysis of (ψ, Δ) can be applied to characterize the macroscopic structure at any given time. The overall results provide a better understanding of how the irradiance in the incident beam is partitioned into specular reflection and transmission and non-specular scattering at interfaces, and thus, possible improved optical engineering of solar cell designs.

Experimental Procedures

The instrument used for real time studies in this task consists of a Xe source, fixed polarizer, sample in the PECVD reactor, rotating-compensator, fixed analyzer, spectrograph, and photodiode array detector [6]. With this instrument, four spectra from 1.4 to 4.0 eV in $\{(Q, \chi), p, R\}$ are collected simultaneously with a total acquisition time of 0.8 s. The repetition time ranges from 3.5 s for the p-layer and early stages of the i-layer, to 50 s in the later stages of i-layer growth. (Q, χ) are the tilt and ellipticity angles of the ellipse of polarization, p is the degree of polarization, and R is the reflectance of the sample for incident light polarized at an angle of $P'=45^\circ$ measured with respect to the plane of incidence.

The a-Si:H p-i-n solar cell studied here was prepared by rf plasma enhanced chemical vapor deposition (PECVD) onto Asahi U-type textured SnO_2 held at 200°C . The $\text{a-Si}_{1-x}\text{C}_x\text{:H:B}$ ($x \sim 0.05$) p-layer was prepared to an estimated thickness of 200 Å using 6:4:0.02:1 flow ratios of $\text{SiH}_4\text{:CH}_4\text{:B(CH}_3)_3\text{:He}$. The a-Si:H i-layer was prepared to 5000 Å using 20 sccm of SiH_4 , and

the a-Si:H:P n-layer was prepared to 300 Å using a 10:0.12 flow ratio of SiH₄:PH₃. The plasma power for the three layers was 70 W/cm², and the total gas pressures were in the range 0.1-0.2 Torr.

Results and Discussion

Analysis of the uncoated SnO₂ film and a-Si:H solar cell fabrication involves breaking the optical problem into two parts (see Fig. IV.1.1 for the case of the uncoated SnO₂) [7]. First, (Q, χ) are converted to the ellipsometry angles (ψ, Δ) assuming an ideal sample. Then (ψ, Δ) are interpreted to deduce the layer thicknesses, microscopic roughness ($L \ll \lambda_m$), and layer optical properties in the same way as for a specular sample [see Fig. IV.1.1(b)]. Second, with the microscopic optical problem solved, the reflectance R that would be predicted for a specular structure is calculated. The differences between the predicted and measured spectra in R are attributed to integrated scattering losses generated by macroscopic roughness with $L \sim \lambda$. The reflectance loss can be modeled using a scalar diffraction theory [3,7] that predicts a dampening of the Fresnel amplitude reflection and transmission coefficients in accordance with $c = c_0 \exp(-\sigma_s \Delta k_c / 2)$ ($c = r, t$) for Lorentzian-distributed macroscopic roughness, i.e., for a surface distribution $w(z)$ given by $w(z) = 2\sigma_s [\pi(4z^2 + \sigma_s^2)]^{-1}$, where z is the height from the average surface plane and σ_s is the full-width at half-maximum (FWHM) [see Fig. IV.1.1(c)]. Δk_c ($c = r, t$) is the change in propagation vector normal to the surface.

For this overall analysis approach to be valid, three conditions must apply [7, 8]: (i) light scattering from the textured film must be independent of the incident polarization and must be rejected by the high $f/\#$ detection system; (ii) the detected beam must be describable as an incoherent superposition of components from different areas of the SnO₂ surface, i.e., from areas that are separated by distances larger than the lateral coherence of the beam, and (iii) the resulting incoherent superposition from areas with different SnO₂ and/or a-Si:H thicknesses must provide polarization information that accurately represents the average thickness and the optical properties. Previous studies [6,7] along with corroborative measurements of the deduced

microstructure suggest that these conditions do apply for the textured SnO₂ and for overlying a-Si:H solar cell fabrication. In the future, it may also be possible to extend the analysis further by addressing a third aspect of the reflected wave, namely, the degree of polarization p which deviates from unity in part owing to the non-uniformity of the SnO₂ [6]. In principle, analysis of p can provide information on the thickness distribution having correlation lengths larger than the lateral coherence of the beam ($L \gg \lambda$).

This overall approach can be first demonstrated through the analysis of the Asahi U-type textured SnO₂ on glass which serves as the starting surface for p-i-n cell fabrication. Figure IV.1.2 shows spectra in (ψ, Δ) and the reflectance R for the bare textured SnO₂. Analysis of the (ψ, Δ) spectra using standard least-squares regression methods [9] yields the SnO₂ film microstructure and optical properties at room temperature before heating as shown in Fig. IV.1.3. The best fit microscopic model of the textured SnO₂ consists of three layers depicted in the inset of Fig. IV.1.3. The first layer simulates a low density region at the interface to the glass; the second layer describes the bulk region; and the third top-most layer describes the microscopically rough surface. The best fit dielectric function of Fig. IV.1.3 uses a sum of Tauc-Lorentz [10] and Drude expressions for ϵ_2 , and a Kramers-Kronig integration for ϵ_1 . The minimum value of ϵ_2 near 2.5 eV is 0.02, which corresponds to an absorption coefficient α of $\sim 1 \times 10^3 \text{ cm}^{-1}$, and a single pass loss of $\sim 5\%$ at normal incidence through the 6180 Å thick bulk layer. This is near the limit of sensitivity for determining α by RTSE.

The microstructure and optical properties from Fig. IV.1.3 yield the fit to the (ψ, Δ) spectra in Fig. IV.1.2 given by the solid lines. An analysis of the reflectance in Fig. IV.1.2 starts with the microscopic optical model of Fig. IV.1.3; however, such a model leads to a reflectance spectrum that exceeds the experimental one by 0.2-0.3, owing to the fact that losses by scattering are not included in the model of Fig. IV.1.3. By adding a macroscopic roughness distribution having a Lorentzian surface profile, an excellent fit (solid line) to the measured reflectance R can be obtained for $\sigma_s = 770 \text{ Å}$. Thus, an optical model for the Asahi U-type SnO₂ includes the

microscopic structure of Fig. IV.1.3 with a macroscopic modulation of the top two interfaces having a FWHM of 770 Å.

Figure IV.1.4 shows the microstructural model ($L \ll \lambda_m$) a-Si_{1-x}C_x:H:B for p-layer deposition on the textured SnO₂. To analyze film growth on the SnO₂ surface, three photon energy independent parameters are used: (i) $f_i(\text{a-Si}_{1-x}\text{C}_x\text{:H:B})$ which describes the filling of the microscopic modulations in the SnO₂ surface by depositing p-layer material; (ii) $d_s(\text{a-Si}_{1-x}\text{C}_x\text{:H:B})$ which describes the thickness of the p-layer extending above the SnO₂ modulations; and (iii) $f_s(\text{a-Si}_{1-x}\text{C}_x\text{:H:B})$ which describes the volume fraction of p-layer material within the layer of thickness $d_s(\text{a-Si}_{1-x}\text{C}_x\text{:H:B})$. The dielectric function of the p-layer is obtained simultaneously in the analysis along with these three parameters.

Figure IV.1.5 shows the best fit results for the microstructural evolution of the p-layer, including the parameters $d_s(\text{a-Si}_{1-x}\text{C}_x\text{:H:B})$ and $f_i(\text{a-Si}_{1-x}\text{C}_x\text{:H:B})$. The parameter $f_s(\text{a-Si}_{1-x}\text{C}_x\text{:H:B})$ is fixed at 0.35 since this best fit value varies little over time. The parameter $d_{\text{eff}}(\text{a-Si}_{1-x}\text{C}_x\text{:H:B})$ in Fig. IV.1.5 is the effective thickness of the p-layer; i.e., the p-layer thickness that would be obtained for uniform, microscopically-smooth film growth on an ideal substrate such as c-Si. In general for material x, d_{eff} is given by $d_{\text{eff}}(x) = f_i(x)d_i(x) + d_b(x) + f_s(x)d_s(x)$. The deduced effective thickness for the p-layer of 201 Å in Fig. IV.1.5 is remarkably close to the intended thickness of 200 Å. Obtaining the intended d_{eff} requires careful deposition timing using the p-layer rate measured from a c-Si wafer substrate. It is surprising that the effective thickness of the 200 Å p-layer can be determined to better than 1% when growth occurs on a SnO₂ surface with 450 Å of microscopic roughness (which is partially filled in by the p-layer) and an even thicker layer associated with macroscopic roughness (which is conformally covered by the p-layer).

Figure IV.1.6 shows the corresponding results for i-layer growth. Here, four parameters are plotted; in addition to $d_s(\text{a-Si:H})$ and $f_i(\text{a-Si:H})$ as in Fig. IV.1.5, the surface layer material fraction $f_s(\text{a-Si:H})$ and the bulk layer thickness $d_b(\text{a-Si:H})$ are shown. The bulk i-layer thickness increases above zero in this case once the roughness at the p/i interface is completely filled by i-

layer material [$f_i(\text{a-Si:H})=0.65$]; thereafter, $f_i(\text{a-Si:H})$ is fixed such that $f_s(\text{a-Si}_{1-x}\text{C}_x\text{H:B})+f_i(\text{a-Si:H})=1$ (horizontal broken line in Fig. IV.1.6, upper panel). The effective layer thickness in this case is given by $d_{\text{eff}}=f_i d_i+d_b+f_s d_s$, where all quantities pertain to a-Si:H. We note that values of $d_b(\text{a-Si:H})$ greater than 4500 Å cannot be determined due to the nearly complete loss of interference fringes over the spectral range of analysis. The extrapolated final effective layer thickness is 4892 Å [see solid line for $d_b(\text{a-Si:H})$ in Fig. IV.1.6, lower panel], in very good agreement with the intended value of 5000 Å. One observation in Fig. IV.1.6 that differs from corresponding analysis results for a-Si:H p-i-n solar cell deposition [11] on much smoother specular SnO₂ [with $d_s(\text{SnO}_2)=100$ Å] is the extensive microscopic roughness on the a-Si:H even at the end of the i-layer deposition. Such microscopic roughness, modeled with the Bruggeman EMT, must be included in any realistic optical model of the solar cell. In an assessment of five different EMT's to simulate the optical properties of such microroughness layers, the Bruggeman EMT was found to provide the best fit to the evolution of the (ψ, Δ) spectra in the bulk i-layer growth regime where surface microroughness is most influential.

Figure IV.1.7 shows a comparison between the evolutions of the macroscopic roughness $\sigma_s(\text{a-Si:H})$ as deduced from an analysis of R and the microscopic roughness $d_s(\text{a-Si:H})$ deduced from the analysis of (ψ, Δ) . Both are plotted as a function of time during i-layer deposition after complete interface filling has occurred. It is interesting to note that although the microscopic roughness decays by more than a factor of four relative to the initial starting value for the SnO₂, the macroscopic roughness decays by only ~20%.

The dielectric functions of the p- and i-layers from the analyses of Figs. IV.1.5 and 6 are shown in Fig. IV.1.8 (solid lines). The result for the p-layer is obtained by fitting dielectric function data obtained by numerical inversion of (ψ, Δ) spectra at $d_{\text{eff}}=201$ Å using the Tauc-Lorentz model. The result of the i-layer is obtained by numerical inversion of the (ψ, Δ) spectra at bulk and surface microroughness layer thicknesses of 1985 and 150 Å, respectively. In both cases the shape of the dielectric function is found to be consistent with the Tauc-Lorentz model [10]. The broken lines in Fig. IV.1.8 show the corresponding best fits to the dielectric functions

of identically-prepared p- and i-layers on specular SnO₂. Although the agreement is reasonable in both cases, consistent differences occur. For example, the amplitudes of both parts of the dielectric function are reduced for the textured i-layer. It is not yet clear whether this effect is due to a higher i-layer void content, or to inaccuracies inherent in extracting optical properties in the presence of macroroughness that scatters up to 30% of the power from the specular beam.

In order to assess the validity of the roughness layer thicknesses on the uncoated and over-deposited SnO₂, these samples were measured *ex situ* by atomic force microscopy (AFM). Figure IV.1.9 shows the distribution of the maximum peak-to-valley vertical distances d_{p-v} for the uncoated textured SnO₂ and the final solar cell on the SnO₂ [7]. Each count plotted on the ordinate in Fig. IV.1.9 was obtained by considering the surface topography within one of a large number of $0.1 \times 0.1 \mu\text{m}^2$ boxes excised from $5 \times 5 \mu\text{m}^2$ images in order to restrict the analysis to the microscopic roughness. (Note that a correlation with root-mean-square values from AFM would be ambiguous.) Excellent agreement is obtained between the optical measurement of microscopic roughness (d_s) and the AFM measurement ($\langle d_{p-v} \rangle$, the average value of d_{p-v}): 450 versus 430 Å for the uncoated SnO₂ and 100 Å versus 120 Å for the completed solar cell. Figure IV.1.10 shows $5 \times 5 \mu\text{m}^2$ images of (a) the uncoated SnO₂ surface and (b) the solar cell surface along with (c) one dimensional Fourier analyses along the diagonal lines indicated on the images. It is clear that upon solar cell deposition on the SnO₂, the microscopic roughness is suppressed to a greater degree than the macroscopic roughness, as also indicated in Fig. IV.1.7. Further quantitative corroboration of the macroscopic roughness is needed to support the simple diffraction-based optical model used here.

Concluding Remarks

Real time Stokes vector spectroscopy (also called polarimetry) has been applied to study the effects of textured a-Si:H p-i-n solar cells on incident polarized light. This technique is powerful because it provides spectroscopic information on polarization modification, depolarization, and reflectance of the textured structure throughout solar cell fabrication. We

have developed analysis ingredients necessary to model such spectra. These include enhanced microscopic roughness at interfaces, whose optical effects are simulated using interface layers with optical properties determined by an effective medium theory, as well as macroscopic roughness at interfaces, whose optical effects on the specular beam are modeled using modified amplitude reflection coefficients.

References

1. G. A. Niklasson, C. G. Granqvist, and O. Hunderi, *Appl. Opt.* **20**, 26 (1981).
2. D. E. Aspnes, *Thin Solid Films* **89**, 249 (1982).
3. P. Beckmann and A. Spizzichino, *The Scattering of Electromagnetic Waves from Rough Surfaces* (Pergamon, Oxford, 1963).
4. J. M. Bennett and L. Mattsson, *Introduction to Surface Roughness and Scattering* (Optical Society of America, New York, 1990), Vol. 1.
5. R.W. Collins, *Rev. Sci. Instrum.* **61**, 2029 (1990).
6. J. Lee, P. I. Rovira, I. An, and R. W. Collins, *Rev. Sci. Instrum.* **69**, 1800 (1998).
7. P. I. Rovira and R. W. Collins, *J. Appl. Phys.* **85**, 2015 (1999).
8. M. D. Williams and D. E. Aspnes, *Phys. Rev. Lett.* **41**, 1667 (1978).
9. G.E. Jellison, Jr., *Thin Solid Films* **233**, 416 (1993).
10. G. E. Jellison, Jr., and F. A. Modine, *Appl. Phys. Lett.* **69**, 371 (1996); **69**, 2137 (1996).
11. J. Koh, Y. Lu, S. Kim, J. S. Burnham, C. R. Wronski, and R. W. Collins, *Appl. Phys. Lett.* **67**, 2669 (1995).

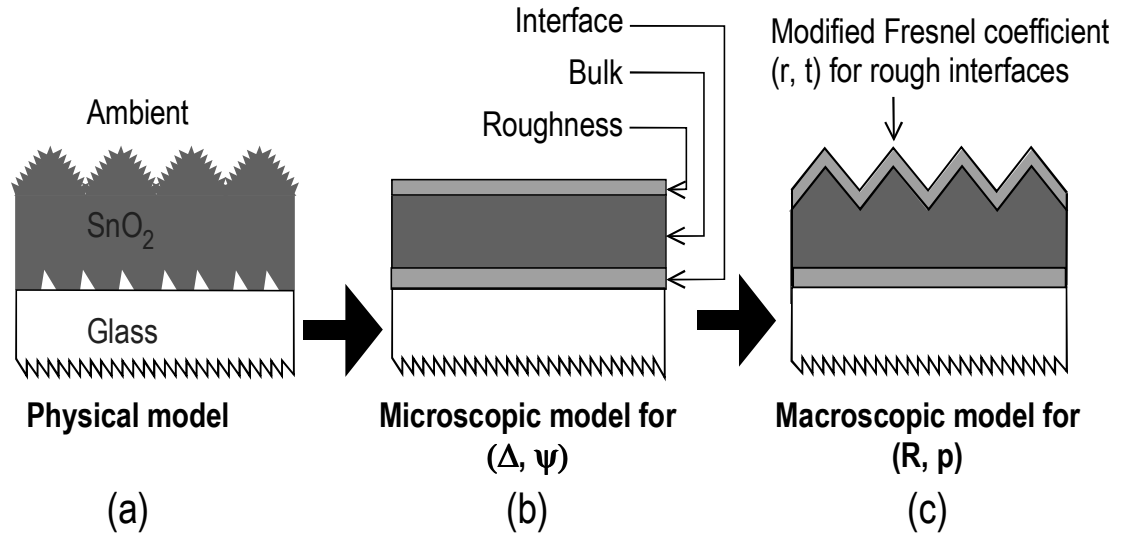


Figure IV.1.1 (a) Schematic physical model for a textured SnO_2 film on glass, along with the decomposition into (b) the microscopic model used in the analysis of (ψ, Δ) and (c) the macroscopic model used in the analysis of the polarized reflectance R .

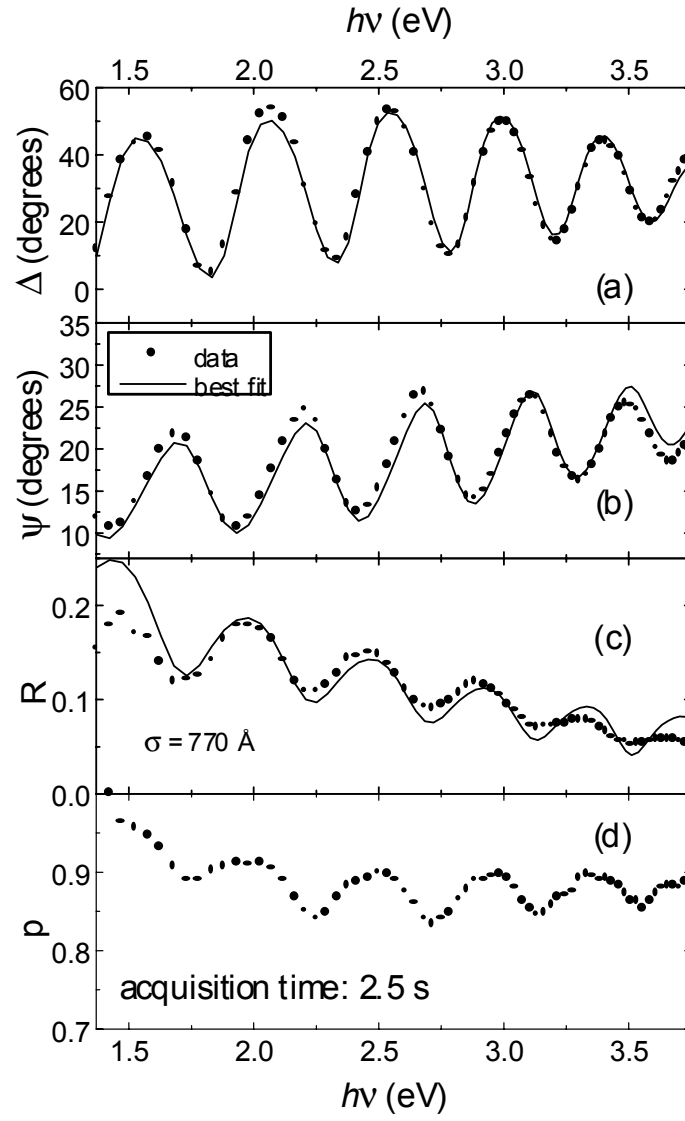


Figure IV.1.2 (a) ψ , (b) Δ , (c) the reflectance, and (d) the degree of polarization spectra for Asahi U-type textured SnO_2 . The fits to (ψ , Δ) (solid lines) are obtained using the microscopic structural model of Fig. IV.1.3. The fit to the reflectance employs in addition a Lorentzian macroscopic roughness distribution with a full-width at half-maximum of 770 Å.

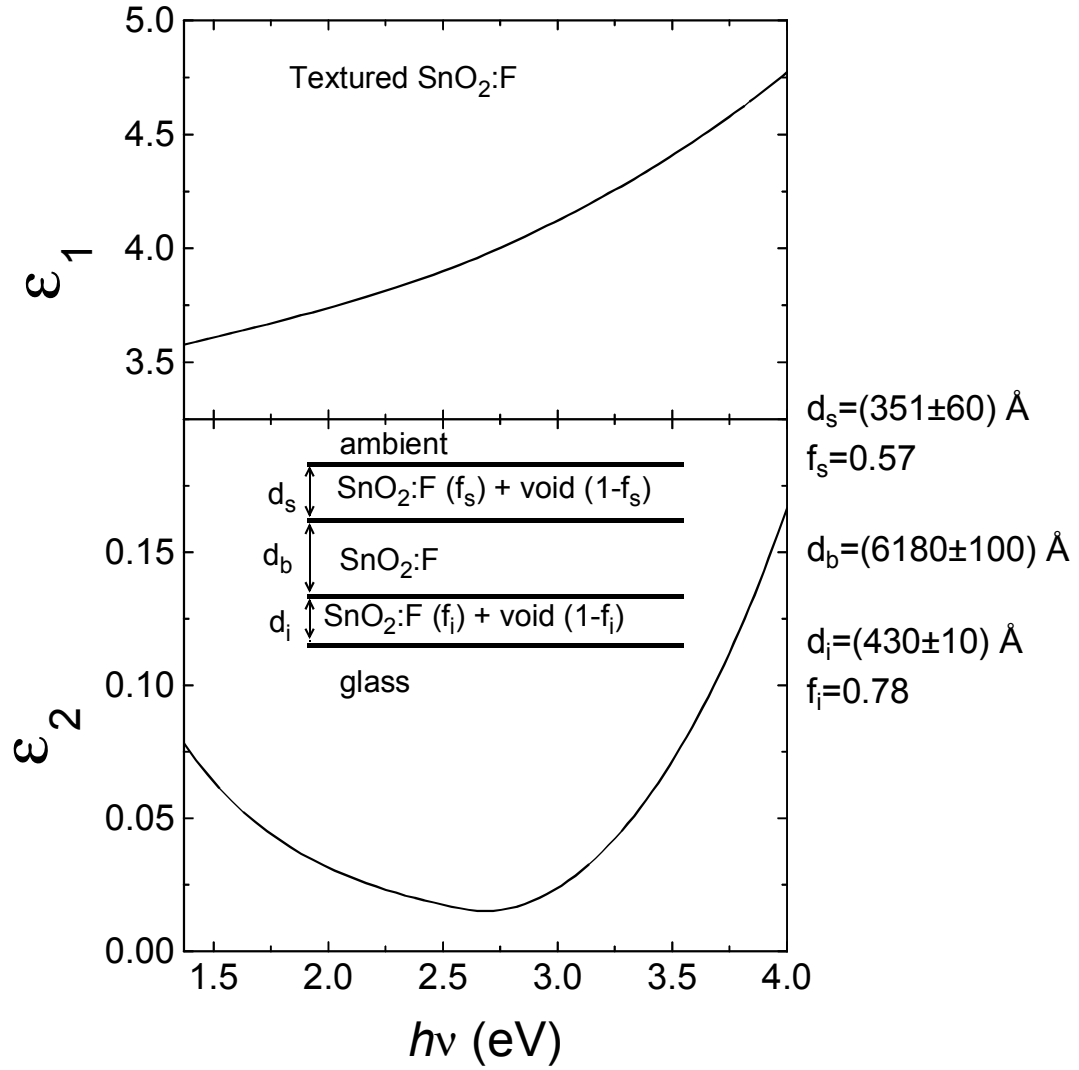


Figure IV.1.3 The best fit dielectric function for the bulk layer of Asahi U-type textured SnO₂ at 25°C using Tauc-Lorentz bound electron and Drude free electron contributions. The inset shows the microscopic structural model for the SnO₂, along with the best fit structural parameters (right).

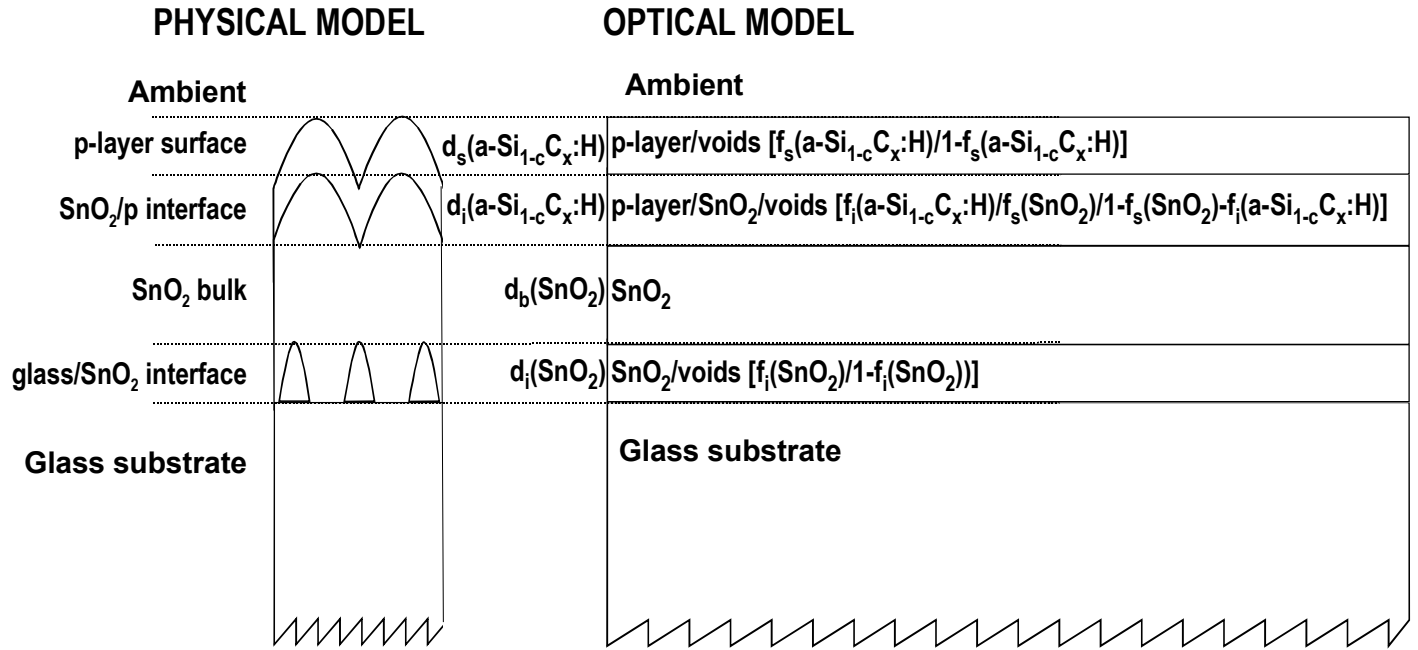


Figure IV.1.4 Schematic microscopic physical (left) and optical (right) models used in the analysis of (ψ, Δ) spectra for the growth of the $a\text{-Si}_{1-x}C_x\text{:H}$ p-layer of an $a\text{-Si:H}$ solar cell on textured SnO₂-coated glass. The parameters $d_s(a\text{-Si}_{1-x}C_x\text{:H})$ and $f_s(a\text{-Si}_{1-x}C_x\text{:H})$ are the thickness and material volume fraction for the p-type $a\text{-Si}_{1-x}C_x\text{:H}$ surface roughness layer that extends above the SnO₂ substrate layer; $d_i(a\text{-Si}_{1-x}C_x\text{:H})$ and $f_i(a\text{-Si}_{1-x}C_x\text{:H})$ are the thickness and p-layer volume fraction for the interface roughness layer between the SnO₂ and the p-layer; $d_i(\text{SnO}_2)$ and $f_i(\text{SnO}_2)$ are the thickness and material volume fraction for a low density SnO₂ layer at the interface to the glass substrate; $d_b(\text{SnO}_2)$ is the SnO₂ bulk layer thickness. All surface and interface roughness layers are assumed to be microscopic, meaning that the correlation lengths of the structure are less than the wavelength of the light.

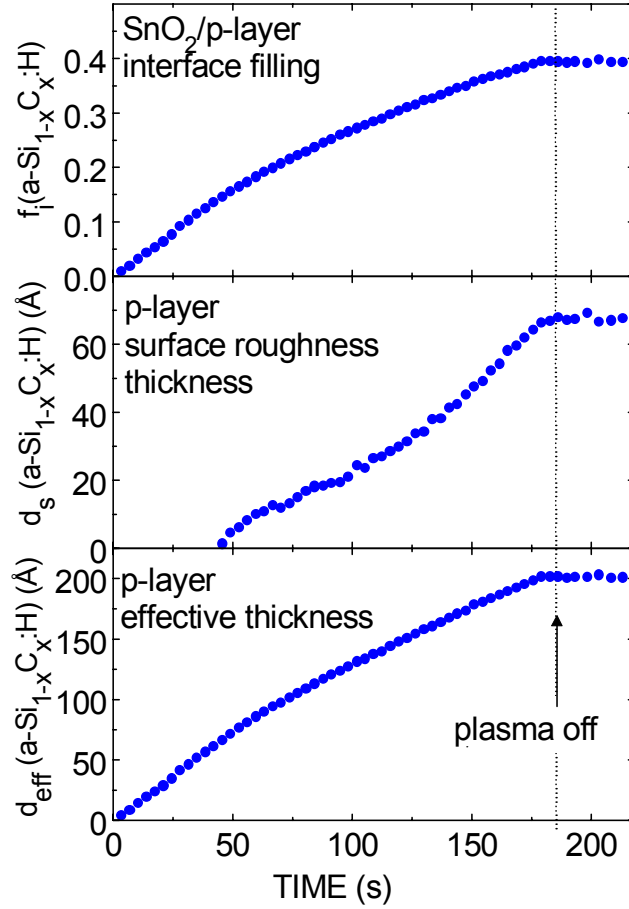


Figure IV.1.5 Evolution of the microstructural parameters for the growth of an $a\text{-Si}_{1-x}\text{C}_x\text{:H:B}$ p-layer on textured SnO_2 -coated glass. The parameter $d_s(a\text{-Si}_{1-x}\text{C}_x\text{:H:B})$ is the thickness of the p-type $a\text{-Si}_{1-x}\text{C}_x\text{:H}$ surface roughness layer that extends above the SnO_2 substrate layer. In this analysis the p-type $a\text{-Si}_{1-x}\text{C}_x\text{:H:B}$ volume fraction within this surface layer is given by $f_s(a\text{-Si}_{1-x}\text{C}_x\text{:H:B})=0.35$. The parameter $f_i(a\text{-Si}_{1-x}\text{C}_x\text{:H:B})$ is the p-type $a\text{-Si}_{1-x}\text{C}_x\text{:H}$ volume fraction filling the interface roughness layer between the SnO_2 and the p-layer. The thickness of this layer is given by $d_i(a\text{-Si}_{1-x}\text{C}_x\text{:H:B})=d_s(\text{SnO}_2)=450 \text{ \AA}$ as determined in an analysis of the starting SnO_2 substrate film. The parameter $d_{\text{eff}}(a\text{-Si}_{1-x}\text{C}_x\text{:H})$ is the effective thickness of the p-layer given by $d_{\text{eff}}=f_i d_i + f_s d_s$.

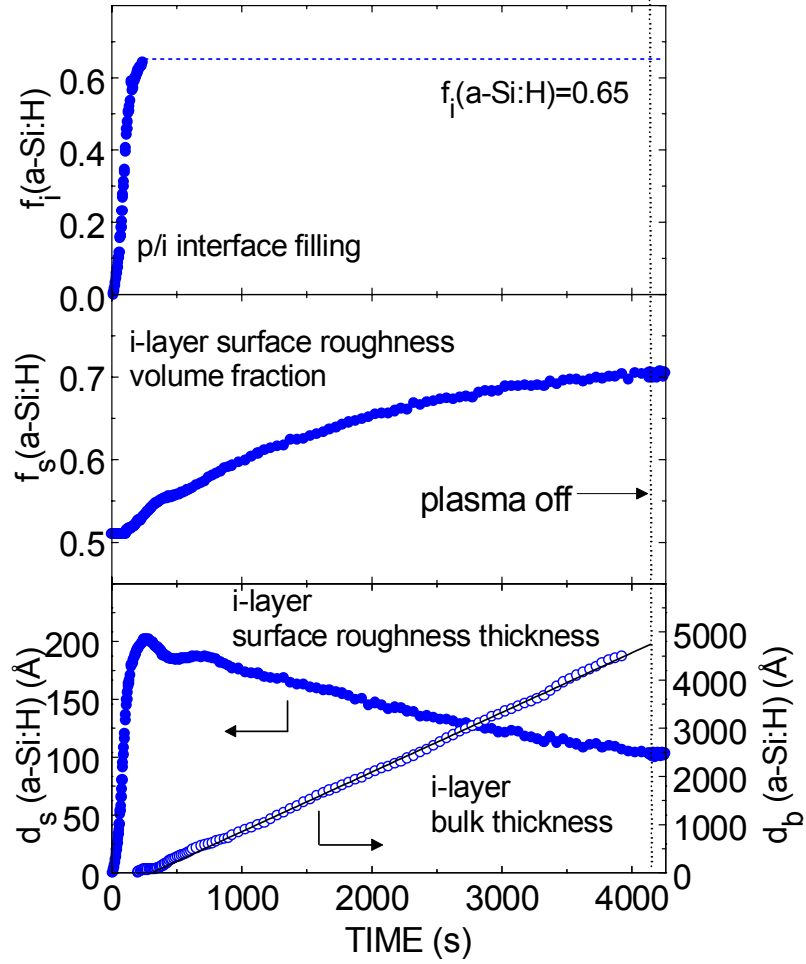


Figure IV.1.6 Evolution of the microstructural parameters for the growth of an a-Si:H i-layer on top of a glass/SnO₂/p-layer structure. The parameters $d_s(\text{a-Si:H})$ and $f_s(\text{a-Si:H})$ are the thickness and material volume fraction in the surface roughness on the a-Si:H i-layer. The parameter $f_i(\text{a-Si:H})$ is the a-Si:H i-layer volume fraction filling the interface roughness layer between the p and i layers, and $d_b(\text{a-Si:H})$ is the a-Si:H i-layer bulk thickness. Once the p/i interface roughness layer is established as a 0.35/0.65 volume fraction mixture of p-layer/i-layer materials, the bulk layer begins to form. In the bulk layer growth regime $f_i(\text{a-Si:H})$ is fixed at 0.65, representing a completely filled p/i interface roughness layer.

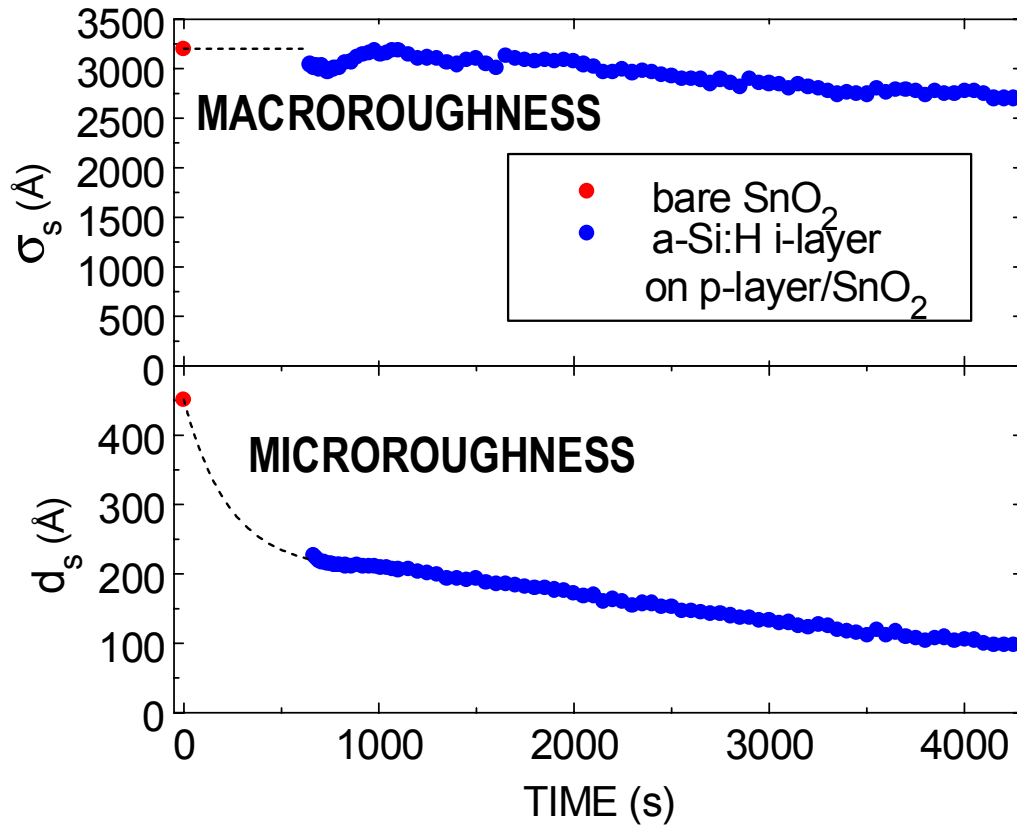


Figure IV.1.7 Evolution of the microscopic and macroscopic roughness layer thicknesses deduced in analyses of (ψ, Δ) and R , respectively, for the later stages of growth of the i-layer on the textured SnO₂/p-layer structure. The macroscopic roughness $\sigma_s(\text{a-Si:H})$ is defined as the FWHM of the Lorentzian distribution describing the a-Si:H surface profile in the scalar diffraction model. The microscopic roughness is defined by $d_s(\text{a-Si:H})$ that describes the thickness of the a-Si:H/void mixture in the effective medium theory. The points at $t=0$ designate the corresponding values for the uncoated SnO₂ surface.

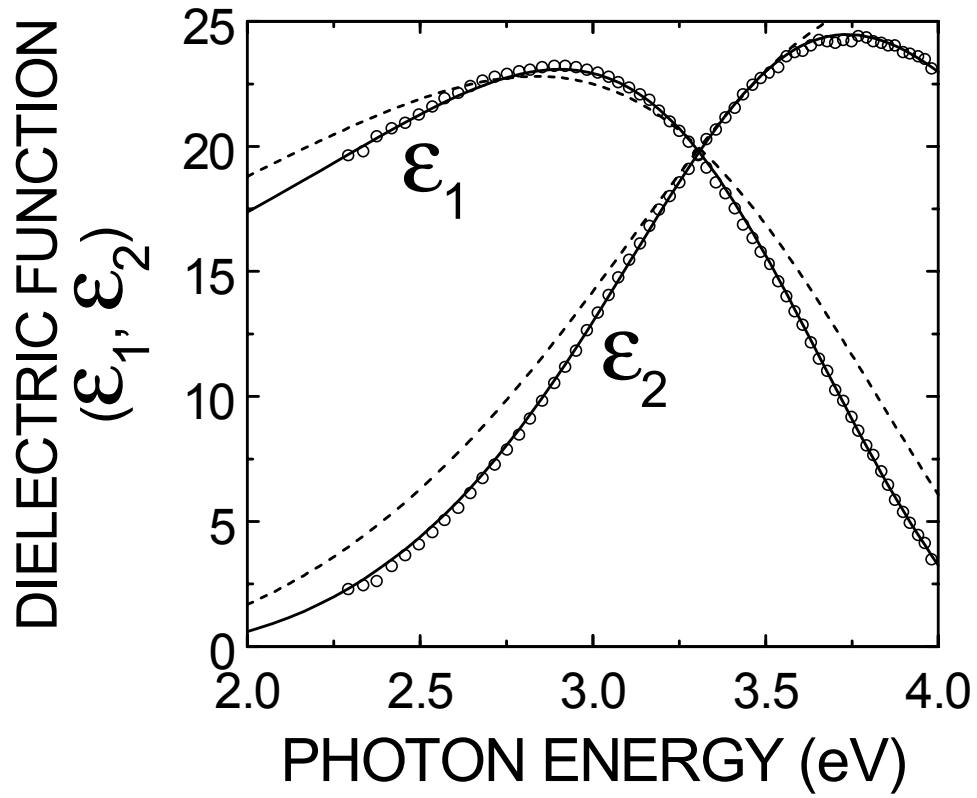


Figure IV.1.8 Dielectric function of the bulk a-Si:H i-layer on a textured SnO₂/p-layer structure obtained from the analysis of Fig. IV.1.6 at a thickness of 1985 Å (points). Also shown are the best fit Tauc-Lorentz models for the dielectric functions of i-layers incorporated into solar cells on textured SnO₂ (solid lines; fit to points) and specular SnO₂ (broken lines).

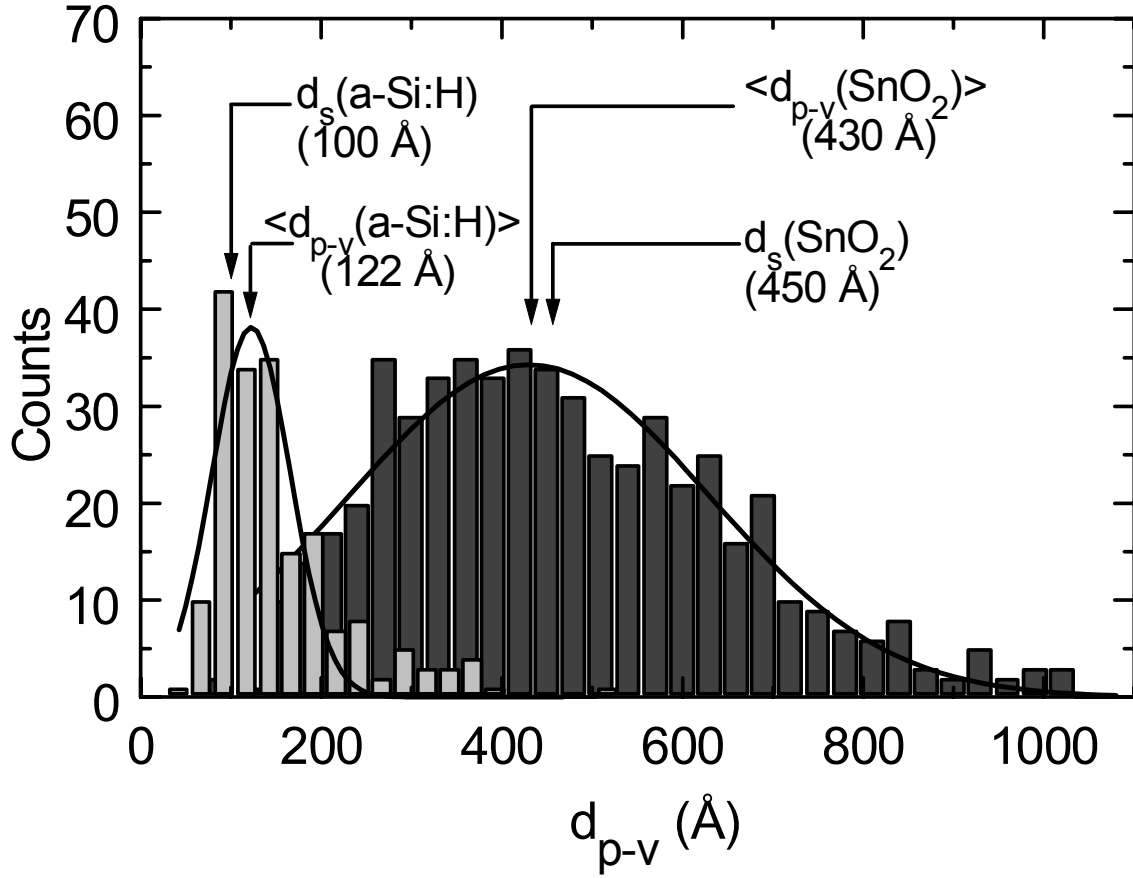


Figure IV.1.9 Distributions describing the maximum peak-to-valley excursions d_{p-v} within $0.1 \times 0.1 \mu\text{m}^2$ regions of $5 \times 5 \mu\text{m}^2$ AFM images for the uncoated textured SnO₂ surface (shaded bars) and for the completed textured a-Si:H solar cell surface (open bars). The solid lines depict fits of these distributions to Gaussian functions. The vertical lines show the average values $\langle d_{p-v} \rangle$ placed at the center of the Gaussian functions, in comparison with the d_s values deduced in the optical analysis of the microstructure.

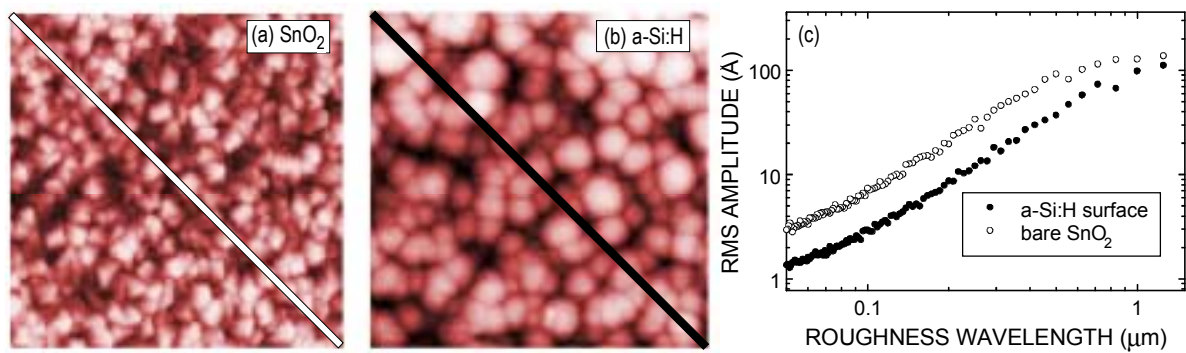


Figure IV.1.10 Atomic force microscopy images over $5 \times 5 \mu\text{m}^2$ areas for (a) the uncoated textured SnO_2 and (b) the completed textured a-Si:H solar cell. In part (c), one dimensional Fourier analyses along the diagonals of the images are shown. In these analyses, the root-mean-square amplitude is plotted as a function of the spatial frequency (or surface profile wavelength) for the two samples.

IV.2. Optical Modeling

Motivation and Overview

Analytical expressions that describe the optical functions, i.e., the real and imaginary parts of the dielectric function (or the index of refraction and extinction coefficient) versus wavelength (or photon energy), have important applications in amorphous and microcrystalline semiconductor science and technology [1]. First, in materials studies such expressions can be used to analyze optical data by least-squares regression and, in this way, extract useful parameters. The optical data of interest include transmittance, reflectance, and ellipsometric spectra, collected either ex situ or in real time, and the deduced parameters include the optical gap, oscillator, and broadening energies that provide information on composition, ordering, phase, and grain size [2]. This application was described in Sec. I.1. Second, such expressions constitute a database for the optical functions of the individual layer components of multilayer stacks, allowing one to simulate optical properties of complex multilayer devices. In this section, we suggest how the expressions can be used in optical modeling of multijunction solar cells

Experimental Details

In the modeling of the dielectric function spectra $\epsilon(E)=\epsilon_1(E)+i\epsilon_2(E)$ developed here, we apply expressions of the form $\epsilon_2(E) = \Theta(E - E_G)G(E)\{\sum_{i=1} L_i(E)\}$, where E_G and Θ designate the lowest energy optical gap and the unit step function, respectively, i.e., $\Theta(x)=0$ for $x<0$ and $\Theta(x)=1$ for $x\geq 0$. In addition, $G(E)$ describes $\epsilon_2(E)$ for $E\approx E_G$, whereas it approaches unity for $E\gg E_G$. Finally, $L_i(E)$ is a lineshape function associated with the i th above-bandgap transition. ϵ_1 can be expressed as $\epsilon_1(E)=\epsilon_{1\infty}+K\{\epsilon_2(E)\}$, where $\epsilon_{1\infty}$ accounts for possible high energy transitions not included in $\epsilon_2(E)$ ($\epsilon_{1\infty}\geq 1$) and K designates the Kramers-Kronig (K-K) integral applied to ϵ_2 .

Such an approach has been first developed by Jellison and Modine (JM) to model the dielectric functions of amorphous semiconductors [3]. In the JM approach, one Lorentz oscillator is used to simulate all above-gap transitions so that $N=1$ and $L_1(E)=A_1E_1\Gamma_1E/\{(E^2-E_1^2)^2+\Gamma_1^2E^2\}$, where (A_1, Γ_1, E_1) are amplitude, broadening, and resonance energies. In addition, $G(E)$ is given by $G(E)=G_{CM}(E)=(E-E_G)^2/E^2$, a function that approaches unity for $E \gg E_G$ and leads to a linear Tauc plot for $E \approx E_G$, based on the assumptions of parabolic bands and a constant momentum (CM) matrix element [4]. We have found that a similar approach can be applied to fit $\epsilon(E)$ for nc-Si:H and μ c-Si:H, with the exception that two oscillators L_i ($i=1,2$) with parameters (A_i, Γ_i, E_i) ($i=1,2$) are incorporated, representing the broadened E_1 and E_2 transitions for crystalline Si. Thus, a total of eight parameters (including E_G and $\epsilon_{1\infty}$) are needed to fit $\epsilon(E)$ for nc-Si:H and μ c-Si:H films.

Although the original single-oscillator approach applied by JM works reasonably well in fitting ϵ for the wider gap a-Si:H-based materials generated by H_2 -dilution and C-alloying, it works poorly for the narrow gap materials generated by Ge-alloying. Thus, a different approach must be applied to obtain a single expression for $\epsilon(E)$ applicable for optical modeling of the full range of potential multijunction solar cell components from a-Si_{1-x}Ge_x:H to a-Si_{1-x}C_x:H. As a result, we set $G(E)=G_{CD}(E)=(E-E_G)^2/\{E_p^2+(E-E_G)^2\}$, where $E_p \approx E_G$ is a variable demarcation energy. E_p separates the regime of $E \gg E_G$ where $G_{CD}(E) \approx 1$, promoting convergence of the K-K integral, and the regime of $E \approx E_G$ where $G_{CD}(E) \approx (E-E_G)^2$, leading to a linear Cody plot based on the assumptions of parabolic bands and a constant dipole (CD) matrix element. Thus, six parameters are needed to fit $\epsilon(E)$ for any amorphous alloy, one more parameter (E_p) than the original approach by JM.

In this study, dielectric functions measured ex situ at 25°C were obtained by combining dual-beam photoconductivity, transmission and reflection spectroscopy, and spectroscopic ellipsometry (SE) [5].

Results

Figure IV.2.1 (points) shows dielectric functions obtained ex situ for $\sim 1 \mu\text{m}$ thick $\text{a-Si}_{1-x}\text{Ge}_x\text{:H}$, a-Si:H , and $\text{a-Si}_{1-x}\text{C}_x\text{:H}$ films with E_{03} values (i.e., the energy at which the absorption coefficient α is 10^3 cm^{-1}) of 1.45, 1.72, and 1.88 eV, respectively. These films were prepared by dc plasma-enhanced chemical vapor deposition (PECVD) at Solarex (courtesy of G. Ganguly), for assessment as components of multijunction solar cells. The solid lines in Fig. IV.2.1 show best fits using the expressions $\epsilon_2 = \Theta G_{\text{CD}} L_1$ and $\epsilon_1 = 1 + K \{\epsilon_2\}$. By fixing $\epsilon_{\infty 1} = 1$, each of these fits yields five free parameters. The biased estimator of the mean square deviation designated χ^2 is given in Fig. IV.2.1 for the fits using the five-parameter CD and four-parameter CM approaches. Application of the five-parameter CM approach with $\epsilon_{1\infty}$ free yields $\epsilon_{1\infty} < 0$ for the $\text{a-Si}_{1-x}\text{Ge}_x\text{:H}$, and so is not considered physically valid. The comparisons of χ^2 in Fig. IV.2.1 show that an improvement is provided by the CD approach as would be expected based on previous work by Cody [4]. Figure IV.2.2 shows the four free parameters in the analysis plotted as a function of optical gap for a set of 0.5 to 2 μm thick samples having the largest bond-packing density (yielding an envelope of maximum A_1). The gap along the abscissa is obtained most accurately in a fit to the linear trend in $\epsilon_2^{1/2}$ versus E just above E_G . This latter approach for determining the gap yields the same energy within $\pm 0.02 \text{ eV}$ as E_{03} and as the Tauc approach (the latter with a linear extrapolation range of $3 \times 10^3 < \alpha < 3 \times 10^4 \text{ cm}^{-1}$) [5]. The solid lines in Fig. IV.2.2 provide continuous fits to the free parameters that allow the optical functions for high-density amorphous materials to be generated based on a single measure of the optical gap.

Figure IV.2.2(b) shows a minimum in ϵ_1 for PECVD a-Si:H when $E_G \approx 1.8 \text{ eV}$. Such material is prepared with a maximal H_2 -dilution level of $R = [\text{H}_2]/[\text{SiH}_4] = 10$, just prior to the onset of $\mu\text{c-Si:H}$ growth for a $0.5 \mu\text{m}$ thick film [6]. In general, ϵ_1 increases from this minimum if, as in Fig. IV.2.2(b) (i) R is reduced to span the range of gaps from 1.8 to 1.7 eV, (ii) Ge is incorporated to span the range from 1.7 to 1.4 eV, or (iii) C is incorporated to span the range from 1.8 to 2.3 eV. Based on such variations we suggest that ϵ_1 is affected by disorder induced by strained Si-Si bonds or by alloying, and the results are consistent with the interpretation of ϵ_1

as being inversely proportional to the lifetime for interband excitations [2]. This interpretation has been exploited to study the ordering for a-Si:H as a function of R, as described in Sec. I.1

Discussion

The parameterizations presented in Sec. 2 adopt the simplest possible approaches (i.e., with the minimum number of free parameters) while extracting useful physical information. These approaches have several limitations that can be addressed in future refinements. First, limitations in the optical function database for applications in solar cell modeling arise from the simplification that ϵ_2 is assumed to vanish below E_G . In order to generate absorbance data accurate to better than a few percent in optical simulations, however, an exponential absorption tail for $0 < E < E_G$ must be included in the model of $\epsilon_2(E)$ for the 50-200 nm thick amorphous i-layers of a-Si:H-based multijunction solar cells. Although such a refinement is not needed for the 20 nm doped μ c-Si:H layers used in such devices, it is in fact critical -- along with a more accurate parameterization in the bandgap region ($E \approx E_G$) -- for optical simulations of the very thick ($>1 \mu\text{m}$) μ c-Si:H i-layers used in "micromorph" cells [7]. In this case accurate parameterized models for $(n, \ln\alpha)$ rather than (ϵ_1, ϵ_2) appear necessary, where n is the index of refraction. Second, limitations arise from the use of Lorentz oscillators to describe all the critical point features in ϵ for crystalline films. The simple approach is suitable for μ c-Si:H, but for polycrystalline Si exhibiting narrower linewidths, additional parameters are needed to simulate the more complicated nature of the critical point transitions [2].

Concluding Remarks

Using simple Kramers-Kronig-consistent analytical expressions, we have fit dielectric functions obtained in ex situ and real time optical studies of amorphous Si and related alloys. The approach is a useful one since the resulting best fit parameters in the expressions provide insights into the nature of the component materials used in devices and can also support

simulations of the optical responses of multilayer stacks that incorporate these components. Working from this basis, future refinements for greater generality will be possible.

References

1. R.W. Collins, D.E. Aspnes, and E.A. Irene, eds., *Proceedings of the Second International Conference on Spectroscopic Ellipsometry*, (Elsevier, Amsterdam, 1998).
2. R.W. Collins and K. Vedam, in: *Encyclopedia of Applied Physics*, Vol. 12, (VCH, New York, 1995), p. 285.
3. G.E. Jellison, Jr., and F.A. Modine, *Appl. Phys. Lett.* **69**, 2137 (1996).
4. G.D. Cody, in: *Semiconductors and Semimetals*, Vol. 21B, (Academic, New York, 1984), p. 11.
5. R.M. Dawson, Y. Li, M. Gunes, D. Heller, S. Nag, R.W. Collins, C.R. Wronski, M. Bennett, and Y.M. Li, *Mater. Res. Soc. Symp. Proc.* **258**, 595 (1992).
6. J. Koh, Y. Lee, H. Fujiwara, C.R. Wronski, and R.W. Collins, *Appl. Phys. Lett.* **73**, 1526 (1998).
7. J. Meier, R. Fluckiger, H. Keppner, and A. Shah, *Appl. Phys. Lett.* **65**, 860 (1994).

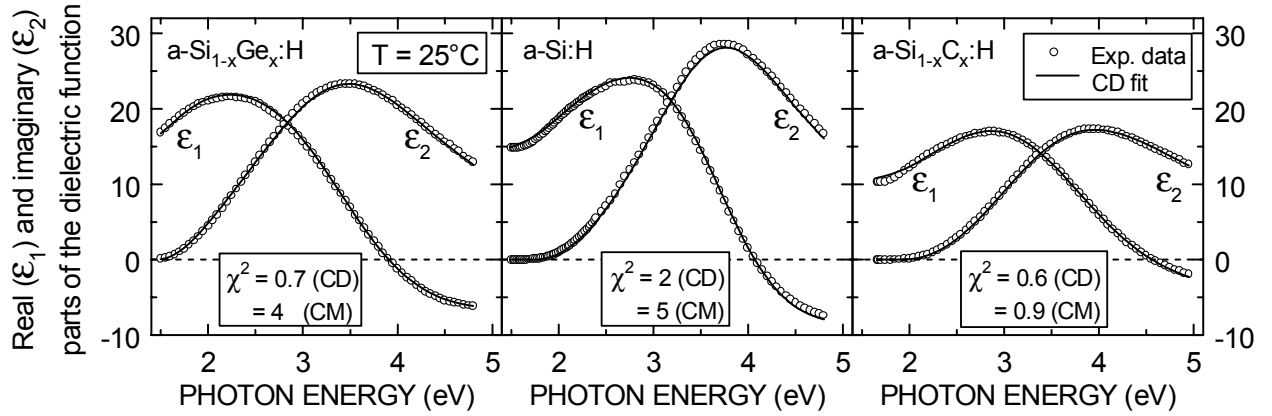


Figure IV.2.1 Dielectric functions measured ex situ at 25°C (points) for a-Si_{1-x}Ge_x:H, a-Si:H, and a-Si_{1-x}C_x:H along with best fits (lines) to an expression exhibiting near-gap behavior consistent with a constant dipole (CD) matrix element. χ^2 indicates the biased estimator of the mean square deviation between the data and best fit.

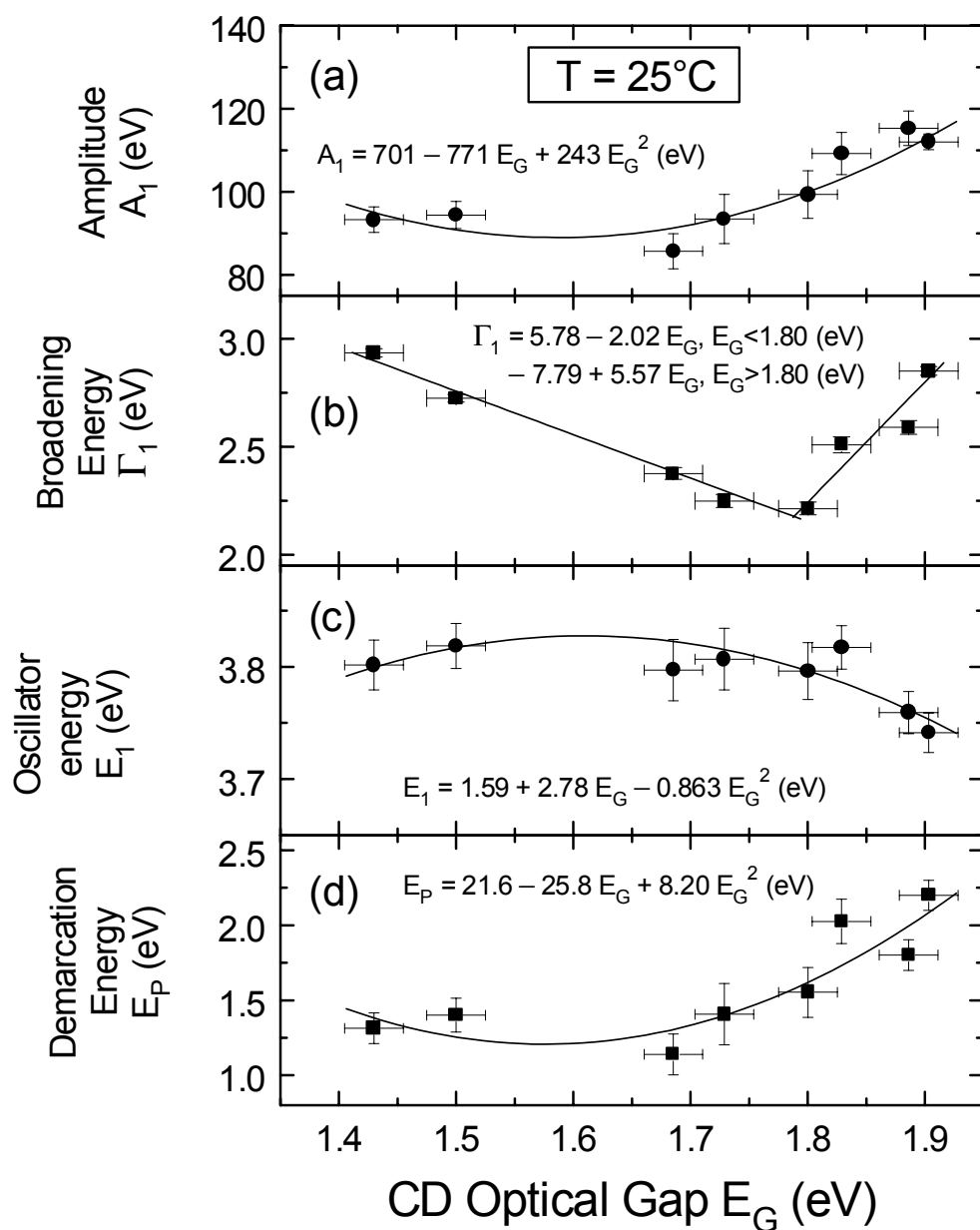


Figure IV.2.2 Free parameters in an expression that provides best fits to the dielectric functions measured ex situ at 25°C for a series of amorphous semiconductor films. These parameters are plotted versus the optical gap deduced assuming a constant dipole (CD) matrix element. The solid lines are fits to the data using the relationships shown.

IV.3. Tunnel Junction Formation

Motivation and Overview

The optimization of p/n and n/p tunnel junctions in amorphous silicon (a-Si:H) based n-i-p and p-i-n multijunction solar cells poses a considerable challenge when very thin (~ 100 Å), microcrystalline silicon ($\mu\text{c-Si:H}$) doped layers are used for high conductivity and reduced optical absorption [1]. There are two key steps in tunnel junction formation. For the case of the p/n junction of an n-i-p multijunction solar cell, for example, one must first ensure immediate, high-density nucleation of a single-phase $\mu\text{c-Si:H}$ p-layer on the underlying i-layer. One must then overdeposit a $\mu\text{c-Si:H}$ n-layer to form a contact having characteristics such that junction recombination is favored over trapping within the doped layers [2]. Rath et al. have found that for high current-generating component cells in the p-i-n configuration, an optimized tunnel junction consists of ~ 200 Å $\mu\text{c-Si:H}$ n and p layers with an ultra-thin intervening oxide layer at the junction [2]. They have proposed that the low mobility gap of the $\mu\text{c-Si:H}$ and the high defect density at the oxide junction are critical to obtaining high recombination rates. Although recent studies have characterized the nucleation and growth of intrinsic, p, and n type $\mu\text{c-Si:H}$ on a-Si:H i-layers [3-7], few studies have characterized the deposition of $\mu\text{c-Si:H}$ layers on underlying $\mu\text{c-Si:H}$ either with plasma termination or with intervening interface layers. In this Task, we have applied real time spectroscopic ellipsometry (RTSE) to obtain insights into of $\mu\text{c-Si:H}$ p/n interface formation.

Experimental Details

In fabricating the $\mu\text{c-Si:H}$ p/n tunnel junctions, the substrate temperature during all processing was 200°C . The underlying a-Si:H i-layer was prepared first using rf plasma-enhanced chemical vapor deposition (PECVD) with pure SiH_4 (i.e., with $R=[\text{H}_2]/[\text{SiH}_4]=0$), a flow rate of 5 sccm, a plasma power of 70 mW/cm^2 , and a pressure of 0.07 Torr. The n-layer growth was performed on two different types of p-layers [7]. For both p-layers, a 150 s H_2 -

plasma pretreatment of the underlying a-Si:H i-layer was applied, using a H₂ flow rate of 200 sccm, a power of 700 mW/cm², and a pressure of 0.9 Torr. In one case, the p-layer was prepared with R=200, a trimethyl boron doping level of $D=[B(CH_3)_3]/[SiH_4]=0.01$, a power of 230 mW/cm², and a total pressure of ~0.9 Torr. In the other case, the p-layer was prepared with R=200, a boron trifluoride doping level of $D=[BF_3]/[SiH_4]=0.05$, a power of 700 mW/cm², and a pressure of ~0.9 Torr. Both sets of conditions led to immediate nucleation of single-phase nanocrystalline silicon films which coalesced at thicknesses as low as ~25-40 Å [7]. In addition, these p-layers exhibited well-defined absorption onsets near 2.4 eV, characteristic of the presence of nanocrystals, and a low relative void volume fraction. In Sec. III.2, the range of gas phase doping level D for optimum structure was found to be narrow for B(CH₃)₃, but very broad for BF₃. We present results for these latter films owing to the relative insensitivity to the deposition process.

For the tunnel junctions, two different n-layer conditions using R=50 (at 0.5 Torr pressure) and R=200 (at 0.9 Torr) were explored in this Task. The fixed conditions included a doping level of $D=[PH_3]/[SiH_4]=0.012$ and a plasma power of 700 mW/cm². The latter conditions were obtained in optimization studies using H₂-plasma-treated a-Si:H i-layer substrates as described in the next section. Amorphous n-layers 50 Å thick used at the tunnel junction interface were prepared using R=0, D=0.02, a plasma power of 70 mW/cm², and a pressure of 0.1 Torr. Finally, ultrathin oxides 10 Å thick used at the tunnel junction interface were obtained by exposing the completed p-layer to a pure O₂ plasma for 2 min using a flow rate of 5 sccm, a power of 70 mW/cm², and a pressure of 0.09 Torr.

RTSE measurements were performed using a rotating compensator multichannel ellipsometer [8]. Spectra were collected during p-layer, interface layer (if used), and n-layer growth with acquisition and repetition times of 1 and 5 s, respectively. Realistic multilayer models were employed to analyze the RTSE data that incorporate the effects of substrate modification, substrate surface roughness filling, nucleation, and growth [3].

Results

The initial experiments performed in this study involved optimization of n-layers on a-Si:H

i-layers for single-phase, high-density, n-type $\mu\text{c-Si:H}$. Both H_2 -plasma treated and untreated i-layer substrates were used and n-layers were deposited with a range of R values (50-200), different doping levels ($D=0.006, 0.012$), and different plasma power levels ($P=230, 700 \text{ mW/cm}^2$). Figure IV.3.1 shows results for the change in surface roughness layer thickness Δd_s versus bulk layer thickness d_b for three n-layers prepared on H_2 -plasma treated a-Si:H i-layers at different R with the other parameters held constant ($D=0.006, P=700 \text{ mW/cm}^2$). Because the initial roughness layer thickness depends on the deposition history of the underlying substrate, it is subtracted from the data. For $R=50$ and 100 , the relatively stable surface with gradual smoothing in the initial stages of growth is attributed in this case to conformal coverage of the i-layer by a-Si:H:P. The abrupt roughening transitions after 75 \AA for $R=50$ and 40 \AA for $R=100$ are consistent with the development of nanocrystals which then propagate throughout the film with increasing thickness d_b [9]. The behavior for $R=200$ is the opposite; in the early stages of growth, d_s gradually increases and then decreases with increasing d_b . This behavior is characteristic of immediate nucleation of nanocrystals on the i-layer. The optical properties of the n-layers obtained in the different stages of growth also support such interpretations of Fig. IV.3.1. Figure IV.3.2 shows the imaginary parts of the dielectric functions ϵ_2 for the films of Fig. IV.3.1 with $R=50$ and 200 , measured at thicknesses of 130 \AA . Both reveal the characteristics of nanocrystalline Si; however, for $R=200$ the E_1 and E_2 crystalline Si features near 3.4 eV and 4.2 eV are more strongly developed and the amplitude is significantly larger. These characteristics indicate a larger grain size and a higher-density for the $R=200$ film. To summarize Figs. IV.3.1 and 2, it is suggested that $R=200$ is optimum for $\mu\text{c-Si:H}$ n-layer growth on an a-Si:H i-layer. Using a similar analysis strategy, the power level of 700 mW/cm^2 was found to be optimum, whereas the other deposition parameters explored here, including substrate treatment and doping level, exert weaker influences on the growth process.

Figure IV.3.3(a) shows the microstructural evolution including d_b and d_s as a function of time for the growth of the optimum $R=200$ $\mu\text{c-Si:H}$ n-layer on the H_2 -plasma-treated i-layer from Fig. IV.3.1. Also shown are the results (b-d) for the growth of three n-layers under identical conditions as in (a), but for different tunnel junction interfaces: (b) 50 Å a-Si:H:P n-layer at the junction interface; (c) 10 Å SiO_2 layer at the interface; and (d) no interface layer (i.e., growth directly on the top of the $\mu\text{c-Si:H}$ p-layer). Analyses of the optical properties show that all n-layers in Fig. IV.3.3 grow in the crystalline phase from the start. The results for n-layer growth on the a-Si:H:P interface in the tunnel junction [Fig. IV.3.3(b)] show similarities to those for n-layer growth on the i-layer [Fig. IV.3.3(a)]. This behavior is expected since both substrate films are amorphous Si. For both depositions of Figs. IV.3.3(a-b), nanocrystal nucleation and interface roughness filling occur initially over a period of 2-3 min with d_s increasing to 40 Å before nuclei coalescence and surface smoothening occur. In both cases, there is an initial slow bulk layer growth period attributed to simultaneous substrate etching. This effect is larger for the untreated a-Si:H:P interface layer in comparison with the H_2 -plasma treated a-Si:H i-layer. For n-layer growth on the SiO_2 interface layer in Fig. IV.3.3(c), nanocrystal nucleation and interface roughness filling occur over a longer period (4 min) with d_s increasing to 50 Å before bulk layer growth. In this case, the bulk layer induction period is absent, indicating that the SiO_2 layer promotes nanocrystal nucleation while arresting substrate etching. For n-layer growth directly on the p-layer without an interface layer in Fig. IV.3.3(d), the structural evolution is characteristic of interface roughness filling *without renucleation*. This is indicated by the constant value of d_s after interface filling (0-1 min), and the very short period before linear bulk film growth occurs (1 min) compared to the two cases (b-c) in which renucleation occurs (3-4 min).

The dielectric functions of these films also exhibit clear trends, as shown by the spectra for ϵ_2 in Figs. IV.3, 4, and 5. The n-layers deposited on the H_2 -plasma treated a-Si:H i-layer [broken line in Fig. IV.3.4] and the a-Si:H:P interface layer of the tunnel junction [broken line in Fig. IV.3.5] reveal results typical of a high density nanocrystalline structure with sharp

absorption onsets at 2.4-2.5 eV [7]. In contrast, the n-layers deposited directly on the $\mu\text{c-Si:H}$ p-layer [solid line in Fig. IV.3.4] and on the SiO_2 interface layer [solid line in Fig. IV.3.5] reveal results typical of a lower-density but larger-grained $\mu\text{c-Si:H}$ structure, with an absorption tail increasing gradually with increasing energy throughout the visible as in bulk crystalline Si. We suggest that the ~ 10 vol.% higher void fraction for the n-layer deposited directly on the p-layer compared with the n-layer deposited on the H_2 -plasma treated i-layer (see Fig. IV.3.4) is related to the development of the larger grains in the n-layer continuously from grains in the p-layer. The etching that occurs at $R=200$ leaves significant void structures in the grain boundary regions of this larger-grained film. The voids can be eliminated by reducing R . Although a value of $R=50$ for the n-layer leads to an initial 75 Å amorphous layer when deposition occurs on the H_2 -plasma treated i-layer, this lower dilution level also leads to continuous grain growth across the tunnel junction when deposition occurs directly on the $\mu\text{c-Si:H}$ p-layer (without an interface layer). The structural evolution for $R=50$ in this latter case is almost identical to that for $R=200$ in Fig. IV.3.3(d), except that the interface filling period is now one-half as long (~ 0.5 min), and the bulk layer growth rate is more than twice as fast (1.25 Å/s). Figure IV.3.6 shows the improvement in ϵ_2 that occurs from $R=200$ to $R=50$ for the two n-layers deposited directly on the $\mu\text{c-Si:H}$ p-layers. These results should be compared with those in Fig. IV.3.2, in which the substrate is a H_2 -plasma treated a-Si:H i-layer, and the reverse trend occurs from $R=200$ to $R=50$. Based on the results in Figs. IV.3.2 and 6, we conclude that optimization studies of $\mu\text{c-Si:H}$ layers for tunnel junction components must be made in the tunnel junction configuration. These results also lead to a general suggestion that although very high R is required for optimum nucleation of nanocrystals on an a-Si:H i-layer, once these nanocrystals form, a much lower R value can be used to propagate a higher-density, larger-grained $\mu\text{c-Si:H}$ structure at higher rates.

Discussion

A key issue raised in this Task is the substrate dependence that must be considered in the optimization of thin layers, particularly when high H_2 -dilution is used. In order to obtain insights

into such effects, we consider the evolutionary phase diagram for the growth of a-Si:H and $\mu\text{c-Si:H}$ versus bulk layer thickness d_b and H_2 -dilution ratio R . Figure IV.3.7 shows such a phase diagram for n-type Si films prepared on both H_2 -plasma treated (solid points on solid line phase boundary) and untreated a-Si:H i-layers (open points). Conditions for growth include $T=200^\circ\text{C}$, $D=0.006\text{--}0.012$, and high power (700 mW/cm^2). In this case, there is no significant effect of the H_2 -plasma treatment of the a-Si:H i-layer substrate in shifting the phase boundary. In addition, the phase boundary for the n-layers with $50 < R < 200$ is similar to that for undoped Si depositions at low power (compare Figs. IV.3.7 with Fig. I.1.2). It should be noted that in contrast to n-type doping with PH_3 , p-type doping with $\text{B}(\text{CH}_3)_3$ generates a large shift in the phase boundary to higher R such that a film prepared with $R=200$ on an untreated a-Si:H i-layer cannot initially nucleate in the form of a crystalline film and grows as an amorphous film to a thickness of 120 \AA (open square in Fig. IV.3.7). The lower limit of the phase boundary for p-layers doped using $\text{B}(\text{CH}_3)_3$ is shown in Fig. IV.3.7 as the dotted line. By performing a H_2 -plasma treatment of the underlying a-Si:H i-layer, however, the phase boundary for these p-layers can be shifted to much lower R (close to the boundary for the n-layer), apparently owing to the role of the H_2 -plasma in generating nanocrystals at the i-layer surface [7]. For the n-layers, direct deposition on the $\mu\text{c-Si:H}$ p-layers also leads to a boundary at very low R (as in Fig. I.1.2) for a similar reason; namely, once the crystallites form, the high value of R is not needed to sustain their growth. This is shown most clearly in the phase diagram of Fig. I.1.2 in which $\mu\text{c-Si:H}$ growth at $R=10$ can be sustained for a $\mu\text{c-Si:H}$ p-layer substrate film.

Summary

The preparation of fully $\mu\text{c-Si:H}$ p/n tunnel junctions for multijunction n-i-p solar cells has been studied using RTSE. In the initial studies, p and n layer recipes have been used based on optimized depositions with $R=[\text{H}_2]/[\text{SiH}_4]=200$ on a-Si:H i-layer substrates (e.g., those used for single junction n-i-p and p-i-n solar cells). For the $\mu\text{c-Si:H}$ n-layer depositions on $\mu\text{c-Si:H}$ p-layers, the role of different interface layers has been studied. We have found that for a thin a-

Si:H:P n-type interface layer at the tunnel junction, n-layer growth follows a very similar pattern to that on an a-Si:H i-layer; namely, crystallite nucleation is immediate and leads to a single-phase, high-density nanocrystalline n-layer after 100 Å. In contrast for an ultrathin SiO₂ interface layer, nucleation occurs at somewhat lower density and leads to a larger-grained μc-Si:H n-layer with a higher volume fraction of voids. For n-layer deposition directly on the μc-Si:H p-layer without an interface layer, renucleation does not occur and grain growth is continuous across the interface. The resulting larger grain size in this latter case is also accompanied by a larger void volume fraction. Surprisingly, the final microstructure of the n-layer is similar for no interface and for the ultrathin SiO₂ interface layer. This observation is a testament to the ability of ultrathin (10 Å) SiO₂ layers to nucleate large grain-size μc-Si:H immediately.

For the n-layer deposited on the p-layer to form a tunnel junction with no discontinuity at the interface, improved microstructure can be obtained by deviating from the conditions found to be best for growth on a-Si:H i-layers. It is found that when the H₂-dilution ratio is decreased from R=200 (which is found to be optimum for initial growth on an a-Si:H i-layer) to R=50, μc-Si:H growth from the p to the n-layer remains continuous, but the resulting n-layer shows a large grain size *and* a dense structure. Presumably this behavior is due to a reduction in the etching that occurs at high R. These results for p/n tunnel junctions in turn suggest a new approach for the deposition of improved single μc-Si:H doped layers on i-layers. In this approach the value of R is reduced after 50 Å has been deposited. In this way, the deposition process is maintained closer to the a-Si:H→μc-Si:H phase boundary, but on the μc side versus thickness, in order to avoid excessive etching that occurs at higher R and to maintain higher deposition rates.

References

1. S. Guha, J. Yang, P. Nath, and M. Hack, Appl. Phys. Lett. **49**, 218 (1986).
2. J.K. Rath, F. Rubinelli, and R.E.I. Schropp, J. Non-Cryst. Solids **227-230**, 1282 (1998).

3. J. Koh, H. Fujiwara, C.R. Wronski, and R.W. Collins, Sol. Energy Mater. Sol. Cells **49**, 135 (1997).
4. P. Pernet, M. Goetz, H. Keppner, and A. Shah, Mater. Res. Soc. Symp. Proc. **452**, 889 (1997).
5. L.L. Smith, W.W. Read, C.S. Yang, E. Srinivasan, C.H. Courtney, H.H. Lamb, and G.N. Parsons, J. Vac. Sci. Technol. A **16**, 1316 (1998).
6. P. Roca i Cabarrocas and S. Hamma, Thin Solid Films **337**, 23 (1999).
7. J. Koh, H. Fujiwara, R. Koval, C.R. Wronski, and R.W. Collins, J. Appl. Phys. **85**, 4141 (1999).
8. J. Lee, P.I. Rovira, I. An, and R.W. Collins, Rev. Sci. Instrum. **69**, 1800 (1998).

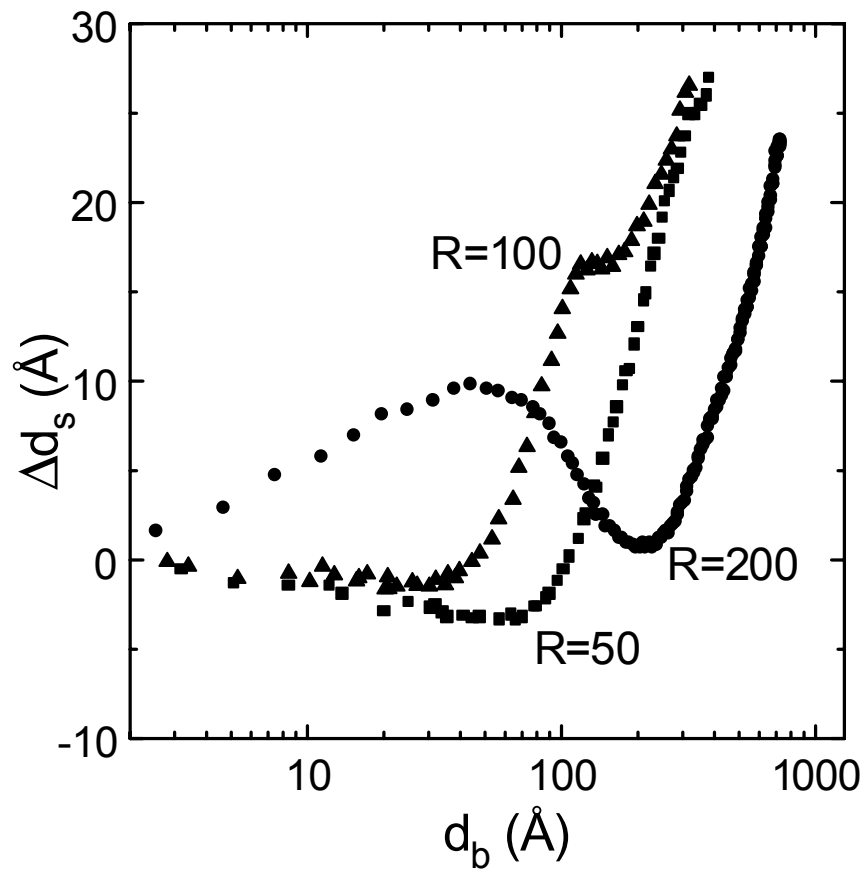


Figure IV.3.1 Change in the surface roughness layer thickness versus bulk layer thickness for n-layers prepared on H₂-plasma treated a-Si:H i-layers at different R values. Other deposition parameters are held constant at the values shown.

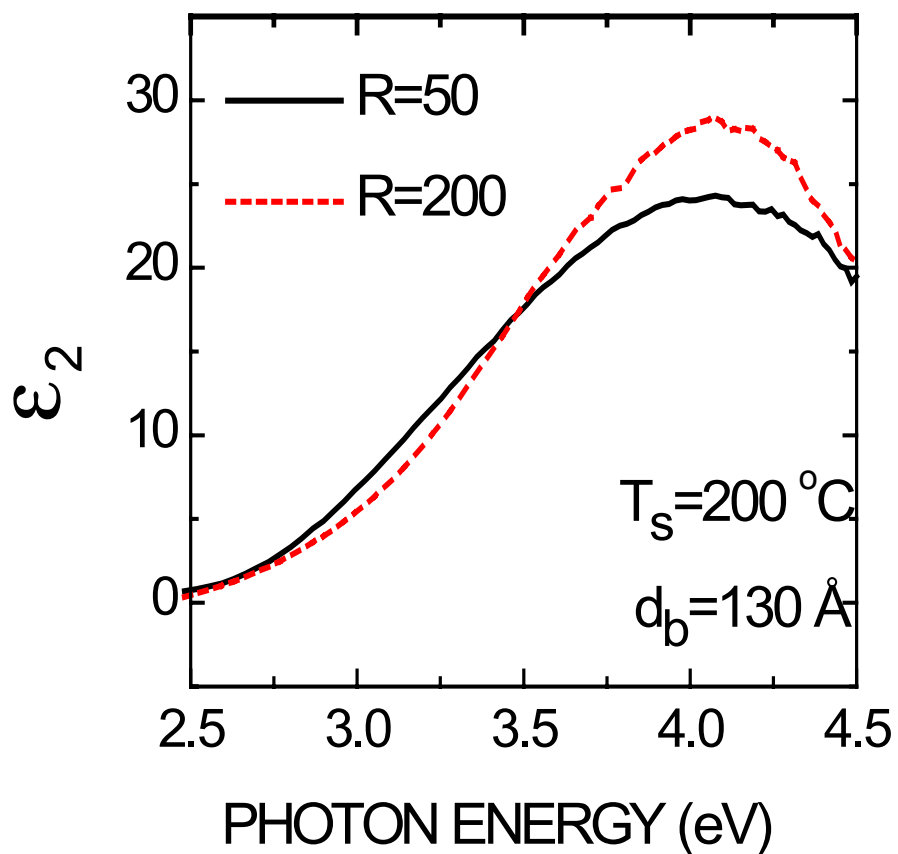


Figure IV.3.2 Imaginary parts of the dielectric functions of the nanocrystalline n-layers of Fig. IV.3.1 prepared on H_2 -plasma treated a-Si:H i-layers with $R=50$ (solid line) and 200 (broken line), measured at a thickness of 130 \AA and a sample temperature of 200°C .

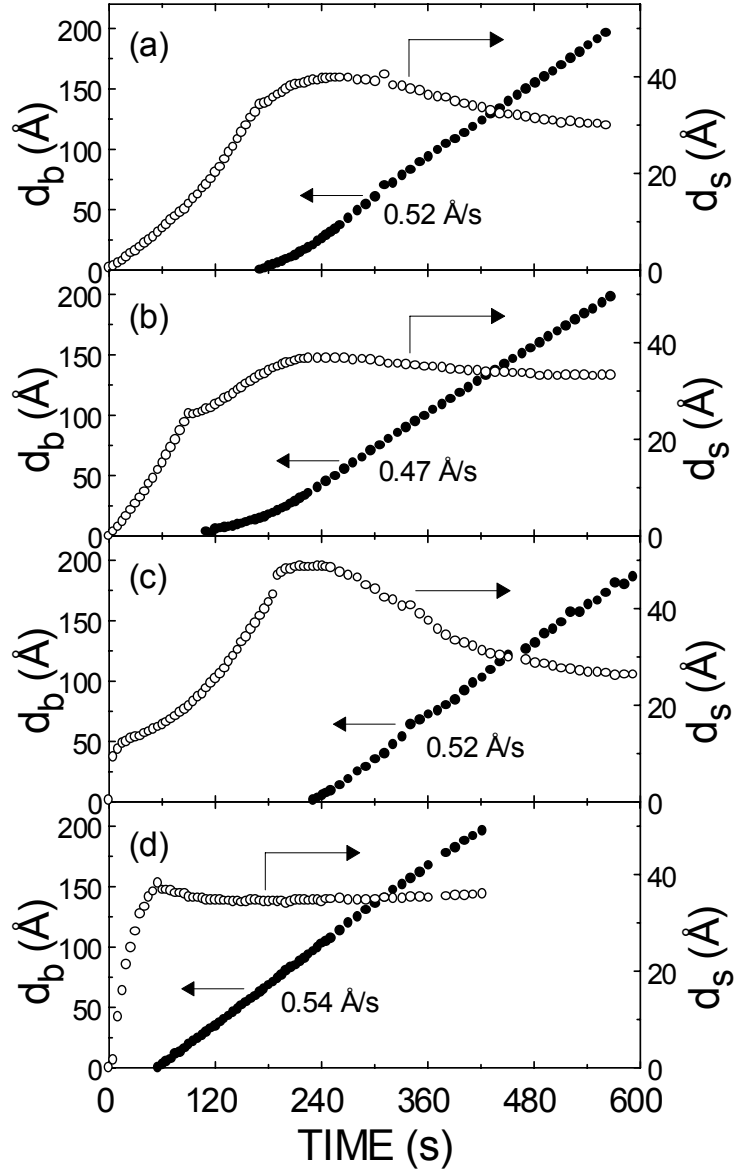


Figure IV.3.3 Microstructural evolution including surface roughness (d_s) and bulk layer (d_b) thicknesses vs. time for the growth of (a) a nanocrystalline n-layer with $R=200$ on a H_2 -plasma-treated a-Si:H i-layer (deposition of Fig. IV.3.1). Also shown (b-d) are the results for the growth of three n-layers under identical conditions as (a), but for different tunnel junction structures: (b) 50 Å a-Si:H:P n-layer at the tunnel junction interface; (c) 12 Å SiO_2 layer at the interface; and (d) no interface layer (i.e., growth directly on the μc -Si:H p-layer).

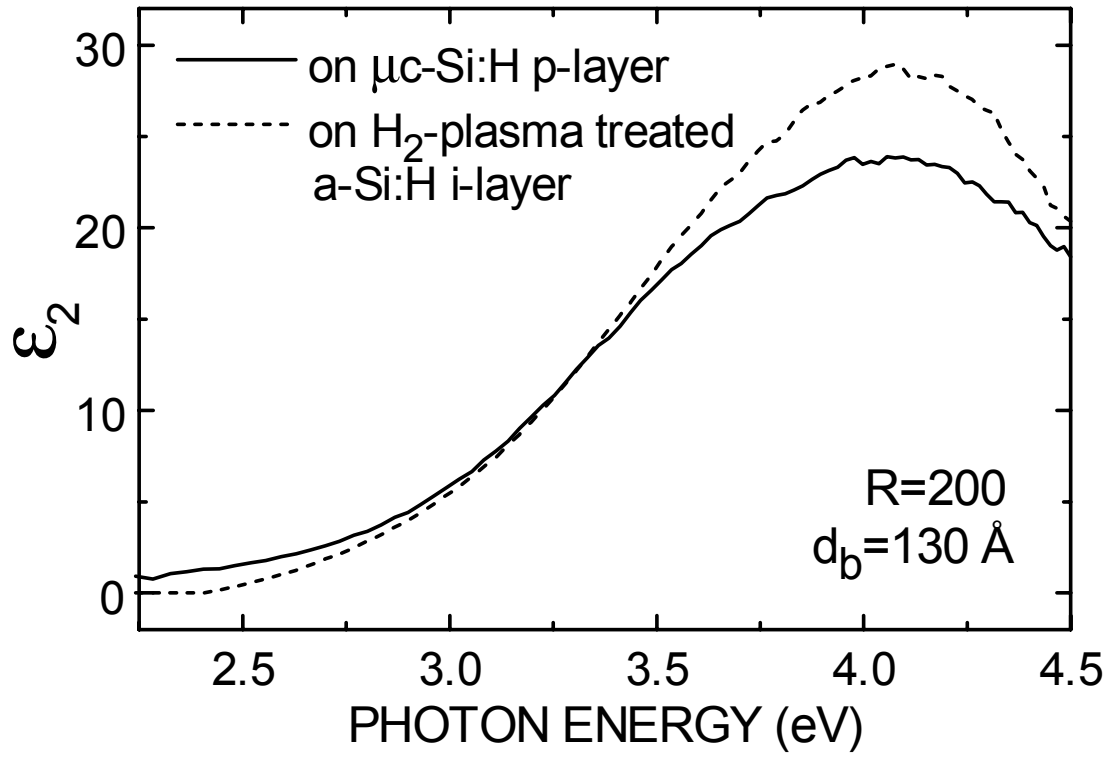


Figure IV.3.4 Imaginary parts of the dielectric functions at 200°C for the identically-prepared n-layers of Figs. IV.3.3(a) and (d), i.e., the n-layer deposited on the H_2 -plasma treated i-layer (broken line) and the n-layer deposited directly on the $\mu\text{c-Si:H}$ p-layer to form the tunnel junction (solid line). The bulk n-layer thickness for these measurements is 130 Å.

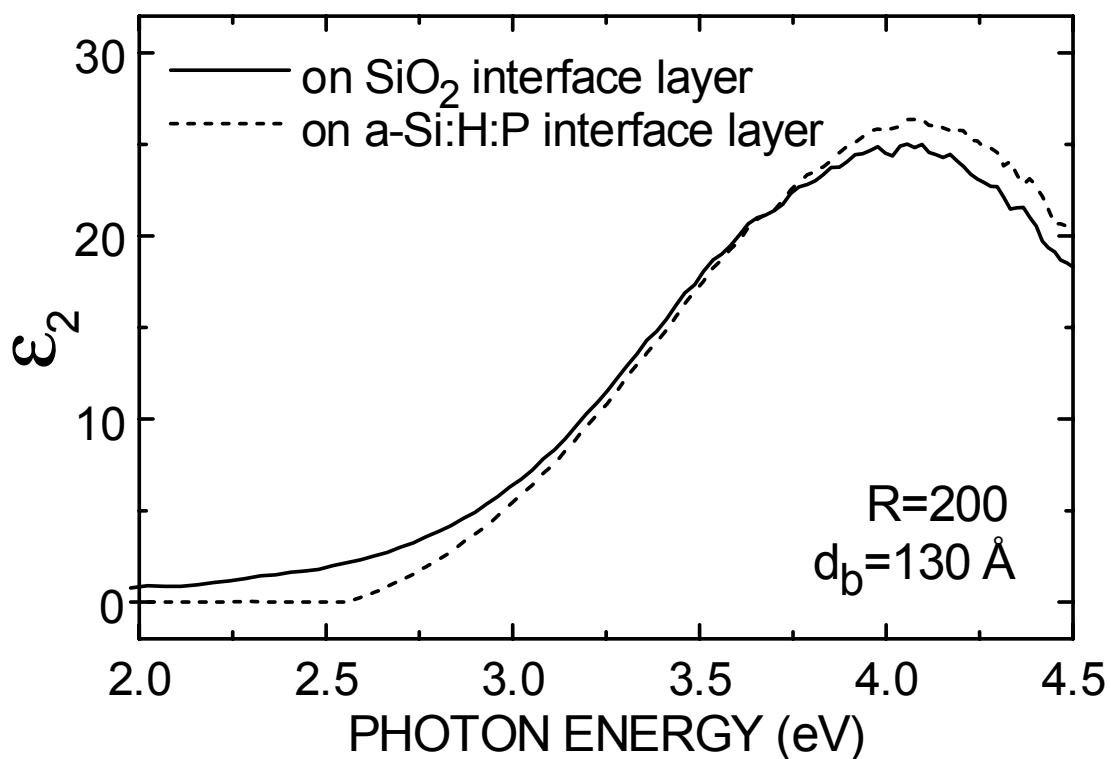


Figure IV.3.5 Imaginary parts of the dielectric functions at 200°C for the identically-prepared n-layers of Figs. IV.3.3(b) and (c), i.e., the n-layer deposited on the a-Si:H:P interface layer of the tunnel junction (broken line) and the n-layer deposited on the SiO_2 interface layer of the tunnel junction (solid line). The bulk n-layer thickness for these measurements is 130 Å.

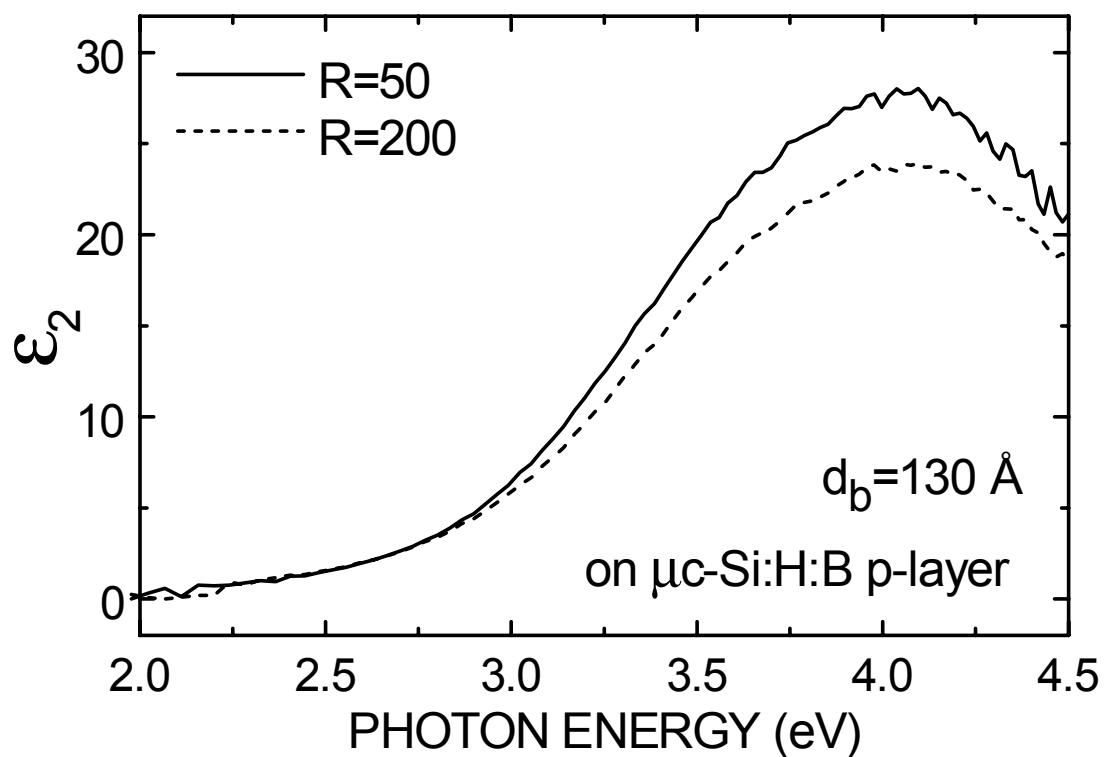


Figure IV.3.6 Imaginary parts of the dielectric functions of n-type $\mu\text{c-Si:H}$ films prepared with $R=50$ (solid line) and 200 (broken line) directly on $\mu\text{c-Si:H}$ p-layers to form the tunnel junctions, measured at a thickness of 130 \AA and a sample temperature of 200°C .

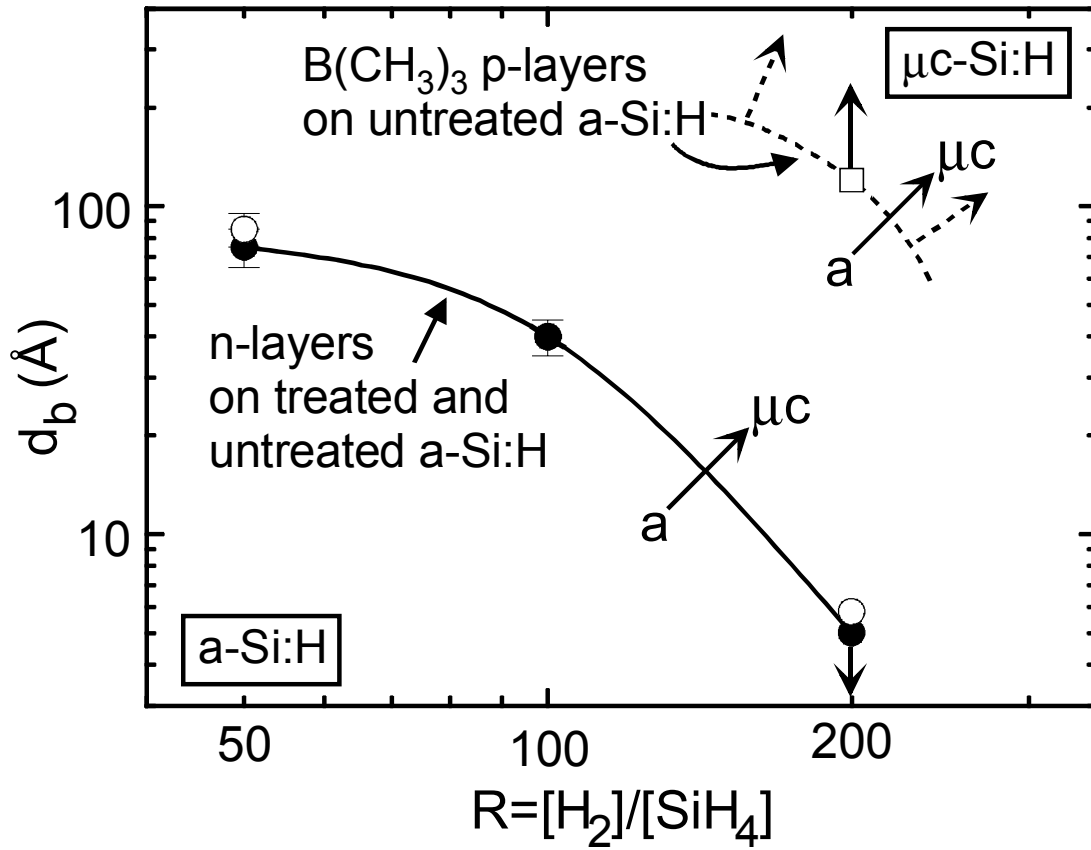


Figure IV.3.7 Evolutionary phase diagram for n-type Si films prepared using PH_3 doping gas on both H_2 -plasma treated (solid points on solid line phase boundary) and untreated (open points) a-Si:H i-layers. Also shown is the estimated lower limit of the phase boundary for p-layers prepared from $B(CH_3)_3$ on untreated a-Si:H i-layers (open square, dotted line).

APPENDIX I

Two USSC samples were characterized: USSC9762 with low H₂ dilution and USSC9765 with high H₂ dilution. Both were deposited at 300 °C on 7059 glass with 1μm thickness. Summary of the characterization results is presented below.

T&R measurements were carried out on both samples and results of the transmission spectra are as shown in Fig. A.1 with the optical absorption (α) in the inset figure. Cody gap E_{cd} is 1.75 eV (Tauc gap 1.80 eV) for the low dilution sample, which is similar to that of the PSU diluted R=10 film (E_{cd} 1.76 eV). In the case of the high dilution sample, E_{cd} is 1.64 eV (Tauc gap 1.72 eV), which is significantly lower. The transmission spectra in Fig. A.1 show that the high dilution film has significantly smaller fringes than the low dilution film even that both films have the same thickness. Even through the extracted Cody and Tauc gaps are lower for the high dilution film, the optical absorption (α) in energy range 1.8 eV~2.2 eV is also lower, indicating distinctly different optical properties.

Photoconductivity and subgap absorption measurements were carried out on both samples. In this characterization, coplanar n⁺/Cr structures were used to ensure good ohmic contacts. First, the n⁺ layer is deposited on the film, then Cr pads are evaporated on the n⁺ layer using a shadow mask and then reactive ion etching was used to etch off the bare n⁺ layer to delineate the coplanar structure.

Fig. A.2 shows the electron mobility-lifetime products as a function of generation rate G for the two films in the annealed state along with those of a PSU diluted R=10 sample. Compared to the PSU sample, much lower $\mu\tau$ products are present in the low dilution film, while much higher $\mu\tau$ products are present in the high dilution film. Dual Beam Photoconductivity (DBP) subgap absorption measurements were also carried out for the annealed state at two generation rates, and results for low generation rates, corresponding to CPM, are shown in Fig. A.3 together with results on the PSU R=10 film. Lower subgap absorption is presented in the low dilution USSC film compared to the PSU film, with both of them showing subgap absorption spectra normally found in a-Si:H materials. However quite different subgap absorption is present in the high dilution film; one which is more like that for μ c-Si:H materials. It is important to note here that the USSC low dilution film has a lower mobility-lifetime product (photoconductivity) even though it also has a lower subgap absorption. The subgap absorption of

the high dilution film indicates the presence of the microcrystalline phase, which also explains the differences in the T&R characteristics discussed earlier.

Light soaking studies were carried out on the low dilution film with AM1.5 illumination up to 300 hr at room temperature with a calibrated ELH light source and an IR reflector. The IR reflector passed wavelengths between 0.4 and 0.7 μm and a cooling fan was used to keep sample at 27 °C. The surface temperature of the sample was measured with a thermocouple under illumination, measuring the temperature to within 1~2 °C. The uniformity variation of the illumination was within 5% across the 1/2x1/2 inch area. Both subgap absorption and photoconductivity were measured to monitor the light induced changes. The $\mu\tau$ products results indicated that the film reaches a steady state in about 120~150 hours. The results for two generation rates for this film as well as a PSU R=10 one are shown in Fig. A.4. The USSC film shows a little slower degradation compared to the PSU film. Subgap absorption spectra were also measured at 40, 150 and 300 hours to monitor the soaking process and are shown in Fig. A.5. The subgap absorption measured after 150hrs and 300hrs show no difference. Both subgap absorption and the $\mu\tau$ product results indicate that film reaches a degraded steady state after about 150 hours of AM1.5 light soaking. Even though the USSC and the PSU films have quite different characteristics in the annealed state, both films reach virtually identical degraded steady state as indicated by results in Fig. A.6 for $\mu\tau$ products and Fig. A.7 for subgap absorption.

As mentioned earlier, the presence of microcrystalline phase in the USSC high dilution film is indicated by both the T&R and subgap absorption results. To investigate if a phase transition occurred during the deposition of this high dilution sample, reactive ion etching (RIE) was used to etch the film to see if any change in the dark conductivity and $\mu\tau$ products could be observed in the remaining bulk. Only slightly drops in conductivity and $\mu\tau$ were found after etching off 2000Å. Removing up to 6000Å showed no further change in dark conductivity, suggesting that no dramatic phase transition occurred after 0.4 μm thickness. AFM studies on the surface topology for both low and high dilution samples were also carried out. The surface of the high dilution sample with an rms of 86Å is much rougher than the surface of the low dilution sample with a rms of 25Å, (similar to the PSU diluted film). The surfaces of $\mu\text{-Si:H}$ film are generally much rougher than those of a-Si:H films, so the AFM results support the presence of $\mu\text{c-Si:H}$ in the high dilution sample.

These two USSC films exhibit dramatically different properties from results of T&R, $\mu\tau$ products, subgap absorption, and AFM. No clear transition in conductivity after removing more than half of the high diluted film, indicating no large changes apparent during the growth of the film.

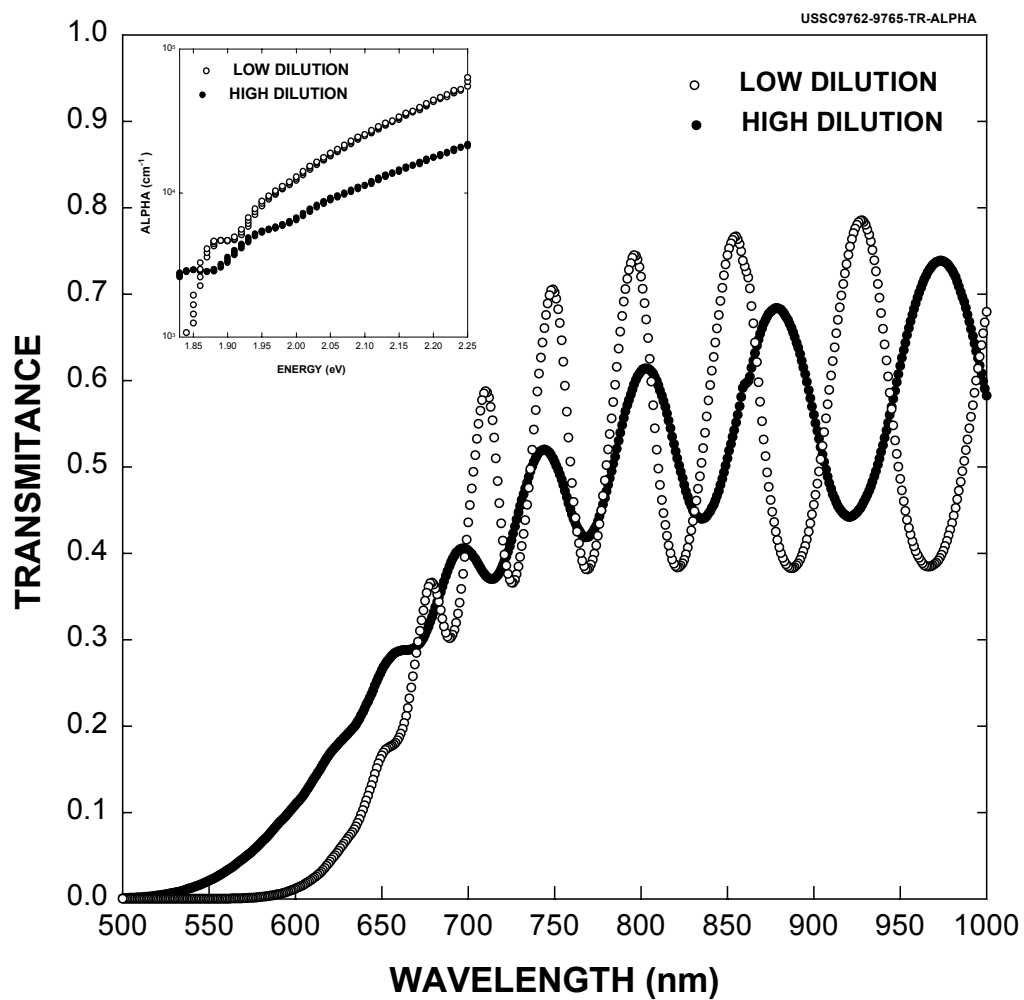


Figure A.1 Transmission spectra of USSC high and low dilution materials; the inset shows the absorption spectra (α).

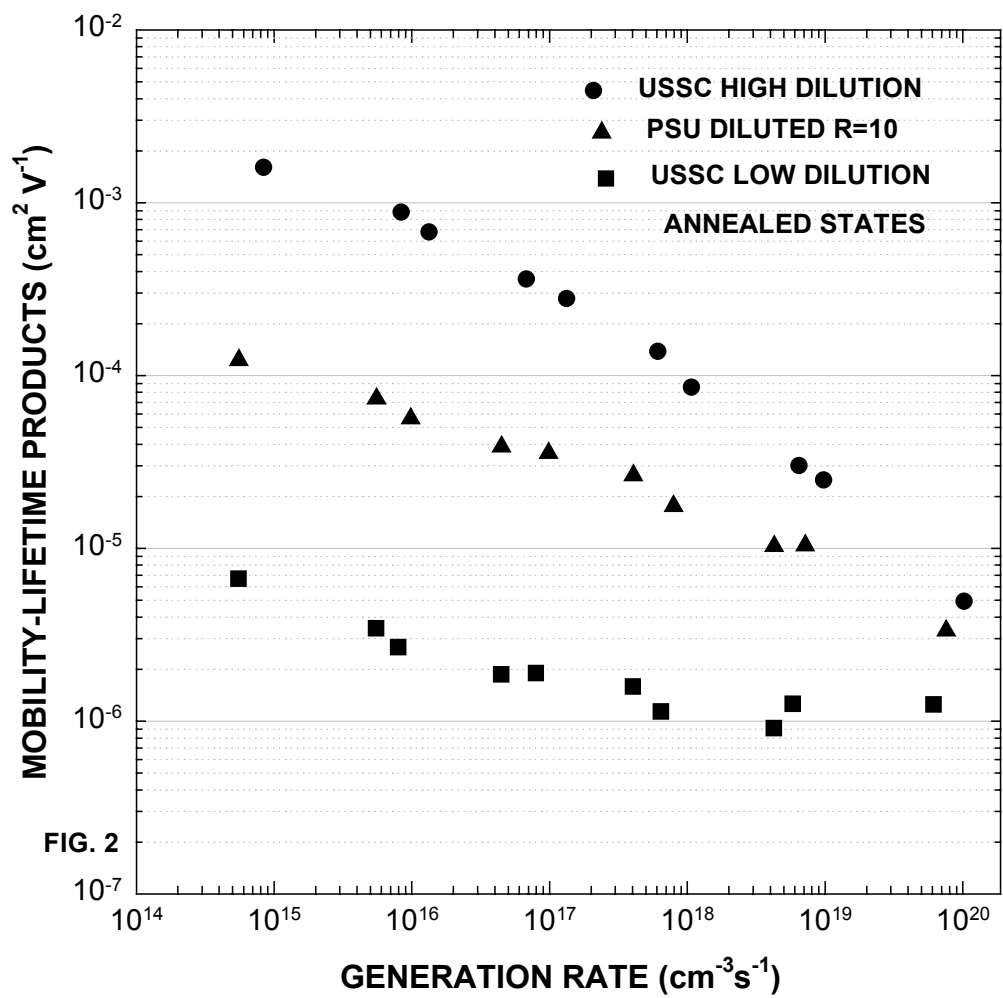


Figure A.2 Mobility-lifetime products of USSC low dilution, high dilution and PSU R=10 diluted materials in the annealed states.

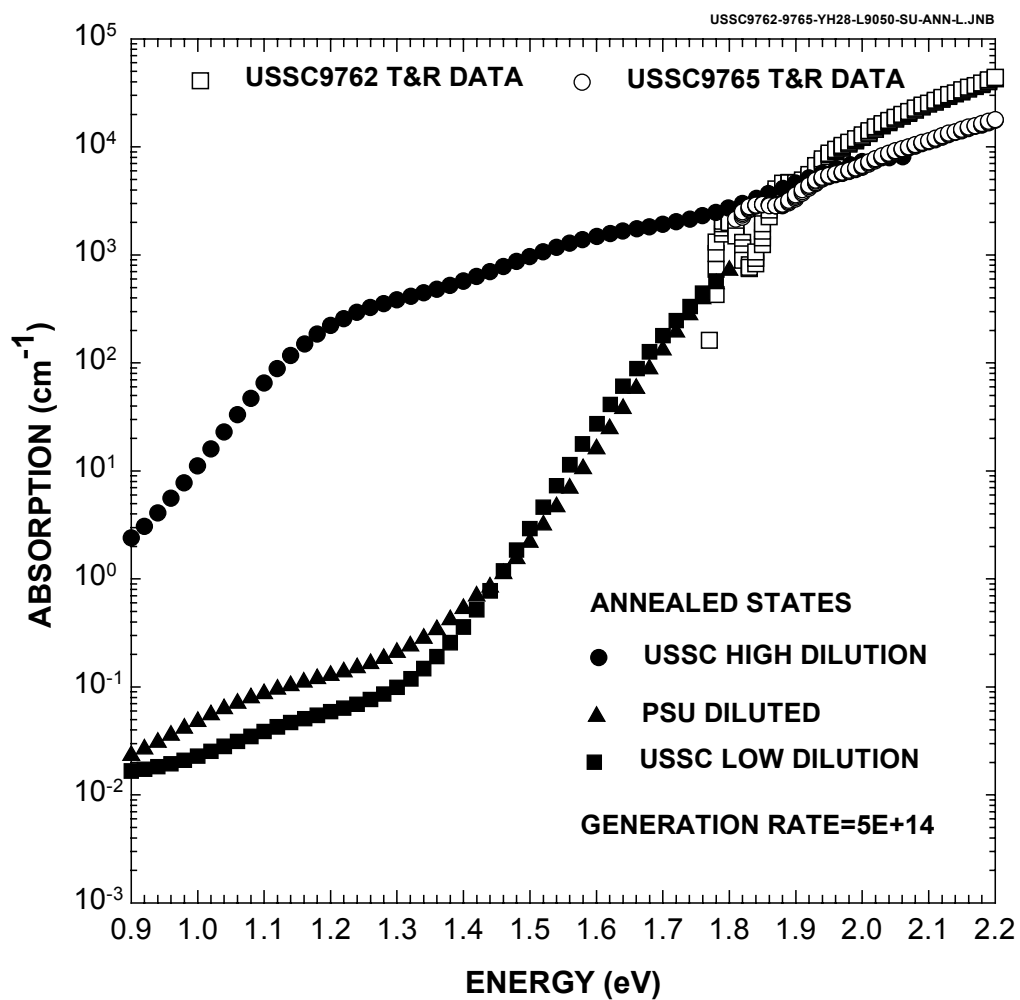


Figure A.3 Subgap absorption spectra of USSC low and high dilution materials and PSU R=10 diluted material in annealed states measured at low generation rate.

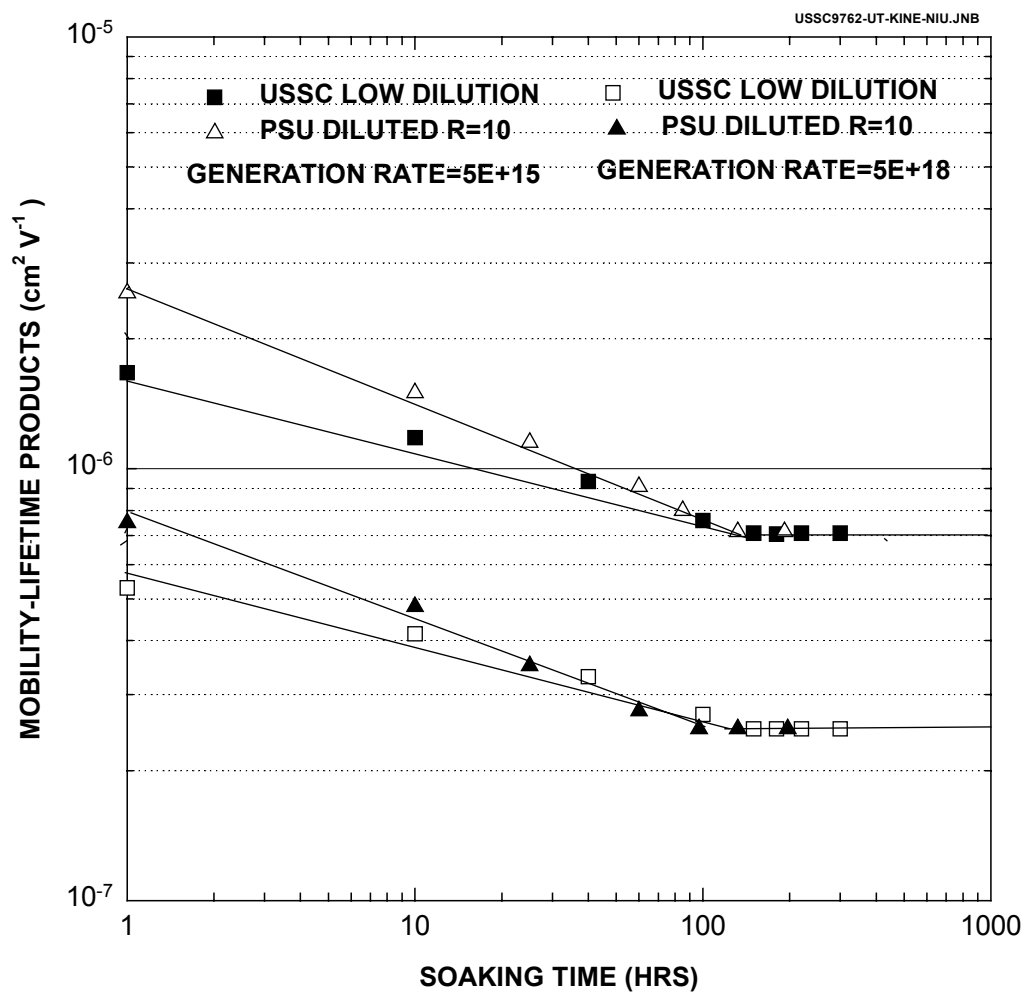


Figure A.4 Light soaking kinetics of USSC low dilution and PSU R=10 materials under 1 sun at room temperature measured using two generation rates.

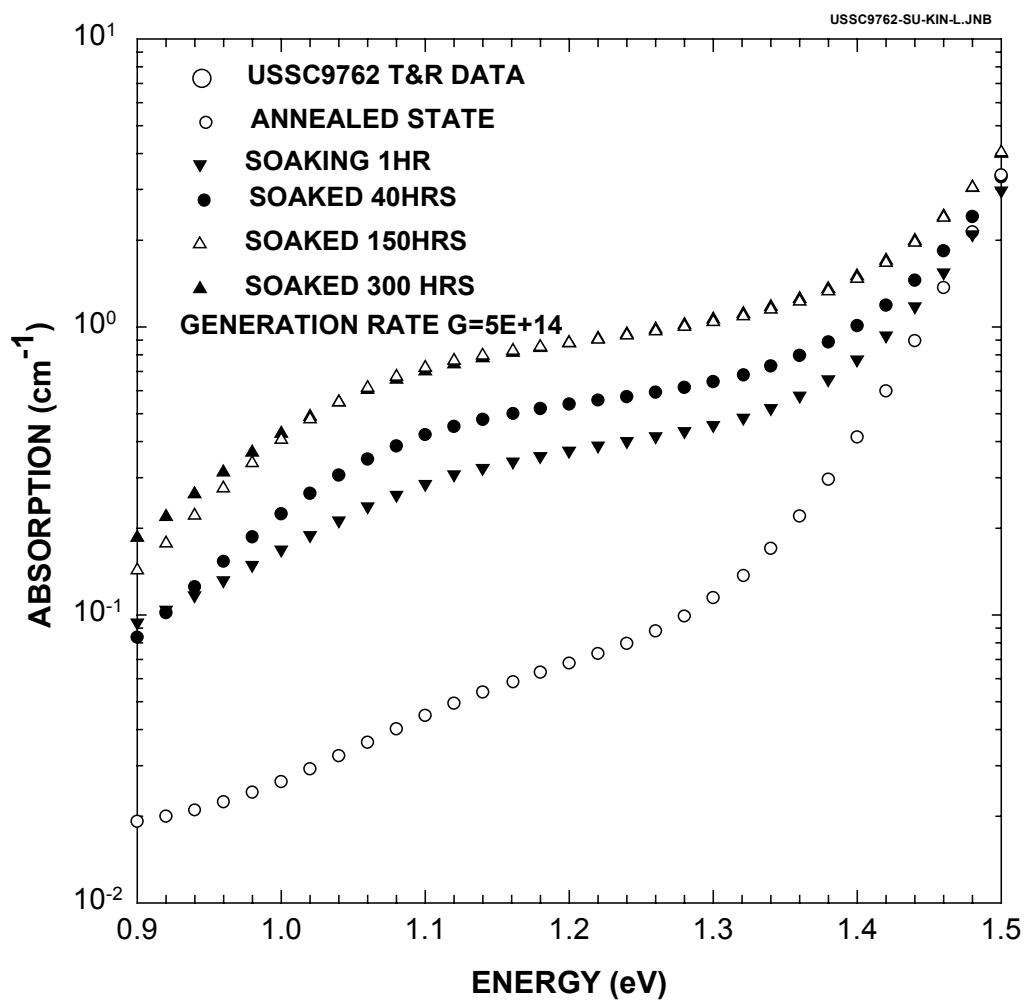


Figure A.5 Subgap absorption of USSC low dilution materials in annealed and different degraded states (1 sun at room temperature) measured using a low generation rate.

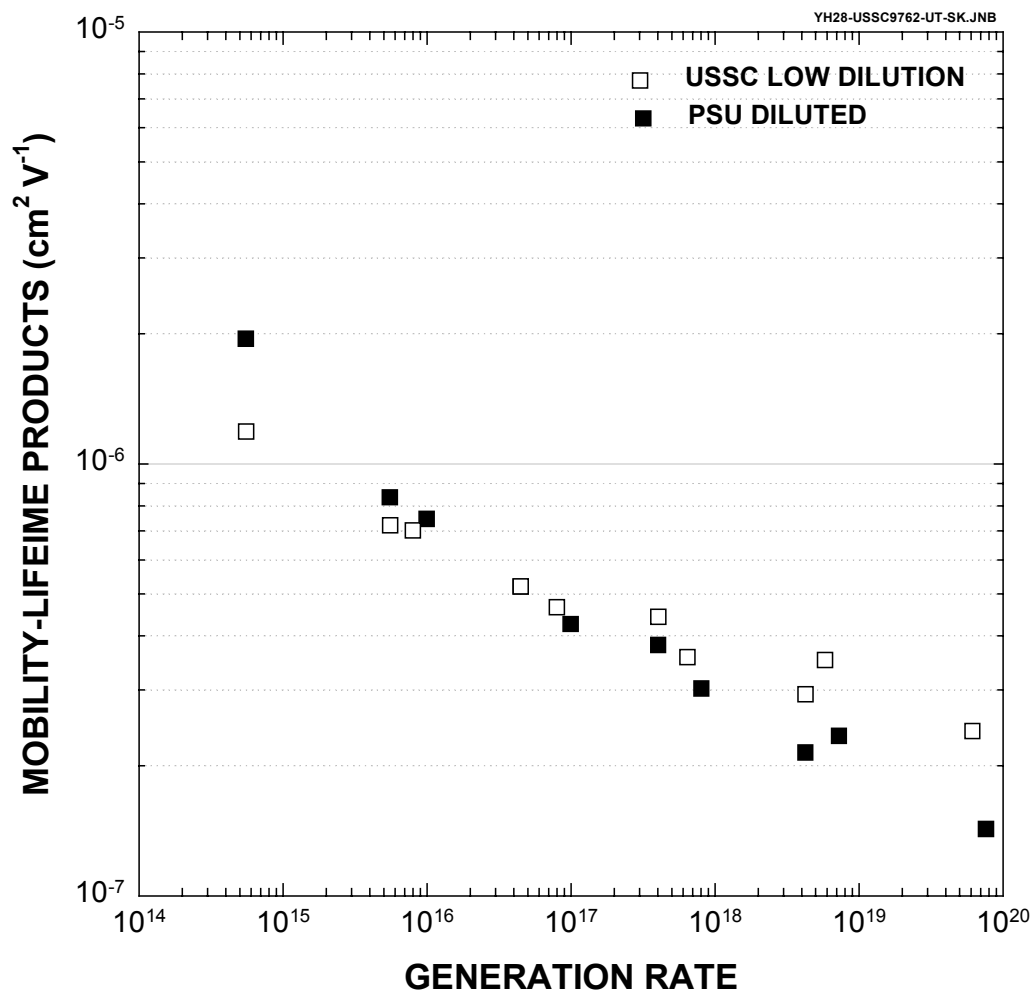


Figure A.6 Mobility-lifetime products of USSC low dilution and PSU R=10 diluted materials in the degraded steady state.

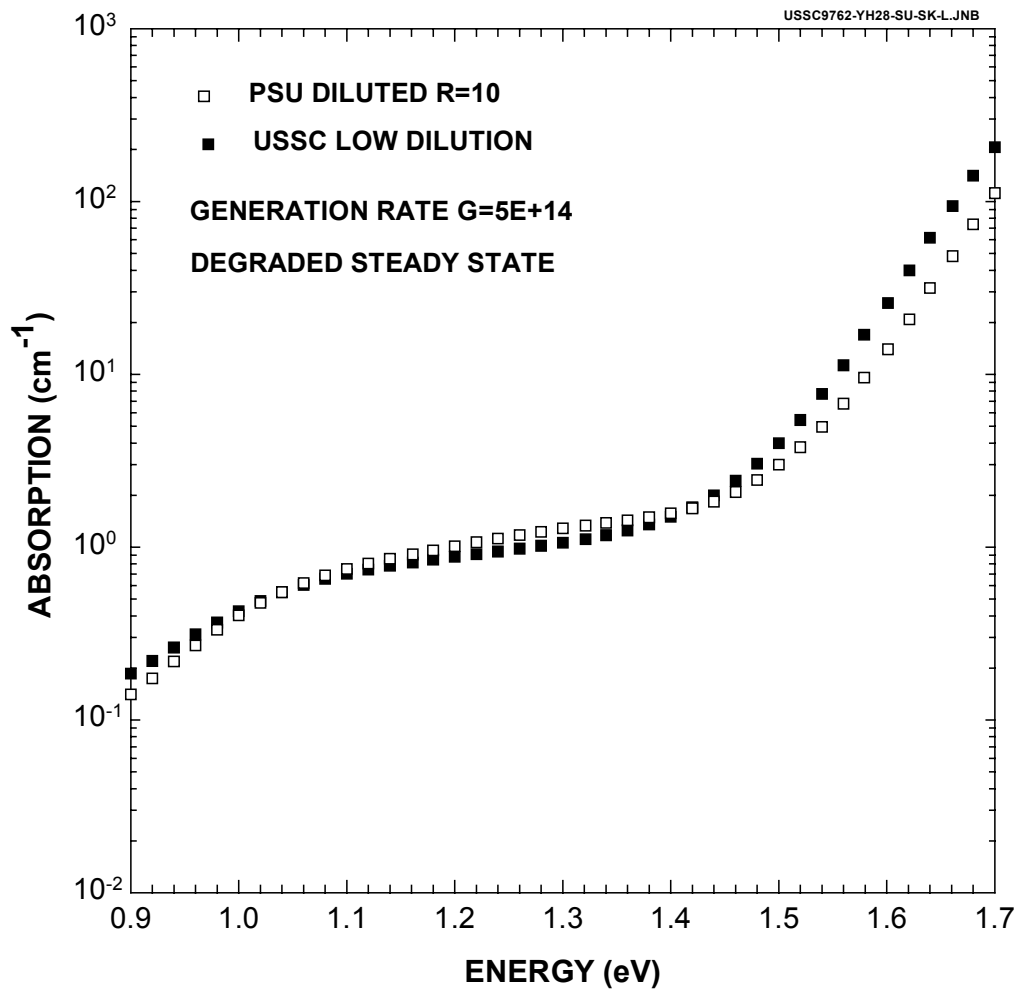


Figure A.7 Subgap absorption of USSC low dilution and R=10 PSU diluted materials in the degraded steady state.

Bibliography (1998-1999)

- (1) "Advances in Multichannel Spectroscopic Ellipsometry", R.W. Collins, I. An, H. Fujiwara, Joungchel Lee, Yiwei Lu, Joohyun Koh, and P.I. Rovira, Thin Solid Films 313-314, 18-32 (1998).
- (2) "Real Time Spectroscopic Ellipsometry for Characterization of the Crystallization of Amorphous Silicon by Thermal Annealing", M. Wakagi, Byungyou Hong, Joungchel Lee, H. Fujiwara, and R.W. Collins, Thin Solid Films 313-314, 464-468 (1998).
- (3) "Real Time Spectroscopic Ellipsometry for Characterization and Optimization of Amorphous Silicon-Based Solar Cell Structures", Joohyun Koh, H. Fujiwara, Yiwei Lu, C.R. Wronski, and R.W. Collins, Thin Solid Films 313-314, 469-473 (1998).
- (4) "Depth-Profiles in Compositionally-Graded Amorphous Silicon Alloy Thin Films Analyzed by Real Time Spectroscopic Ellipsometry", H. Fujiwara, Joohyun Koh, and R.W. Collins, Thin Solid Films 313-314, 474-478 (1998).
- (5) "Microstructural Evolution of a-Si:H Prepared using Hydrogen Dilution of Silane Studied by Real Time Spectroellipsometry", H. Fujiwara, J. Koh, and R.W. Collins, Journal of Non-Crystalline Solids 227-230, 73-77 (1998).
- (6) "Parameterization of the Optical Functions of a-Si:H and a-Si_{1-x}C_x:H: Applications to Carbon Depth Profiling and Surface Temperature Monitoring in Solar Cell Preparation", H. Fujiwara, Joohyun Koh, C.R. Wronski, and R.W. Collins, Journal of Non-Crystalline Solids 227-230, 460-464 (1998).
- (7) "Optical Depth Profiling of Band Gap Engineered Interfaces in Amorphous Silicon Solar Cells at Monolayer Resolution", H. Fujiwara, Joohyun Koh, C.R. Wronski, R.W. Collins, and J.S. Burnham, Applied Physics Letters 72, 2993-2995 (1998).
- (8) "Real Time Spectroscopic Ellipsometry Characterization of Structural and Thermal Equilibration of Amorphous Silicon-Carbon Alloy p-Layers in p-i-n Solar Cell Fabrication", H. Fujiwara, Joohyun Koh, Yeeheng Lee, C.R. Wronski, and R.W. Collins, Journal of Applied Physics 84, 2278-2286 (1998).
- (9) "Optimization of Hydrogenated Amorphous Silicon p-i-n Solar Cells with Two-Step i Layers Guided by Real Time Spectroscopic Ellipsometry", Joohyun Koh, Yeeheng Lee, H. Fujiwara, C.R. Wronski, and R.W. Collins, Applied Physics Letters 73, 1526-1528 (1998).
- (10) "Real-Time Characterization of Film Growth on Transparent Substrates by Rotating Compensator Multichannel Ellipsometry", Joungchel Lee and R.W. Collins, Applied Optics 37 4230-4238 (1998).

- (11) "Rotating Compensator Multichannel Ellipsometry: Applications for Real Time Stokes Vector Spectroscopy of Thin Film Growth", Joungehel Lee, P.I. Rovira, Ilsin An, and R.W. Collins, *Review of Scientific Instruments* 69, 1800-1810 (1998).
- (12) "An Improved Analysis for Band Edge Optical Absorption Spectra in Hydrogenated Amorphous Silicon from Optical and Photoconductivity Measurements", Lihong Jiao, Ingshin Chen, R.W. Collins, and C.R. Wronski, *Applied Physics Letters* 72, 1057-1058 (1998).
- (13) "Nucleation of p-Type Microcrystalline Silicon on Amorphous Silicon for n-i-p Solar Cells Using B(CH₃)₃ and BF₃ Dopant Source Gases", Joohyun Koh, H. Fujiwara, R.J. Koval, C.R. Wronski, and R.W. Collins, *Materials Research Society Symposium Proceedings, Proceedings of the Spring 1998 Meeting of the Materials Research Society, Symposium A*, (MRS, Pittsburgh, 1998).
- (14) "Real Time Spectroscopic Ellipsometry Studies of the Solid Phase Crystallization of Amorphous Silicon", H. Fujiwara, Joohyun Koh, Yeeheng Lee, C.R. Wronski, and R.W. Collins, *Materials Research Society Symposium Proceedings, Proceedings of the Spring 1998 Meeting of the Materials Research Society, Symposium A*, (MRS, Pittsburgh, 1998).
- (15) "Application of Real Time Optics for the Design of Optimized Solar Cells", R.W. Collins, H. Fujiwara, Joohyun Koh, Yeeheng Lee, and C.R. Wronski, Technical Digest of the 11th "Sunshine" Workshop on Thin Film Solar Cells, 26 January 1998, Shinjuku, Tokyo, Japan, (MITI-NEDO, Tokyo, 1998), pp. 19-26.
- (16) "Effects of Charged Defects on Stability of a-Si:H Materials and Solar Cells", C.R. Wronski, L. Jiao, and R.W. Collins, Technical Digest of the 11th "Sunshine" Workshop on Thin Film Solar Cells, 26 January 1998, Shinjuku, Tokyo, Japan, (MITI-NEDO, Tokyo, 1998), pp. 67-74.
- (17) "In Situ Characterization of Structural Relaxation in p-Type Amorphous Silicon Carbon Alloys", H. Fujiwara, J. Joh, Y. Lee, C.R. Wronski, and R.W. Collins, Proceedings of the 45th Japan Society of Applied Physics, (Tokyo, Japan, 1998), p. 930.
- (18) "Application of Real Time Spectroscopic Ellipsometry for Depth Profiling of Compositionally Graded Amorphous Silicon Alloy Thin Films", H. Fujiwara, J. Koh, J.S. Burnham, C.R. Wronski, and R.W. Collins, Proceedings of the 45th Japan Society of Applied Physics, (Tokyo, Japan, 1998), p. 902.
- (19) "Spectroscopic Ellipsometry", edited by R.W. Collins, D.E. Aspnes, and E.A. Irene (Elsevier, Amsterdam, 1998), pp. 1-850.
- (20) "Real Time Spectroscopic Ellipsometry Studies of the Nucleation and Growth of p-Type Microcrystalline Silicon Films on Amorphous Silicon Using B₂H₆, B(CH₃)₃, and BF₃

- Dopant Source Gases", Joohyun Koh, H. Fujiwara, R.J. Koval, C.R. Wronski, and R.W. Collins, *Journal of Applied Physics* 85, 4141-4153 (1999).
- (21) "Analysis of Contamination, Hydrogen Emission, and Surface Temperature Variations Using Real Time Spectroscopic Ellipsometry during p/i Interface Formation in Amorphous Silicon p-i-n Solar Cells", H. Fujiwara, Joohyun Koh, C. R. Wronski, and R. W. Collins, *Applied Physics Letters* 74, 3687-3689 (1999).
 - (22) "Analysis of Specular and Textured SnO₂:F Films by High Speed Four-Parameter Stokes Vector Spectroscopy", P.I. Rovira and R.W. Collins, *Journal of Applied Physics* 85, 2015-2024 (1999).
 - (23) "Dual Rotating-Compensator Multichannel Ellipsometer: An Instrument Design for Real Time Mueller Matrix Spectroscopy of Surfaces and Films", R.W. Collins and Joohyun Koh, *Journal of the Optical Society of America A* 16, 1997-2006 (1999).
 - (24) "Real Time Characterization of Non-Ideal Surfaces and Thin Film Growth by Advanced Ellipsometric Spectroscopies", R.W. Collins, P.I. Rovira, A.S. Ferlauto, J.A. Zapien, R. Messier, and C.R. Wronski, *Mater. Res. Soc. Symp. Proc.* 59, 43-58 (1999).
 - (25) "Extension of Multichannel Spectroscopic Ellipsometry into the Ultraviolet for Real Time Characterization of the Growth of Wide Bandgap Materials from 1.5 to 6.5 eV", J.A. Zapien, R.W. Collins, and R. Messier, *Mater. Res. Soc. Symp. Proc.* 59, 71-76 (1999).
 - (26) "Characteristics of Solar Cells and Materials Fabricated from both Deuterated and Hydrogenated Silane", L. Jiao, R. Koval, X. Niu, J. Koh, R.W. Collins, and C.R. Wronski, *Proceedings of the Second World Conference and Exhibition on Photovoltaics Solar Energy*, Vienna, Austria (July 1998).
 - (27) "Enhancement of Stable Open Circuit Voltages in a-Si:H p-i-n Solar Cells by High Hydrogen Dilution of the p/i Interface Regions", Y. Lee, A.S. Ferlauto, Z. Lu, J. Koh, H. Fujiwara, R.W. Collins and C.R. Wronski, *Proceedings of the Second World Conference on Photovoltaics*, Vienna, Austria, p. 940 (July 1998).
 - (28) "Characterization of Light Induced Gap States in a-Si Materials", C.R. Wronski, L. Jiao, Z. Lu, X. Niu, R.W. Collins, and A. Matsuda, *Review Meeting for Research with Overseas Country Research Institutes, Technical Digest*, (1998), p. 17.
 - (29) "Recent Progress in Real Time Optics for a-Si:H Solar Cell Optimization", R.W. Collins, J. Koh, H. Fujiwara, R. I. Rovira, A. Ferlauto, and C.R. Wronski, *Review Meeting for Research with Overseas Country Research Institutes, Technical Digest*, (1998), p. 1.
 - (30) "Characteristics of Different Thickness a-Si:H/Metal Schottky Barrier Cell Structures-Results and Analysis", Z. Lu, L. Jiao, R. Koval, R.W. Collins and C.R. Wronski (1999), *Mat. Res. Soc. Symp. Proc.* (in press).

- (31) “Kinetics of Light-Induced Changes in P-I-N Cells with Protocrystalline Si:H”, R.J. Koval, J. Koh, Z. Lu, Y. Lee, L. Jiao, R.W. Collins and C.R. Wronski (1999), Mat. Res. Soc. Symp. Proc. (in press).
- (32) “Performance and Stability of Si:H p-i-n Solar Cells with i Layers Prepared at the Thickness-Dependent Amorphous-to-Microcrystalline Phase Boundary”, Randy J. Koval, Joohyun Koh, Z. Lu, L. Jiao, R.W. Collins, and C.R. Wronski(1999), Appl. Phys. Lett. (in press).

REPORT DOCUMENTATION PAGE			Form Approved OMB NO. 0704-0188	
Public reporting burden for this collection of information is estimated to average 1 hour per response, including the time for reviewing instructions, searching existing data sources, gathering and maintaining the data needed, and completing and reviewing the collection of information. Send comments regarding this burden estimate or any other aspect of this collection of information, including suggestions for reducing this burden, to Washington Headquarters Services, Directorate for Information Operations and Reports, 1215 Jefferson Davis Highway, Suite 1204, Arlington, VA 22202-4302, and to the Office of Management and Budget, Paperwork Reduction Project (0704-0188), Washington, DC 20503.				
1. AGENCY USE ONLY (Leave blank)		2. REPORT DATE August 2000		3. REPORT TYPE AND DATES COVERED Annual Report-Phase I, 17 July 1998-16 October 1999
4. TITLE AND SUBTITLE Stable a-Si:H Based Multijunction Solar Cells with Guidance from Real Time Optics; Annual Report-Phase I, 17 July 1998-16 October 1999			5. FUNDING NUMBERS C: XAF-8-17619-22 TA: PV005001	
6. AUTHOR(S) C.R. Wronski, R.W. Collins, L. Jiao, A. Ferlauto, P.I. Rovira, R.J. Koval, Z. Lu, and X. Niu				
7. PERFORMING ORGANIZATION NAME(S) AND ADDRESS(ES) Center for Thin Film Devices The Pennsylvania State University University Park, PA 16802			8. PERFORMING ORGANIZATION REPORT NUMBER	
9. SPONSORING/MONITORING AGENCY NAME(S) AND ADDRESS(ES) National Renewable Energy Laboratory 1617 Cole Blvd. Golden, CO 80401-3393			10. SPONSORING/MONITORING AGENCY REPORT NUMBER NREL/SR-520-28809	
11. SUPPLEMENTARY NOTES NREL Technical Monitor: B. von Roedern				
12a. DISTRIBUTION/AVAILABILITY STATEMENT National Technical Information Service U.S. Department of Commerce 5285 Port Royal Road Springfield, VA 22161			12b. DISTRIBUTION CODE	
13. ABSTRACT (Maximum 200 words). This summary describes tasks of novel improved intrinsic materials for multijunction solar cells, insights into improved stability in materials and solar cells, optimization of solar cell performance with improved intrinsic layers, and optimization of multijunction solar cells. The report characterizes a "protocrystalline" a-Si:H film growth regime where thin samples retain their amorphous state when their growth time or thickness is limited to small values, even when films are deposited with high hydrogen dilution that results in microcrystalline thick films. The Staebler-Wronski degradation kinetics of films and devices are systematically studied as a function of hydrogen dilution.				
14. SUBJECT TERMS photovoltaics ; multijunction solar cells ; novel i-layer materials ; optimization of p/i interfaces ; amorphous silicon ; p-i-n solar cells ; n-i-p solar cells ; Staebler-Wronski degradation ; Schottky barrier cell ; TCO studies; optical modeling ; tunnel junction formation			15. NUMBER OF PAGES	
			16. PRICE CODE	
17. SECURITY CLASSIFICATION OF REPORT Unclassified		18. SECURITY CLASSIFICATION OF THIS PAGE Unclassified	19. SECURITY CLASSIFICATION OF ABSTRACT Unclassified	20. LIMITATION OF ABSTRACT UL